Preparation and characterization of magnetic EuO and related compounds: EuS and Eu_2O_3

Thesis Submitted by
Iris Moder
to apply for the degree of Doctor in Physics

Thesis Supervisor: Prof. Javier Rodríguez-Viejo

Universitat Autònoma de Barcelona

Grup de Nanomaterials i Microsistemes
Departament de Física
Universitat Autònoma de Barcelona

Bellaterra, September 2012

Contents

Chapter 1

Introduction

Since the discovery of the giant magnetoresistance (GMR) in 1988 by Albert Fert and Peter Grünberg in multilayers alternating a ferromagnetic metal with a nonmagnetic metal (e.g. Fe/Cr or Co/Cu) spintronic technology began to develop. The present challenge is to find systems with a stronger spin polarisation than that of common ferromagnetic metals (iron, cobalt, nickel, etc.). Here, magnetic oxides form an interesting class of candidate materials.
The ferromagnetic insulator europium monoxide (EuO) is the only known binary oxide that can be grown in a thermodynamically stable form in contact with silicon [1] and it can be epitaxially integrated with mainstream semiconductors such as silicon and GaN [2, 3]. Its conductivity can be matched to the conductivity of silicon by introducing oxygen vacancies [4], which is a key necessity for coherent spin injection in spintronic devices [5]: In such devices the polarization of the spin current in direct electrical spin injection from a metallic ferromagnet into a semiconductor depends directly on the ratio of their resistances (R_F/R_S). This is often referred to as *conductivity mismatch problem.*
Therefore, heterostructures composed of Si and EuO may be used as model systems for studying applications of devices in the field of spintronics, where besides the charge, the spin degree of freedom is also used to control the flow of conduction electrons. Another approach for avoiding the *conductivity mismatch problem* is using EuO as a ferromagnetic tunnel barrier [6]. Where electrons tunnel through insulating EuO, which acts as a spin filtering tunnel barrier, into a semiconductor. Spin injection via tunneling seems also a promising mechanism since the tunneling process is not affected by the conductivity mismatch between stoichiometric EuO and the semiconductor. The high exchange splitting of the conduction band and the resulting high spin polarization makes EuO a specially attractive material for semiconductor-based spintronic devices. A spin polarization at the contact between EuO and the transport medium (Si) of 100% is expected [6]. Thermally evap-

orated polycrystalline EuO thin films have been studied but only a polarization of 29% can be reached [7], using EuO as a tunnel barrier. In case of using EuS, a material similar to EuO, spin polarizations up to 85% [8,9] were reached in tunnel measurements. In comparison, polarization in epitaxial La-doped EuO films exceeds 90% [2] measured by means of Andreev reflection.
This thesis mainly focuses on EuO, nevertheless also EuS tunnel measurements were performed, as its magnetic properties are similar to EuO, and has advantages when it comes to deposition.

Material	Curie Temperature (K)	magn. Moment (μ_B)	$2\Delta E_{ex}$ (eV)	lattice a (nm)
EuS	69	7.0	0.36	FCC, 0.596
EuO	16	7.0	0.54	FCC, 0.514

Also high epitaxial Eu_2O_3 was deposited as a by-product.

1.1 Physical Properties of EuO

1.1.1 Structure and growth

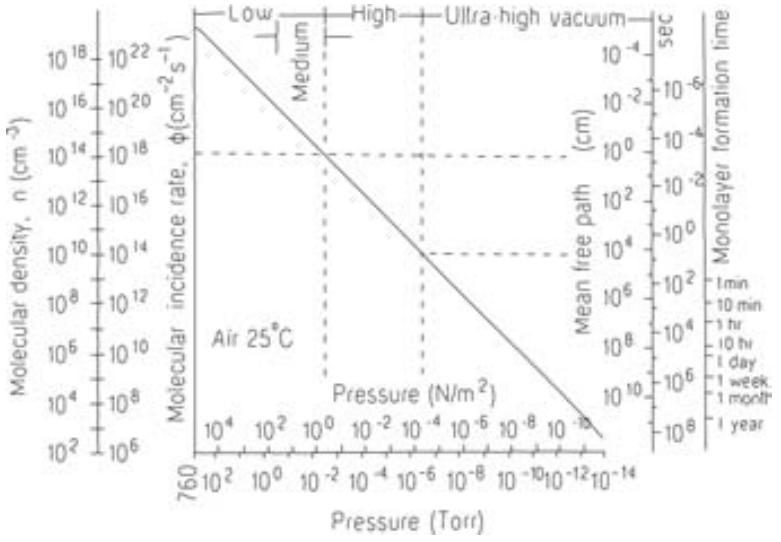

Figure 1.1: Molecular density, incidence rate, mean free path and monolayer formation time as a function of pressure for unhindered oxidation taken from [10].

EuO crystalizes in a NaCl structure with a lattice constant of 5.14Å [11] at room temperature, which reduces to 5.127Å below 10 K. Although it

is unstable in air, the reaction kinetics are low enough that single crystal EuO has been made in the 1960s [12]. Either by melting together Eu and Eu_2O_3 [13, 14], or by reducing Eu_2O_3 at a temperature of 1500°C in an hydrogen environment, bulk EuO is formed. With a heat of formation, $\Delta H_f = 1730$kJ/mol, for Eu_2O_3 compared to $\Delta H_f = 608$kJ/mol for EuO, Eu readily oxidizes to form the more stable compound Eu_2O_3. Hence, a high control of the oxygen flow and the deposition rate are essential for EuO deposition. Furthermore the formation of higher oxides is not a self-limited process, various 100nm can be oxidized before further oxygen diffusion is stopped. As shown in figure 1.1 and also observed in our experiments the oxidation of a EuO surface monolayer, even in high vacuum of 10^{-8} Torr, is a matter of minutes! Because of this a fast, *in-situ* capping of the deposited film is essential to preserve stoichiometry. Because of this the growth of high quality thin EuO films was hindered during decades. The first published deposition conditions of EuO film growth are shown in table 1.1. All films are polycrystalline as typical growth rates are $2 - 7$Å/s and generally glass and fused quartz substrates were used. Co-evaporation of Eu and Eu_2O_3 was mostly used, but also reactive evaporation of Eu metal in oxygen atmosphere was a common method for the film deposition. The substrate was generally heated to temperatures up to 500°C. The pressure during the deposition was mostly in the range of $10^{-6} - 10^{-5}$ Torr, with the exception of references [15, 16], who were the first to use an ultra high vacuum system for growth of Eu-rich films. The rather high pressures used in other depositions may not be sufficient to avoid the presence of water or hydrocarbons in the films. One can note, that all the films shown in the table, except the last two, were deposited at the *IBM Watson Research Center*.

Table 1.1: Range of conditions used for the first EuO films.

year	ref.	deposition technique	P during growth (Torr)	T_S (°C)
1967	Suits [17]	- heating bulk EuO using an electron beam - co-evaporation of Eu and Eu_2O_3 - evaporation of Eu in oxygen atmosphere	$10^{-6} - 10^{-5}$	250
1968	McGuire [18]	co-evaporation of Eu, Eu_2O_3, and rare earth oxides of either Gd, La, Nd, Ho, or Y	10^{-5}	250
1970	Suits [15]	rf sputtering of EuO in argon atmosphere	$10^{-9} + P_{\text{Argon}}$	-150 - 500
1970	Shafer [19]	co-evaporation of Eu_2O_3 and Eu - Fe doped	6×10^{-6}	200
1971	Suits [20]	co-evaporation of Eu, Eu_2O_3 - Fe, Eu doped	$0.5 - 8 \times 10^{-6}$	140, 250
1971	Lee [16]	- rf sputtering of EuO - co-evaporation of Eu and Eu_2O_3 - Eu, Fe, La doped	$10^{-10} - 10^{-9}$+P_{Argon}	not indicated
1971	Suits [21]	co-evaporation of Eu, Eu_2O_3 - Ag, Cu and Eu doped	$\leq 8 \times 10^{-6}$	not indicated
1971	Bordure [22]	Reactive evaporation of Eu metal in oxygen atmosphere	10^{-5}	not indicated
1974	Van Dang [23]	- Oxidation of evaporated Eu metal on substrate	3×10^{-7}	200 - 250
		- Reactive evaporation of Eu metal in oxygen atmosphere	10^{-5}	400

After almost 2 decades growing interest is found in EuO again, due to advances in deposition and characterization methods. More recently several groups managed to grow stoichiometric epitaxial thin EuO films mainly by MBE deposition [2, 24–29], similar to the reactive evaporation of Eu metal in oxygen atmosphere described before. More recently, also other vapor phase techniques, such as Pulsed Laser Deposition [28, 30] and magnetron sputtering [31], have also been successfully used to prepare EuO thin films thanks to the achievement of base pressures as low as 10^{-9} Torr, which allows working with oxygen partial pressures and europium fluxes comparable to those of MBE systems. Polycrystalline EuO films have been grown directly on silicon using bare surfaces [32–34] or onto metal-coated surfaces used as bottom electrode to perform electrical and magnetic characterizations [7,31, 35–37]. In recent studies epitaxial and single crystalline EuO films can be achieved using yttria-stabilized cubic zirconia (YSZ) [24, 24, 25], cubic-ZrO_2 [26], MgO [27], $SrTiO_3$ [27], $YAlO_3$ [2, 28, 29], SrO-buffered and unbuffered Si [2], and SrO-buffered GaN [2] substrates and Ni [38]. Typical growth temperatures range from room temperature to 590°C with deposition rates of 0.05-0.2Å/s using a partial oxygen pressure of $2 \times 10^{-7} - 2 \times 10^{-9}$ Torr. Generally EuO is grown by carefully adjusting the Eu flux to the partial oxygen pressure in a 1:1 ratio. Anyhow, stoichiometry is still a serious problem as several studies reported that Eu^{3+} contaminants are partially present in the films.

1.1.2 Electronic structure of EuO

Metal Europium has 63 electrons which are in the [Xe]$4f^7 5d^0 6s^2$ ground state configuration. It appears in two valence states, either 3+ or 2+, where 3+ is the more stable form. The electronic ground state of EuO is Eu:[Xe]$4f^7 5d^0 6s^0$ O: $1s^2 2s^2 2p^6$, where the conduction band consisting of the 6s and the 5d orbitals of Eu^{2+} is empty. The full valence band is formed by the p orbitals of O^{2-}. The energy gap between the conduction and valence band is 4.3 eV. In between these two bands lies a narrow half-filled strongly localized 4f-band containing 7 electrons. Following Hund's rules in the ground state configuration the 4f electrons align parallel leading to a magnetic moment with a magnitude of $\mu_B gJ = 7.0\mu_B$ [1]. This is matched by band structure calculations [40, 41] predicting a magnetic moment of 6.8 and $7.0\mu_B$ and SQUID measurements of bulk crystals and thin films (also in this thesis). Below the Curie temperature the $5d$ density of states of the conduction band splits into two levels, the lower spin-up energy $5dt_{2g}$ states and the higher spin-down energy $5de_g$ states. The exchange splitting of $2\Delta E_{ex} = 0.54$eV of the conduction band was first measured by the optical studies [42], being one of the highest.

1.1.3 Magnetism

EuO is often used as a model system as it is considered an ideal Heisenberg magnet. It has a Curie temperature od 69K and a magnetic moment of $7\mu_B$ when in the ferromagnetic state. The magnetism of EuO is determined by the magnetic moments in the half-filled Eu 4f shell which align parallel. As the exchange interaction via free electrons is very unlikely in a semiconductor, the existence of a ferromagnetic semiconductor or insulator like EuO has been doubted for a long time. Furthermore, there exist several other magnetic ordering Eu chalcenogides, such as EuS, EuSe and EuTe, which order antiferromagnetically. Neutron scattering experiments [14] have shown that specially the spin-wave spectrum of EuO can be described conveniently with the well known Heisenberg exchange model [43].

$$H = -\sum_{i \neq j} J_{ij} \mathbf{S_i} \cdot \mathbf{S_j} \tag{1.1.1}$$

The interaction between localized magnetic moments $\mathbf{S_i}$ and $\mathbf{S_j}$ is determined by the exchange integral J_{ij}. Usually one distinguishes between direct exchange processes between neighboring lattice sites i, j, indirect exchange

[1] EuO has an effective (paramagnetic) moment $\mu_B g\sqrt{J(J+1)} = 7.9\mu_B$, which is the magnitude of the moment. The saturation moment $\mu_B gJ$ reached by a ferromagnet is the maximum value of the projection of the moment on the applied field direction [39]. for each europium atom. For the Eu^{2+} ion with a Landau factor $g = 2$, orbital angular momentum quantum number $L = 0$ and spin angular momentum quantum number $S = 7/2$ from the half filled $4f^7$ states, the total angular momentum is $J = L + S = 7/2$.

processes and superexchange processes due to virtual excitations. From neutron scattering experiments the exchange parameters J_1 and J_2 can be calculated ($J_1/k_B = 0.606 \pm 0.008$ K and $J_2/k_B = 0.119 \pm 0.015$ K). It is generally accepted [44,45] that the nearest neighbor exchange J_1 is based on a 4f electron having a virtual excitation to the 5d band. There it undergoes a d-f exchange with the nearest neighbor Eu site that polarizes the electrons spin, which then returns to its initial 4f state. This leads to ferromagnetic coupling. The nature of the next-nearest neighbor exchange constant J_2 is thought to be more complex and involves various competing exchange paths between the O2p, Eu5d, and 4f orbitals:
1. The Kramers-Anderson superexchange, where an f electron is transferred via oxygen to an f orbital on a neighboring atom. This exchange is antiferromagnetic and very small.
2. The antiferromagnetic superexchange via the d-f interaction, where oxygen electrons are transferred to the d orbitals of neighboring Eu atoms, there they affect the 4f spins via the d-f exchange interaction.
3. The net J_2 exchange from contributions 1. and 2. is ferromagnetic and can be understood as the virtual excitation of an O 2p electron to the conduction band, where it contributes to the exchange.
Although J_2 is positive for EuO, its strength is much smaller as compared to J_1 and it becomes more negative across the chalcogenides, so that EuSe and EuTe are antiferromagnetic.

1.1.4 Manipulating the Curie Temperature T_C - Effect of doping, strain and film thickness

At the moment the low Curie temperature of EuO impedes the incorporation into devices. Doping with lanthanides or oxygen vacancies as well as introducing strain can raise it well above liquid nitrogen temperatures.
When doping with rare earth metals Gd, Tb, Dy, Lu, La, Ce, Ho and Y [2, 24, 46–50], the dopant atoms are substituting the Eu^{2+} ion with trivalent ions and thus introduce one extra electron per dopant atom. This will effectively enhance the magnetic coupling between Eu^{2+} 4f local moments via 5d conduction electrons due to the 4f - 5d exchange interaction, which is responsible for the enhancement of T_C beyond 70 K [49]. One can expect that the dopant atom, i.e. Gd, in the EuO matrix can be in two different states: either the extra electron is delocalized in the conduction band and the atom becomes a Gd^{3+} ion or the electron stays localized and the atom is a Gd^{2+} ion. Using high dopant concentrations results in a metallic phase with delocalized electrons. For low concentrations of dopants the excess electron is trapped at the Gd site and polarizes neighboring Eu^{2+} ions via the Gd 5dEu 4f exchange interaction, thus creating a giant spin molecule or bound magnetic polaron [45, 51]. It contributes to conduction via hopping or diffusion. The earlier probosed activation laws as described

by [44] are not valid, where a minimum dopant concentration of about $\sim 1\%$ is necessary before an enhancement of T_C is observed. Sutarto et al. observed enhancement of T_C with Gd concentrations as low as 0.2 % [24]. The highest T_C of $\sim$ 200K was found studying EuO thin films doped with 10% La [48]. However, because the exchange interaction of the dopant and Eu electrons decreases with higher doping (observed experimentally as a decrease in magnitude of the red shift ΔE_{ex} [13] with increasing number of dopants), the T_C reaches saturates at a certain dopant concentration and even decreases for higher concentrations. The same effect can be observed when doping with oxygen vacancies, where thin films of $EuO_{1-\delta}$ increase the T_C, which is attributed to the presence of Eu-metal which contributes conduction electrons to enhance the Eu^{2+}-Eu^{2+} interaction. On the other hand in oxygen-rich $EuO_{1+\delta}$ the Eu^{2+}-Eu^{2+} exchange interaction is weakened by the formation of a metastable solution with notable amounts of Eu^{3+} in the EuO lattice [19].
One of the most striking properties of EuO is the strong colossal magneto resistance (CMR) effect observed in EuO that is doped by oxygen vacancies [2, 52, 53] and Gd [4, 13] for having a metal-insulator transition. A resistivity drop of more than 8 orders of magnitude below T_C has been observed for Eu-rich EuO. The free charge carriers appear to be nearly 100% spin polarized in the metallic phase. Below T_C the magnetic part of the binding energy disappears more and more and the Coulomb energy of the weaker bound electron is not large enough to localize the electron, thus leading to a metal-like conductivity. Actually, the CMR in EuO is one of the strongest effects of that kind ever observed in nature. For higher doping concentrations the samples are metallic at all temperatures.

An enhancement of T_C up to 200K has also been achieved by applying a hydrostatic pressure of 100kbar [11, 54]. Although hydrostatic pressure is not an option for device applications, this gives rise to the possibility of adjusting the EuO Curie temperature by introducing strain in the sample. Simulations show that T_C can be raised to almost 250 - 300K when a the EuO lattice is isotropically compressed by a factor of 0.92 [55, 56]. In the case of biaxial stress in epitaxial samples a compression by a factor of 0.89 is needed to enhance T_C to 250K, though real films have the possibility to partially compensate for in-plane-lattice parameter with the out-of-plane lattice parameter. Compression enhances the exchange interaction between the Eu 4f and 5d bands [56], and affects the O 2p-Eu 4f superexchange mechanism [55] resulting in higher T_C values. Schlom et al. [57] showed that the perovskite structured $BaTiO_3$ and $PbTiO_3$ out-of-plane lattice parameter expands $\sim 3\%$ when cooled below T_C giving the possibility to observe the predicted effects of strain.

A reduction of the Curie temperature can also be achieved, by depositing

EuO thin film with thicknesses lower than about 12nm. This was predicted by [58,59] using a combination of first-principles and model calculation based on the ferromagnetic Kondo-lattice model. They calculated the electronic structure of a single-crystal EuO(100) film, down to a single monolayer, as a function of temperature and thickness. For a single monolayer T_C as low as 15K is predicted. With increasing thickness the bulk value of 69K is reached at a thickness of 12nm. This can be intuitively understood, because the surface atoms have lower coordination number (=8 for this fcc structure) compared to that of the atoms in the center of the film (=12 for bulk). As thickness decreases surface atoms represent a larger fraction of the film and the T_C reduces due to fewer nearest-neighbor interactions of the surface atoms. Santos [36] was the first to experimentally show this effect with SQUID measurements of down to 1nm thick EuO films.

Chapter 2

Motivation and Overview

Apart from being a good candidate for spintronic applications EuO is a classical magnetic ideal for calorimetric measurements. Teaney [60] and Ahn [61] published heat capacity measurements on bulk EuO showing a sharp peak at the bulk Curie temperature. In order to measure thin films the nanocalorimetric measurements are necessary, performed in this thesis. As shown before epitaxial stoichiometric EuO is mainly deposited by MBE nowadays. One of the main issues of this thesis is the investigation of alternatives to this rather expensive deposition method, like sputter deposition, PLD and resistive thermal evaporation.

In chapter 3 a detailed description of the used deposition and characterization techniques is given. Several deposition methods have been used: Sputtering, thermal evaporation, MBE and PLD. X-ray and SQUID measurements are mainly used for confirmation of the crystalline and magnetic quality of our films. The oxidation states are measured by XPS. Nanocalorimetry is used to calculate the magnetic entropy and the polarization of the electron current is measured by the Meservey-Tedrow method.

Chapter 4 focuses on the first depositions by PLD, where due to the limitations of the used system epitaxial Eu_2O_3 is deposited. Nowadays, Eu_2O_3 is the most used of the europium oxides, mainly in microelectronic as high dielectric gates and optic-electronic devices due to its spectral transition between red- and white-luminescence states. Although Eu_2O_3 is used as a buffer layer, barely any research on epitaxial growth has been done.

In chapter 5 the attempts of EuO deposition by sputtering from a metal target are described. The effect of different substrates, inter- and capping layers is discussed. We show that the high reactivity of Eu inside the plasma leads to bad reproducibility of depositions.

In chapter 6 MBE deposited stoichiometric and doped EuO samples are presented. YSZ substrates have a perfect lattice match with EuO and are favoring epitaxial growth. Problems in the deposition on YSZ could be over-

come by introducing an MgO buffer layer enhancing crystallinity. Doping EuO with a very low percentage of Se surprisingly shows a large enhancement of the Curie temperature. As EuO is typically doped with lanthanides or oxygen vacancies, no model exists for this case. The mechanism for the enhancement of the Curie temperature by Se is discussed.

Chapter 7 presents the results of the first nanocalorimetric measurements on EuO deposited by PLD. Through continuos improvement of the measurement system, referring to design of the nanocalorimeters, the electronics and the software, ultra-fast adiabatic nanocalorimetric measurements could be performed starting at 20K. A mathematical formalism was developed to allow a more accurate calculation of the heat capacity. Thin films EuO could be measured in thicknesses down to a few nanometers, where size effects come to play.

In chapter 8 tunneling measurements through ferromagnetic insulating EuS barriers - similar to EuO barriers - are discussed. The effect of the interface between EuS and superconducting aluminium is investigated by introducing thin Cu and Si interlayers in SC-FI-SC junctions. A zero bias peak is observed, which is hysteretic with respect to an applied magnetic field. The origin of this feature is discussed.

Chapter 3

Experimental methods

Before carrying out tunneling experiments or nanocalorimetric measurements, the major challenge of the project had to be overcome. That is, a high-quality thin film, either a highly-oriented polycrystalor a single-crystalline EuO had to be prepared. To reach this aim arious deposition techniques, Pulsed Laser Deposition (PLD), Magnetron Sputtering, Thermal reactive evaporation and Molecular Beam Evaporation (MBE), were attempted along the project. Sputtering and Thermal evaporation were carried out at MATGAS, MBE was done during two short stays at the Francis Bitter Lab in Cambridge, and PLD was carried out both at CIN2 and, finally, at the University of Twente during a short stay. To determine the quality of the film structural, magnetic and transport properties were measured. This chapter details the film deposition procedures and techniques employed to characterize the films.

3.1 Deposition methods

During this thesis different techniques have been used in order to achieve the growth of high quality EuO or Eu_2O_3 thin films. In this chapter the main deposition techniques and the setups used along this work are briefly introduced.

3.1.1 Pulsed laser deposition (PLD)

This is a relatively recent technique (used since 1987) that relies on the use of a pulsed laser to generate the atomic species that constitute the thin film. Its major outcome is that due to the high energy of the ejected particles and the precise control of the laser power, epitaxial films of oxides and other materials can be grown with a monolayer control.
In pulsed laser deposition the target material is vaporized by focusing a laser beam on its surface. The target is mounted on a rotating plate in order to

allow a uniform ablation of the surface. Within nanoseconds the ablated material expands until it condenses on the substrate to form a film. To form oxides the system has the possibility of introducing oxygen or other gases during deposition. In general the PLD has higher deposition rates than i.e. magnetron sputtering, with the drawback of bad uniformity on big substrates. In the frame of a collaboration with J. Santiso (CIN2) we

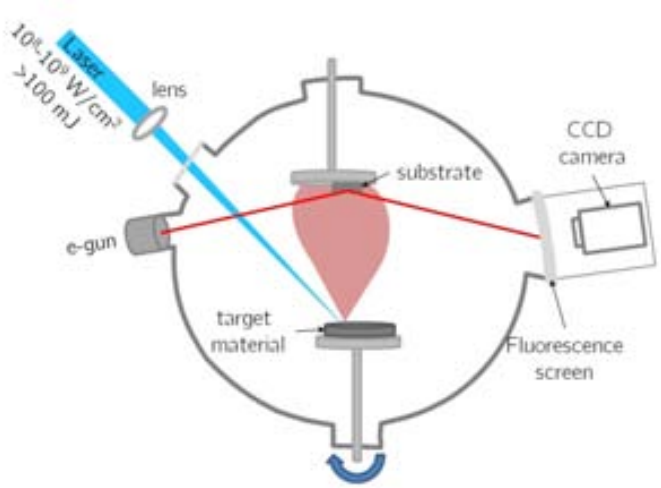

Figure 3.1: Schematic of the Pulsed Laser Deposition system at the CIN2 with an incorporated RHEED.

use the PLD system installed at CIN2[1]. It incorporates an *in-situ* RHEED (reflection high energy electron diffraction technique), Fig. 3.1. This setup allows depositions of ultrathin films with a nanometer scale thickness control and *in-situ* RHEED analysis provides information about the crystalline structure (orientation, lattice parameter, defect distribution, strain) during deposition. The base pressure is in the range of 10^{-6} Torr, when heating the substrate. The equipment also posses a carousel with 4 target allowing for a multi-layered growth.

No phases other than Eu_2O_3 are deposited in this system, as the base pressure is high enough to oxidize the target materials upper layers even during deposition. During this thesis EuO was deposited successfully in a UHV PLD [28,30], vacuum conditions which cannot be reached at the CIN2. Results are shown in section 4.

To guarantee the growth of high quality EuO several films were deposited also by PLD at the University of Twente in the group of Prof. Brinkam [28].

[1]Centro de Investigacion en Nanociencia y Nanotecnologia, Campus UAB, 08193 Bellaterra, Spain

This UHV-PLD setup reaches vacuum conditions not attainable in the PLD setup located at CIN2. In addition, this setup incorporates complementary characterization tools that allow in-situ monitoring of various characteristics of the grown films. The COMAT incorporatesa combination of PLD, RHEED, AFM, and XPS in one system. At the university of Twente the COMAT incorporating a combination of PLD, RHEED, AFM, and XPS in one system is used to grow thin EuO films. With a base pressure of 10^{-9}Torr and an incorporated RHEED the system is optimally equipped. The sample can also be transferred to an XPS chamber without breaking the vacuum. The exact setup of this system is described in Joost Beukers thesis [62]. The main results obtained with this system are described in section 7.

3.1.2 Sputtering

The commercial AJA sputtering system in MatGas[2] shown in fig. 3.2 is equipped with 4 magnetron sputtering sources and 2 thermal evaporators, which can all be used for co-deposition. With a base pressure of $< 5\text{x}10^{-8}$Torr, it is compareable with equipments for thermal evaporation (see next chapter). The substrate can be heated until 800°C. N_2, Ar, H_2 and O_2 can be introduced in the deposition chamber. An oscillating quartz crystal is used to calibrate and control the growth rates, which depend on the argon working pressure and the sputter voltage. The substrate can be rotated to permit the deposition of uniform films.
A mass spectrometer is also installed in the chamber, to measure the composition of the vacuum at pressures below 10^{-6}Torr. As a working pressure of $10^{-2} - 10^{-3}$Torr is needed to create plasma, the mass spectrometer can only operate before and after the deposition. The deposition of Europium leads to a reduction of the CO_2 and H_2O content of the chamber. When depositing consecutive samples in a run the starting conditions can therefore vary and lead to problems of reproducibility, as EuO is extremely sensitive to the O_2 partial pressure. To improve the base pressure, a cold finger was introduced into the main chamber. The finger acts as acts as a LN_2-trap to quench heavier gases, such as CO_2 and H_2O.

3.1.3 Thermal reactive evaporation

Thermal evaporation is a simple technique where the material to be deposited is heated until the vapor pressure creates a flux of particles that matches the desired deposition rate.
The Sputtering chamber, described in the chapter before, is also equipped with two thermal evaporation sources. A thin sheet of tungsten is used for resistive evaporation controlled by adjusting the applied power. The oscillating crystal is also used for monitoring the deposition rate and film thickness

[2]MATGAS Research Centre, Campus UAB, 08193 Bellaterra, Spain

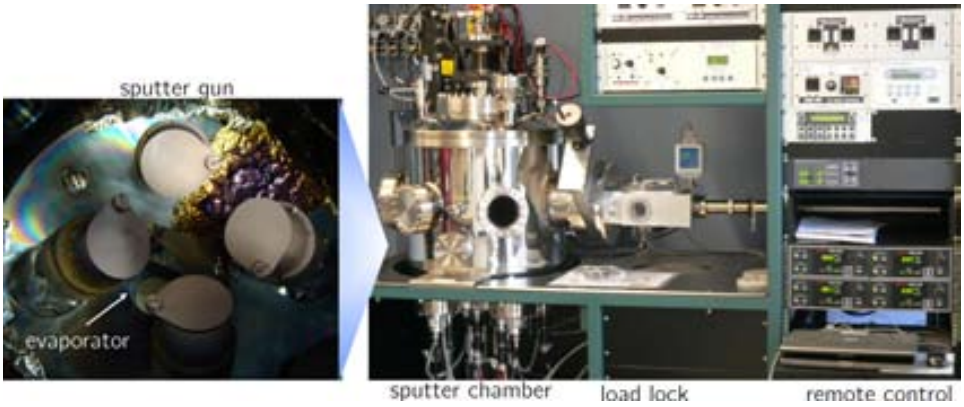

Figure 3.2: The commercial sputtering system located at MatGas incorporates one AC and three DC sputter guns and 2 thermal evaporators, which can all be controlled remotely.

in situ. In comparison with the evaporation system used at MIT(described below), the power introduced in the heated boat is controlled by a rotating knob and does not allow fine adjustment.

The EuS tunnel junctions were fabricated at FBML[3] using a custom-built [6], thin film vacuum deposition system. This chamber combines thermal evaporation with e-beam evaporation. Electrons are emitted from heated filaments of the gun source and a transverse magnetic field is applied in order to deflect the electron beam in a circular arc and focus it on the material to be evaporated, which has to be grounded and water-cooled.
A schematic is shown in fig. 3.3. The base pressure of this high-vacuum chamber is 6x10^{-8} Torr. The system has five resistively heated, thermal evaporation sources, all mounted on a rotating platform, and a three-hearth, electron-beam evaporation source. Only one material can be evaporated at a time monitored by an oscillating quartz crystal, and the material to be deposited is positioned directly beneath the substrate, at a distance of about 40 cm. The main characteristic of this system is the incorporation of a set of shadow masks that permit to fabricate in-situ the structure of the tunnel junction by sequential evporations. The shadow mask system is interchangeable, and can hold up to six beryllium-copper masks. The mask to be used is positioned directly beneath the substrate and then raised to be in contact with the substrate. The substrate is mounted onto a copper substrate holder, which can be cooled by a liquid nitrogen flow

[3]Francis Bitter Magnet Lab, Massachusetts Institute of Technology, Cambridge, 02139 Massachusetts, USA

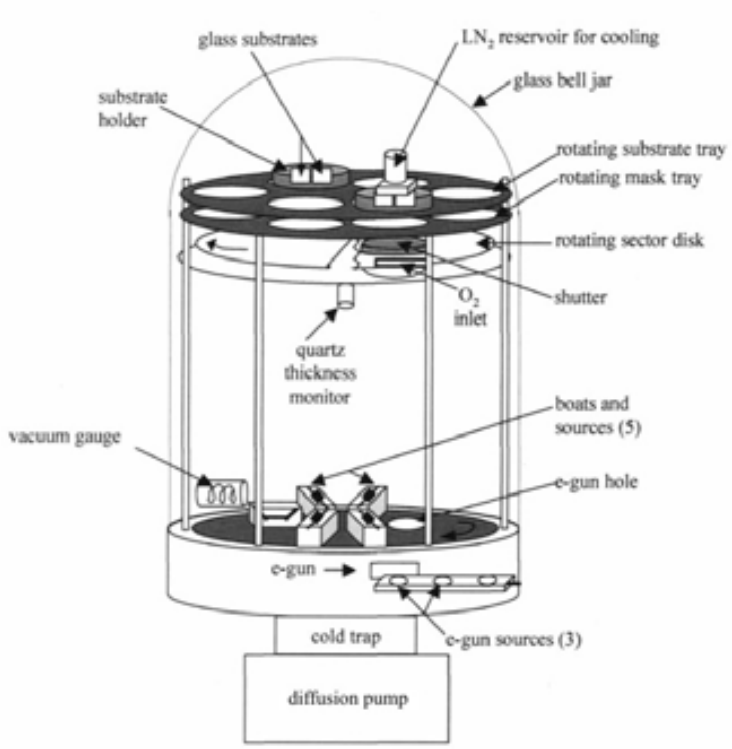

Figure 3.3: Schematic from [39] of the thin film evaporation chamber used for tunnel junction fabrication. 5 resistively heated sources and 3 electron-beam sources are placed at the bottom of the chamber. The shadow masks are located at the top. The substrate can be cooled by liquid-nitrogen. Film thickness is monitored by an oscillating quartz crystal.

3.1.4 Molecular beam epitaxy

Molecular beam epitaxy (MBE) systems are ideally suited for epitaxial growth due to low growth rates and UHV which allows great control of the deposition parameters. The material to be deposited is heated to provide a suitable vapor pressure in an isothermal enclosure. Molecular effusion from an aperture in the end of the cell gives rise to a cosine intensity distribution. The deposition rate is extremely stable being determined by the temperature of the furnace. The custom-built MBE system used at the FBML is shown in figure 3.4 and reaches a base pressure better than $8\text{x}10^{-11}$Torr. Up to four Knudsen cells and two five-pocket electron beam evaporation sources permit the evaporation of up to four materials simultaneously. It has a home-built masking system accommodating eight masks in-situ (with a feature size < 100 μm). The substrate can be heated up to 673 K and cooled down to 80 K. The UHV load-lock chamber is equipped with plasma

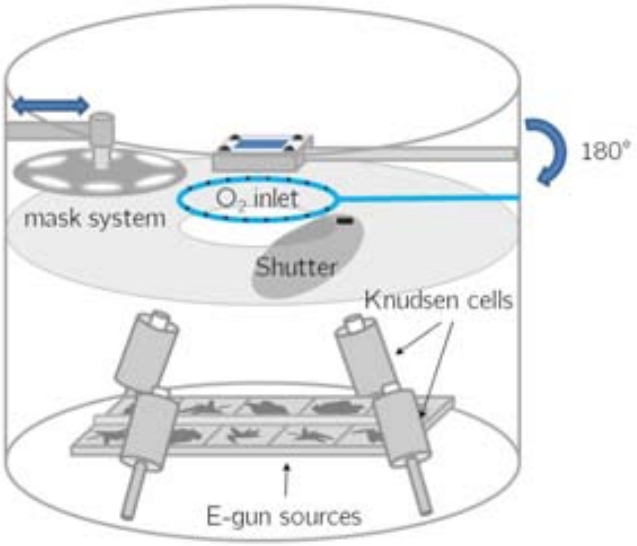

Figure 3.4: Schematic of the used MBE system.

oxidation/nitridation and an RF sputtering source.

3.2 Characterization methods

3.2.1 Structural analysis

X-ray measurements are a non-destructive analysis and a very powerful tool to identify crystalline phases and structures of crystalline films, such as epitaxy, strain, grain size and defects. X-Ray Reflectivity (XRR) also allows to determine the film thickness, including multilayers.
The basic principle on which the X-ray analysis of crystalline structures is based is the Bragg condition for constructive interference. When the x-rays scattered by the atomic planes d_{hkl} interfere constructively, a diffraction peak is observed satisfying the equation:

$$n\lambda = 2d_{hkl}\sin(\Theta_{hkl}) \tag{3.2.1}$$

where λ is the x-ray wavelength (normally for Cu 1.54Å), $n \geq 1$ is an integer and Θ_{hkl} is the angle between the atomic planes and the incident (diffracted) beam.

For complete characterization of the sample most diffractometers have four degrees of freedom as shown in figure 3.5 :

2-Theta (2Θ) is the Bragg angle between incident beam and diffracted beam, also angle between beam trap and detector shown in figure 3.5.

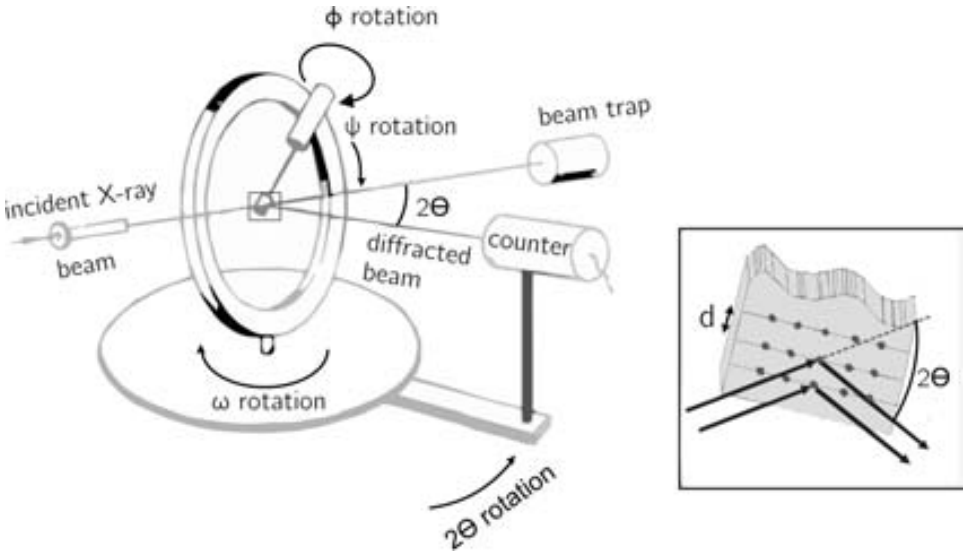

Figure 3.5: Adapted from the Image courtesy of the International Union of Crystallography, sketch of the 4 degrees of freedom in a four circles goniometer for X-ray analysis. Inset: principle of diffracting planes for Bragg condition.

Omega (ω) angle between incident X-rays and sample surface.

Psi(ψ) sample tilt around the direction given by the intersection between the sample surface and the diffraction plane. Rotates in the plane normal to that containing omega and 2-theta. This angle is also sometimes also referred to as Chi(χ).

Phi(ϕ) in-plane sample rotation, rotation around the normal of the sample surface.

X-ray analysis can be performed in symmetric or asymmetric geometry. In the first case the sample surface is positioned symmetrically to the source and detector. This means that the relationship between ω and Θ is fixed to $\omega = 2\Theta/2 = \Theta$, the detector rotates at twice the speed of the sample. In this configuration only the sample's surface can be analyzed. In the other case, additional rotation around any other angle brings other planes, not parallel to the surface, into Bragg condition. For this thesis the following measurements have been performed, if not indicated otherwise, with the PANalytical X'Pert equipment in collaboration with the CIN2 [4]:

Theta-2Theta ($\Theta - 2\Theta$) This scan is realized keeping the relationship $\omega = \Theta$ fixed while changing the values of ω. When Θ reaches a value

[4]Centro de Investigacin en Nanociencia y Nanotecnologia, CIN2 (CSIC-ICN), Campus UAB, 08193 Bellaterra, Spain

associated to a family of planes d_{hkl} the Bragg condition is complied and a peak shows up in the diffraction pattern. This is the standard analysis to investigate the orientations of a crystalline film, which also allows to extract information about the grain sizes and relative amount of phases with different orientations. Using MAUD [5] quantitative analysis between EuO and Eu_2O_3 was performed.

Rocking curve, also ω-scan Rocking curves were mainly used to align the diffraction system with respect to the planes of interest. By fixing 2Θ and changing ω information about the misalignment of certain family of planes can be obtained from the width of the diffraction peak. In a perfect crystal the width of a sharp peak would indicate the resolution of the diffraction system.

Glacing angle X-ray Reflectivity (XRR) X-rays are totally reflected at incidence angles smaller than the critical angle, because their refractive index is less than 1. The reflection at the surface and interfaces is due to the different electron densities in the different films (materials), which corresponds to different reflective indexes in the classical optics. By variation of the incidence angle $\omega = \Theta$ just above the critical angle the penetration depth of the X-rays varies and the reflection from the different interfaces interfere to give rise to interference fringes. This allows to determine thickness, roughness and density of the films.

Phi-scan (ϕ-scan) For the ϕ-scan a family forming at an angle α with the surface of the sample is considered and the values of ω and 2Θ are fixed in a way so that $\omega = 2\Theta/2 + \alpha$ while changing ϕ. Hence this is an asymmetric measurement. This measurement allows to see the alignment of the substrate with the film. During this thesis also in-plane ϕ-scans have been performed so see the distribution of orientations, as the substrate peaks of YSZ were overlapping exactly with the peaks of EuO.

GADDS - General Area Detection Diffraction System The measurement in a GADDS system[6] differs from that of the X-ray system described before in the sense that an area detector allows to obtain information about big regions of 2-Theta all at once. For the measurement of a certain area the sample must be orientated in the x-ray beam using a CAD camera and a laser beam. This allows microdiffraction to be done on small regions of a sample. Data can be fast detected due to a 2-dimensional detector with a large 2-Theta and Psi-range being ideal for doing rapid, crystallographic texture analysis of samples, including

[5] MAUD - Materials Analysis Using Diffraction, http://www.ing.unitn.it/ maud/

[6] Bruker-AXS diffractometer, model D8 Advance with GADDS- 2D Detector Diffraction System

thin films. The system works in a horizontal Theta-2Theta configuration and is the fastest way to measure pole figures. Alternatively pole figures can also be measured with a standard X-ray equipment.

3.2.2 X-ray Photoelectron Spectroscopy (XPS)

The phenomenon is based on the photoelectric effect outlined by Einstein. An X-ray photon with the energy $E_v = hv$ is absorbed by a surface atom leading to ionization and the emission of an electron. The electron ejected from the sample surface has a kinetic energy of $E_k = hv - \phi - E_b$, where ϕ is the work function (which gives the minimum energy required to remove an electron from the surface) of the material and E_b the binding energy. The kinetic energy of the electron is measured using a hemispherical analyzer. The binding energy of the peaks are characteristic of each element and can be measured by correcting for the workfunction of the material. The peak areas can be used (with appropriate sensitivity factors) to determine the composition of the materials surface. The shape of each peak and the binding energy can be slightly altered by the chemical state of the emitting atom. Hence XPS provides chemical bonding information as well.
For the measurement at the University of Twente, where the bare EuO surface can be measured after deposition without exposing the sample to air, an Omicron XPS system with an excitation energy of 1485 eV (Al Kα) is used. *Ex-situ* measurements of multilayers were performed using a PHI ESCA-5500 Spectrometer equipped with a monochromatic Al Kα source. In this case the surface has to be etched with an argon gun in order to access deeper sample layers.

3.2.3 Secondary ion mass spectrometry - SIMS

SIMS is used to analyse the composition of thin films by bombarding the sample surface with an ion beam followed by mass spectrometry of the emitted secondary ions from the sample. It allows to identify all elements, even light elements such as H and He and trace them in solid materials (specially thin films) as a function of depth. Also elements present in very low concentration levels, such as dopants in semiconductors, can be detected.
During SIMS analysis the sample surface is sputtered away with typical rates of 0.5 to 5 nm/s. Depending on the energies used in the process atoms from the sample's outer monolayer can be driven in about 10 nm, thus producing surface mixing. The fraction of sputtered atoms that become ionized (ion yield) can vary over many orders of magnitude for the various elements, further the presence of oxygen in the sample enhances positive ion yields for most elements. The proper choice of primary ion beam is important in enhancing the sensitivity of SIMS. Oxygen is usually used for sputtering electropositive elements or those with low ionization potentials such as

Na, B, and Al. Cesium atoms, on the other hand, are better at sputtering negative ions such as C, O, and Se. As a result, in order to get a reliable quantitative analysis some calibration measurements have to be performed beforehand.
The depth profiles of Se doped 10nm EuO thin films were performed at the University of Barcelona using 1-2kV Cs^+ atoms for sputtering for detecting Se impurities in different layers of the sample. The negative and positive ions ejected from the sample are measured separately.

3.2.4 Rutherford Backscattering Spectroscopy (RBS, also high-energy ion scattering spectroscopy - HEIS)

RBS is a widely used nuclear method for anaysis of the near surface layers of solids. Originally, Ernest Rutherford used the backscattering of alpha particles from a gold film in 1911 to determine the fine structure of the atom, resulting in the discovery of the atomic nucleus. It took 46 years for the first use of RBS for material analysis by Rubin *et al.* [63]. It is a nondestructive method and has a good depth resolution of the order of several nm. It also allows the quantitative determination of the composition of a material without the need of a reference sample and depth profiling of individual elements. For heavy elements a high sensitivity in the order of parts per million (ppm) can be achieved.
The technique is based on bombarding a sample with a mono-energetic beam of ions, with energies in the range 0.5 to 5 MeV, which elastically scatter and measuring energy of the backscattered ions. Usually protons, ^{4}He, and sometimes lithium ions are used as projectiles at backscattering angles of typically $150° - 180°$. The energy of the backscattered particles is related to the depth and mass of the target atom, while the number of backscattered particles detected from any given element is proportional to concentration. In the laboratory system the energy of the backscattered particle E_1 and mass M_1 with incident energy E_0 is given by $E_1 = KE_0$, where K is the kinematic factor $K = [(M_2 - M_1)/(M_1 + M_2)]^2$ for a scattering angle of 180°. Additional energy loss terms have to be subtracted for deeper layers, as the incident ion loses most of its energy through interactions with electrons (i.e. due to electronic stopping), mainly by ionization and excitation of target electrons. The energy loss per depth (dE_0/dx [eV/nm]) is given by the stopping cross section $\epsilon = 1/N \cdot dE_0/dx$. The film thickness can be directly related to the energy loss, given that N (atoms/cm^2) the 2-D density of the film is known. This slowing down of the ions is accompanied by a spread in the beam energy and is called straggling. But also other effects such as channeling have to be taken into account when interpreting the data.
The program SIMNRA [64] used in this thesis is a powerful tool for simulating RBS spectra. The measurements were performed at CMAM with the 5

MV tandem accelerator using a He beam at two different energies, 1500 keV and 3035 keV. The lower energy beam gives higher accuracy in the depth resolution, while the higher energy beam enhances the mass resolution of the measurement.

3.2.5 Superconducting Quantum Interference Device - SQUID

DC SQUID measurements are based on the DC Josephson effect and can be used to measure changes in the magnetic field with extremely high sensitivity. It consists of a superconducting loop having two small separating oxide barriers connected in parallel (DC SQUID). SQUIDs are magnetic flux-to-voltage transducers, converting the magnetic flux, which is hard to measure, into voltage, which is easy to measure. A fundamental property of superconducting rings is that only magnetic fluxes that are multiples of the magnetic flux quantum, $\Phi_0 = h/2e = 2 \times 10^{-15}$ Wb, can flow in a superconducting ring. In other words, an external magnetic field can penetrate a superconducting loop only if the magnetic field is an integer multiple of the magnetic flux quantum. In absence of an magnetic field an electrical bias current I splits in two equal parts $I/2$ for every branch. When applying an external magnetic field the screening current I_S in the superconducting ring results in $I/2 + I_S$ in one branch and $I/2 - I_S$ in the other branch, changing direction every $\Phi_0/2$. If this current is higher than the critical current of the Josephson junction the junctions get normal conducting and a voltage drop can be measured. As the screening current is periodic in the applied flux, the SQUID's critical current is periodic in the applied magnetic flux. This oszillations can be sensed by measuring the voltage drop over the superconducting ring.
The magnetic behavior of our films was measured with a "Quantum design MPMS XL-7T" operating in RSO (Reciprocating Sample Option) mode, which reaches a magnetization absolute sensitivity of 1×10^{-8} emu, located in the ICMAB. One can measure magnetization of the sample as a function of temperature (4 K to 400 K range) and applied magnetic field ($\pm$70000 Oe). Due to the large saturation moment of 7 μ_B per Eu^{2+} ion, an EuO film with an area of 25 mm^2 and thickness down to 1 nm could be measured. As SQUID measurements give the magnetization for the whole sample including substrate, buffer and capping layers, the linear magnetization of the para- and diamagnetic layers was measured and subtracted from the sample to obtain the behaviour of the EuO.

3.2.6 Meservey-Tedrow method

Characterization of the transport properties are performed using the Meservey-Tedrow method [65]:
In 1971 Meservey and Tedrow [66] published a spin-polarized electron tun-

neling technique which uses properties of the superconducting states to probe spin-dependent features of electron density of states of magnetic metals. An insulator (I) is placed between a ferromagnetic metal (FM) and a superconductor (S) and a magnetic field is applied. Normally the conductivity of the FM/I/S junction is measured below the critical temperature. The tunneling conductance of the junction is determined by the convolution of the density of states (DOS) of the ferromagnet and the superconductor. The tunneling current is described by the general formula, where M is the tunnel matrix (assumed energy independent in the region of interest), N_x is the density of states of the electrode x and f is the Fermi function:

$$I(V) \sim |M|^2 \int_{-\infty}^{\infty} N_1(E-V)N_2(E)[f(E-V)-f(E)]\,dE \tag{3.2.2}$$

In case of a superconducting electrode

$$N_S(E) = \begin{cases} \frac{N_N(E)E}{(E^2-\Delta^2)^{1/2}} & |E| \geq \Delta \\ 0 & |E| < \Delta \end{cases} \tag{3.2.3}$$

The superconductor shows a sharp peak at the gap energy and is symmetric for spin-up and spin-down electrons. Applying a magnetic field parallel to the junction electrodes this peak is split by $\pm\mu_B$H. As shown in fig. 3.6 in the presence of H, the DOS is spin-dependent, allowing the superconducting Al to act as the spin detector. The tunneling conductance for the two spin directions is obtained by convoluting this split DOS. Changes in the tunneling probability between the spin-up and spin-down electrons can be measured. Aluminum is the S used for this measurement because it has low spin-orbit scattering, and thus long spin lifetime, and a high critical field of about 5 Tesla depending on the film thickness.

Measuring polarization of the tunnel current from a FM through an insulating barrier has been extensively practiced with the use of a superconducting aluminum electrode as the spin detector. Instead of using a FM as the source for spinpolarized electrons, we use a ferromagnetic tunnel barrier of EuS and introduce several additional interlayers X of Cu or Si to study the surface effects in a Al/X/EuS/Al junction. We choose relatively light elements as the Abrikosov and Gor'kov theory [67] suggests that spin-orbit scattering increases approximately as Z^4, where Z is the atomic number. For the measurements our junctions were fully submerged in a pumped liquid He4 bath, where the temperature can be adjusted by pumping between 4.2K and 0.9K. The dynamic conductance dI/dV was measured with two terminal as well as 4 terminals. A small AC voltage was superimposed onto the DC bias voltage across the junction. The change in AC current through the junction was measured by detecting the AC voltage across a series resistor with a lock-in amplifer (see schematic of the circuit fig. 3.6 from [39]).

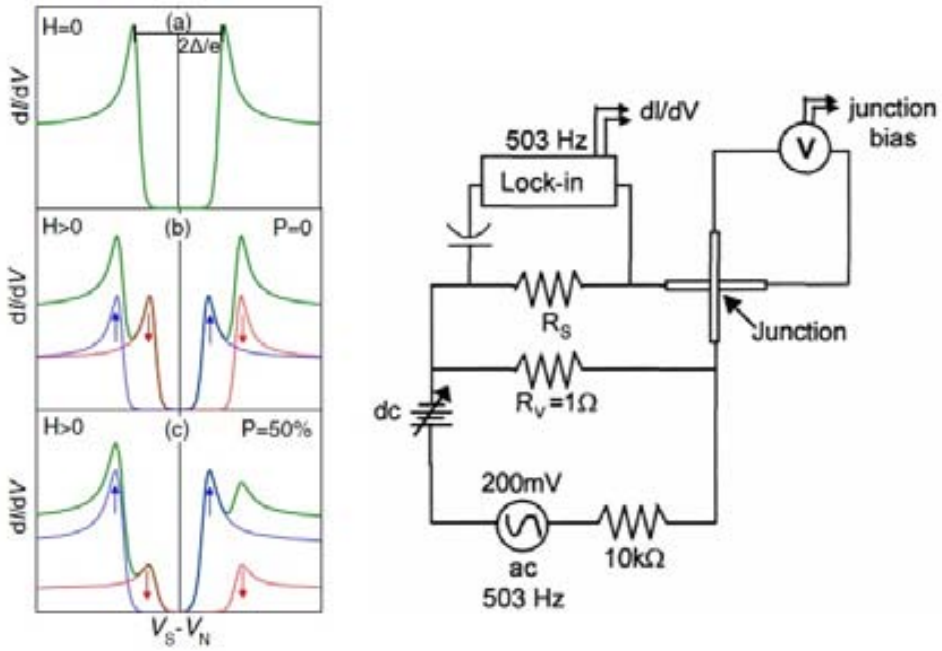

Figure 3.6: Adapted from [6]. For a superconductor/insulator/metal tunnel junction the typical tunnel conductance (green) is shown as a function of bias voltage across the electrodes. (a) At $H = 0$, the conductance reveals the superconducting energy gap centered at V=0 and the 2 peaks at $\pm\Delta/e$, corresponding to the quasiparticle DOS. (b) At $H \neq 0$ the Zeeman splitting lifts the degeneracy between the spin-up (blue) and spin-down (red) states. When P=0, for a nonmagnetic metal counter electrode, the measured (green) curve is completely symmetric. (c) At $H \neq 0$, in case of a ferromagnetic counter electrode, the spin-up DOS is greater than the spin-down DOS resulting in an asymmetric curve. The right figure shows the schematic of the used measurement circuit.

3.2.7 Quasi-adiabatic Membrane-based Nanocalorimetry

3.2.7.1 Introduction

Calorimetric measurements are based on the detection of the heat being absorbed or released from the material during any process. For more than 100 years calorimetry has been the most powerful tool for investigating thermodynamic properties. Conventional Differential Scanning Calorimetry (DSC) is limited to sample sizes > 1 mg. To investigate the properties of systems at the nanoscale (such as thin films, nanoparticles, etc.) nanocalorimetry is needed. With a sensitivity of about 10 pJ/K in heat capacity, nanoclaorimetry can be used to measure phase transitions in ultrathin films down to few

nm. These microsystems have already been demonstrated to work in the temperature range 10 K - 800 K in nearly adiabatic conditions [68], using DC sourcing and sensing at extremely fast heating rates (10^4-10^6K/s), AC nanocalorimetry with similar sensitivity has also been shown to provide accurate measurements of phase transitions [69].
Membrane-based calorimetry has already been used to study a few systems involving nanoscale materials, such as the size dependent melting point of isolated metal nanoparticles at relatively low temperatures [68], or the heat capacity of magnetic bilayers [70] or the glass transition in organic ultrathin layers [71]. The measurement of magnetic transitions by nanocalorimetry in ultrathin films of a ferromagnetic material,such as Ni, and antiferromagnetic, such as CoO, have been recently demonstrated by our group [72, 73]. Until recently few groups have managed to develop nanocalorimetric systems [72, 74–76] with enough reliability and sensitivity. The mayor difficulty in nanocalorimetry lies in detecting the low amount of energy involved in phase transitions of very small samples. In order to increase sensitivity, the heat capacity of the nanocalorimetric cell has to be minimized to make it comparable to the heat capacity of the sample and achieve a high signal-to-noise ratio (as shown later in fig. 7.8f. and 7.9f. where the red curve is raw signal).
To yield a measurable heat flow and minimize heat loss (adiabatic) due to conduction, convection and radiation, all measurements have to be performed in high vacuum ($<10^{-6}$ Torr) and at heating rates of about 10^4-10^6 K/s, since typical cooling rates are around 10^3K/s. Also the thermal link between the calorimetric cell and the sample is of great importance and has to be maximized to avoid any thermal lag during the calorimetric measurement. Finite element modelling has shown the thermal gradient between heater/sensor and a metallic thin film is at most 0.1 K during heating rates as fast as 10^5 K/s [77]. Another limitation is related to the sample thickness and heat conduction, as thick and poorly conducting films have large thermal gradients within the sample volume. More detailed information about the characteristics and setup of the used nanocalorimetric system can be found in Aitor Lopaendia's PhD thesis [78].

The calorimetric cell consists of an amorphous SiN_x membrane supported by a Si frame (fig. 3.7). On top of the membrane a thin metallic meander-shaped film is deposited forming heater and temperature sensor at once.
By introducing a current pulse through the metallic heater the calorimetric cell consisting of heater, membrane and sample is heated by the Joule effect while the Si frame with the contact pads remains at constant temperature acting as a heat drain. In this case, all Joule heat generated by the heater, is consumed by an increase in the temperature of the cell:

$$P(t)dt = C_P(T)dT \tag{3.2.4}$$

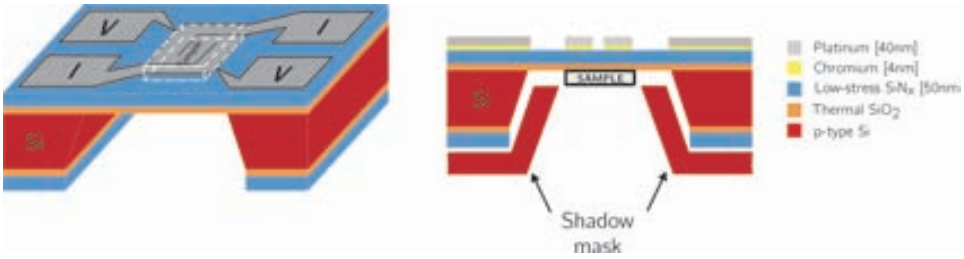

Figure 3.7: New generation nanocalorimeter, where current (I) and voltage (V) contacts are indicated. The meander-shaped heater is also used to sense the temperature. For deposition a shadow mask is fabricated allowing to deposit material only in the measurement area.

As the voltage is measured on the sensing pads (4 point technique) the change in resistance $R(t)$ of the sensing area can be easily obtained by taking $V(t)/I(t)$. The power can be calculated and the heat capacity can be obtained if the temperature of the sensor is calibrated T(R(t)). Further improvements on the measured signal can be made by measuring in differential mode with a vacant reference calorimeter as described in more detail in section 7.4.1

3.2.7.2 Microfabrication

In the last years the design of the nanocalorimetric cell has changed a lot as optimization of the thermal profile to more and more uniform heat distribution in the cell was performed. Starting with a U-shaped heater separated from the sensor to the meander shaped calorimeters of today a lot of work has been done by GNaM. The fabrication of the nanocalorimetric devices was done in collaboration with Prof. F. X. Muoz-Pascual from IMB-CNM using standard microfabrication technology. Starting from a double-sided polished silicon wafer, a 50 nm thick silicon oxide layer is thermally oxidized at 1000°C to avoid electrical shunting during operation or calibration of the devices. Then, 50-to-180 nm low-stress SiN_x is deposited by low pressure chemical vapor deposition at high temperature, i.e. 800°C, on both sides of the wafer. The bottom side is patterned by photolithography and plasma etched with SF_6 until the underlying Si. It is in the last step used as mask for the bulk etching of Si. The top side is also patterned for the metallic contacts and heater/sensor by photolithography. Subsequenty, 4 nm Cr and 40 nm Pt are deposited by electron beam on the top side and the photoresist is removed. Cr enhances the adhesion of the Pt heater. The wafer is then kept for 2 h in a furnace at 600°C in N_2 atmosphere to thermally stabilize the metallic films. In a last step the membrane is etched with KOH to get rid of the bulk Si.

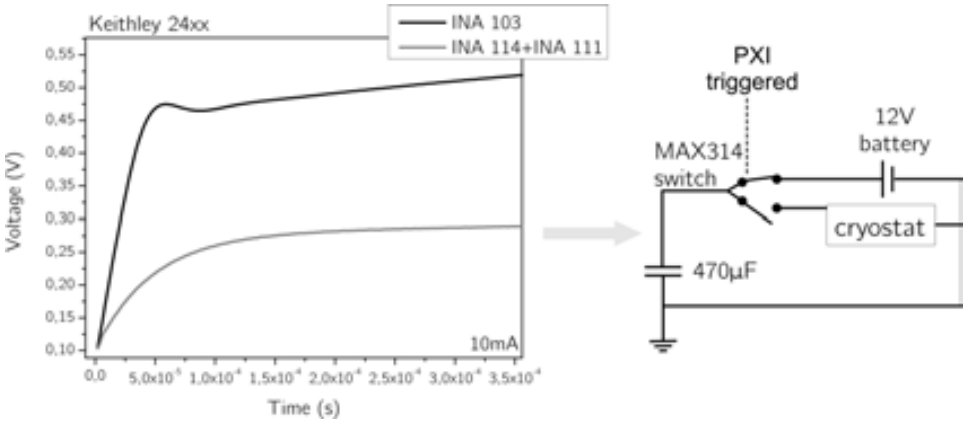

Figure 3.8: The first μs of a measurement of 2 different calorimeters is shown. The old setup INA 114 + INA 110 have a stabilization time of 0.2 ms. The INA 103 has a stabilization time of 10μs and shows the transient of the Keithley 2400 used in this measurement. The optimized design with the capacitance is shown on the right side. The triggering pulse is generated by the PXI that is also used to read the measured voltages at 500 Ksamples/s.

3.2.7.3 Low temperature nano-calorimetry

Usually a constant current pulse of various mA is generated by the Keithley 2400 and the nanocalorimeters response is amplyfied with a precision instrumental amplifier with a regulated gain (from 1x to 10000x), the INA 114[7]. For filtering high frequencies it is coupled with an INA 110[8]. During the experiments problems were experienced with this setup: EuO has a Curie temperature of 69 K and therefore requires low temperature measurements. By using the closed cycle He cryostat located in MatGas temperatures as low as 10 K can be reached. Due to the high heating rates inherent to the nanocalorimetric method, the measurement started, when the calorimetric cell had already reached a temperature > 60 K, which is too close to the T_C of EuO. Also, the Keithley 2400 current source has a small current overshoot before stabilizing at the desired current value. This can lead to bursting of the sensing connections.
The challenge was to develop faster electronics, which allow us to start the measurement earlier and hence at lower temperatures. The delay between the starting of the current pulse to the measurement of a constant current was limited by the amplification setup, as shown in figure 3.8. By fabricat-

[7]Burr-Brown, INA 114 precision instrumentation amplifier data-sheet. http://www.burr-brown.com/

[8]Burr-Brown, INA 110 Fast-settling FET-Input instrumentation amplifier data-sheet. http://www.burr-brown.com/

ing an electronic circuit using faster low noise amplifiers INA 103[9] this could be overcome. This amplifier only needs a stabilization time of 10μs. With the faster electronics we could then see the transient (shown in fig. 3.8) of the Keithley 2400 before reaching the desired current value. For further improvement the squared current pulse from the Keithley was no longer used. Instead Aitor Lopeandia and Manel Molina fabricated a capacitor source which incorporated in the system, as shown in fig. 3.8, introducing less noise and allowing us to start the measurement earlier (comparison between measurements with the Keithley 2400 and the capacitor source are presented in the section 7.4.1). The measurement software written by GNaM in Labview 8 also had to be adapted accordingly.

[9]Burr-Brown, INA 103 Low Noise, Low Distortion instrumentation amplifier. http://www.burr-brown.com/

Chapter 4

PLD deposited epitaxial Eu_2O_3 thin films

For the growth of epitaxial films, cubic (100) Yttria-stabilized zirconia (YSZ) with a lattice constant of 5.16Å[1] has an excellent lattice mismatch of 0.4% with EuO (a=5.142Å [79]) being the reason why we deposit on YSZ substrates. However this substrate has two mayor drawbacks. Europium monoxide is suspected to grow cube on cube on this substrate making it impossible to identify by standard Theta-2Theta x-ray scans as substrate and EuO peaks coincide (chapter 6.1). On the other hand YSZ can act as oxygen donor as observed by Schmehl et al. (supplementary information of ref. [2]) and lead to formation of higher oxides at the interface.
The groups that successfully grew EuO [28, 30] use a UHV-PLD system allowing them to reach base pressures as low as 10^{-9}Torr and then adjust the partial oxygen pressure to 1×10^{-7} and 10^{-6} Torr using a fluence of 0.4 and 2J/cm^2 and an a deposition frequency of 10 and 20Hz at a temperatures of 340°C and 300°C. These conditions couldn't be reached with the PLD system at CIN2 used for this work.

4.1 Introduction

In the last decade, as a member of rare earth oxide family, Europium Oxide (Eu_2O_3) has been largely investigated as a potential material for novel optical and electronic devices and applications [80–82]. Luminescence properties have been widely investigated for application in photoactive coating, optical storage data, and fluorescent displays. Besides it's intrinsically properties, implementation of the nanoscale in optical devices has been also evaluated in the form of Eu_2O_3 nanoparticles [83–85], polycrystalline thin film [86–88]

[1] from high resolution Theta-2Theta measurements

and even nanocrystalline mesoporous thin films [89]. Also for its integration in silicon devices, the study of interfaces to form europium silicate [87,88,90] and its optical properties are being widely investigated. Furthermore, Eu_2O_3 also present interesting electrical properties such as large dielectric constant, large band gap and high dielectric strength. Therefore, Eu_2O_3 films have been recently used in microelectronic devices as high dielectric gates [80,91]. Thin film preparation processes, from solution deposition [85, 92–94] to vapor phases techniques [84, 86–88, 91, 95] have thus been developed in last years to implement Eu_2O_3 in formerly described devices. Nevertheless, only Bellocchi *et al.*, using the sputtering process, has directly prepared films, in an as-deposited methodology, i.e. avoiding any further thermal treatment needed to obtain high quality films. Taking into account that perfect control of the film thickness and of the post-deposition processing have been pointed as essential for optimum properties, any preparation technique with extremely well controlled film thickness and quality is needed for a fundamental study of the material properties. For this fundamental approach, preparation of single crystalline films is also mandatory. To our knowledge, epitaxial Eu_2O_3 films have been only grown by solution deposition approaches on textured Ni [94], for YBCO tapes buffer applications, and on single crystal $LaAlO_3$ substrates [92]. In both cases, post-deposition thermal treatments up to 1000-1200°C were necessary to achieve high quality epitaxial films. We present the results of the preparation of epitaxial thin films at relatively low temperatures using the pulsed laser deposition technique. *In-situ* and *ex-situ* characterization techniques have been used to analyze the films texture as a function of deposition temperature reaching a high quality epitaxy for temperatures above 450°C.

4.2 Experimental

Our samples are deposited in a temperature range of 350°C - 650°C with a europium flux of 0.3Å/s (1Hz with 0.5J/cm^2) from a metal europium target. No oxygen is introduced in the chamber. The base pressure is 10^{-6}Torr, but during deposition argon is introduced rising the chamber pressure to 2×10^{-2}Torr. On all samples a capping layer of polycrystalline aluminum is deposited. X-ray diffraction (XRD) analysis was performed in a four-angle diffractometer with CuKα radiation after deposition. XRR and XRD have been performed to determine thickness and structure of the layers. *Ex-situ* pole figures of selected reflections along with in-situ reflection high-energy electron diffraction (RHEED) during initial growth stages allowed us to analyze epitaxial growth and relationships with the substrate.

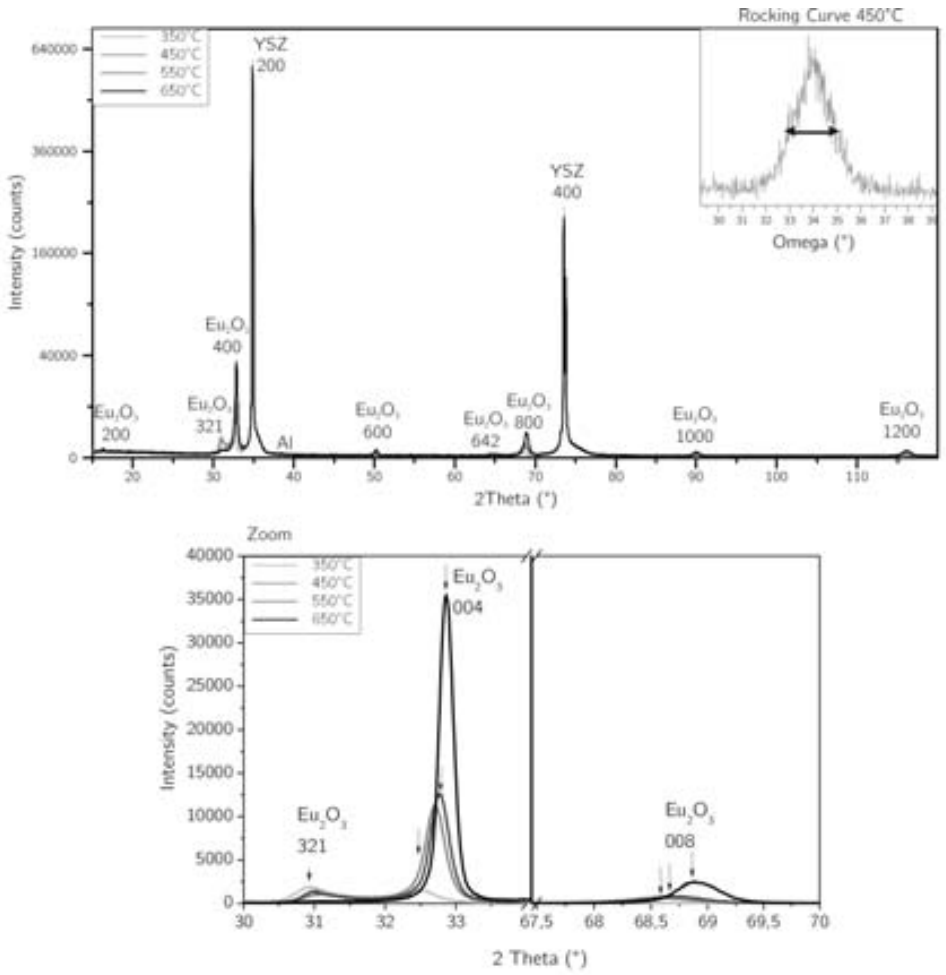

Figure 4.1: The XRD scan of Eu_2O_3 thin films on YSZ deposited at various temperatures is shown in the top figure. The inset shows the rocking curve of the sample deposited at 450°C. The bottom figure shows a zoom on the region of interest.

4.3 X-ray characterization

Figure 4.1 shows the Theta - 2Theta scan of all Eu_2O_3 films. Among peaks corresponding to the YSZ substrates only peaks corresponding to the cubic Eu_2O_3 are observed. Samples deposited at 650°C shows only reflections corresponding to a preferentially oriented (|00) films, while below this deposition temperature a small amount of crystals with the {321} orientation are also seen at 31°. By increasing the deposition temperature this amount clearly diminishes until vanishing at 650°C. High quality of the preferred out-

of-plane orientation was also confirmed by measuring 400 reflection rocking curves with a FWHM around 1.5° (see inset). As seen in the bottom figure of figure 4.1, by increasing deposition temperature a shift to higher angles of the $\{\ell 00\}$ reflection is observed. This corresponds to a systematic change in the out-of-plane lattice parameter of Eu_2O_3 (a⊥) with the annealing temperature.

The 2Θ angles measured for the 008 reflection and each deposition temperature are shown in the following table, where also the measured FWHM of the peak and the extracted out-of-plane cubic lattice parameter applying the Bragg's law are compared.

Temperature (°C)	2Θ (°)	FWHM (°)	c (Å)	Δc[1] (%)
350	68.267	0.900	10.982	1.05
450	68.563	0.671	10.940	0.67
550	68.700	0.599	10.922	0.49
650	68.897	0.441	10.892	0.24

[1] $\Delta c = (c - a_0)/a_0 \times 100$ where $a_0 = 10.868$Åcorresponding to the bulk Eu_2O_3 lattice constant

As the bulk value for cubic Eu_2O_3 parameters is $a_0 = 10.868$Å [96], we can see that film present an elongated out of plane parameter compared to its isotropic bulk structure but this elongation tends to diminish as the deposition temperature increases. As Eu_2O_3 (00ℓ) is expected to grow cube-on-cube on (00l) YSZ, the in-plane lattice mismatch taking bulk value is expected to be -4.97%, with a compressed in-plane structure, which will probably induce the elongation in the out-of-plane direction. The out of plane lattice strain is calculated as $\Delta a = (a - a_0)/a_0$ as shown in the table.

In-plane texture was analyzed by performing a pole figure at a 2Θ of 56.02° i.e. along the {311} direction. As shown in figure 4.2a, the experimental maxima adjust to the superposed simulated ones, represented by half transparent gray dots. The intensity peaking at $\psi = 25°$ corresponds to the fourfold degenerate 113 reflection and the intensity peaking at $\psi = 72°$ to that of degenerated 311 and 131 reflections. Figure 4.2b. shows the ϕ-scan of the {311} reflection extracted from the pole figure for ψ equal to 72° with an FWHM of 2.4°.

4.4 In situ - RHEED

RHEED analysis was performed with the primary beam along the [100] and the [110] axis of the YSZ substrate. By selecting the center spot, intensity as function of growth time can be measured. Unless, for samples deposited at 350°C, the period of oscillation corresponding to the growth of one monolayer (ML) is clearly observed for the other growth temperatures, indicating

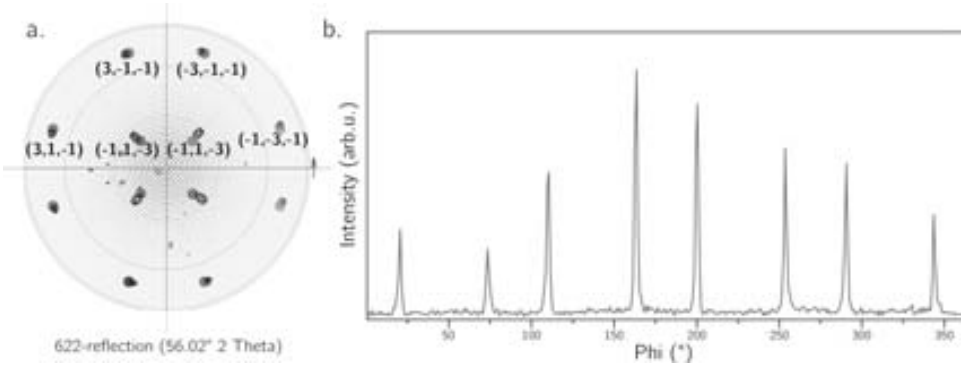

Figure 4.2: The pole figure in **a.** shows the expected fourfold symmetry of Eu_2O_3 in 622 direction for the sample deposited at 450°C. The extracted phi scan (**b.**) at $\psi = 72°$ shows a FWHM of 2.4Å.

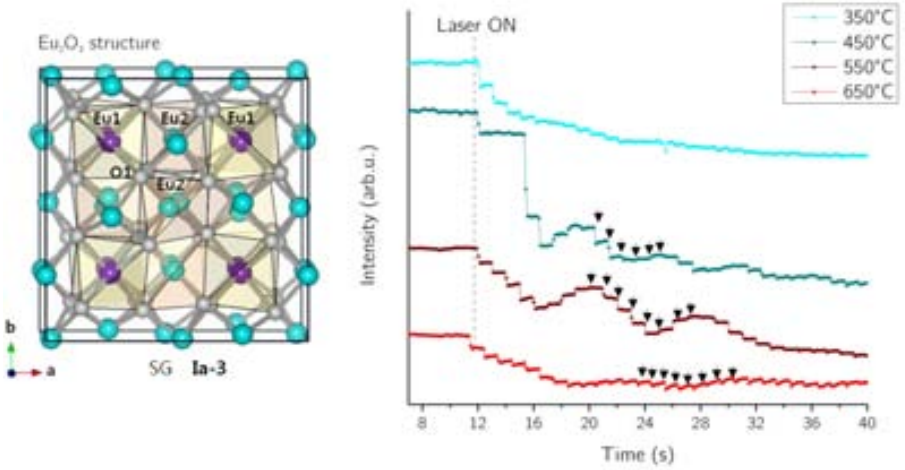

Figure 4.3: The schematic of the cubic Eu_2O_3 structure is taken from ref. [97]. It explains the definition that 1 monolayer corresponds to a/4. RHEED oscillations intensity variation during the first stages of Eu_2O_3 growth. A substructure related to the single laser pulses (marked arrows) is resolved.

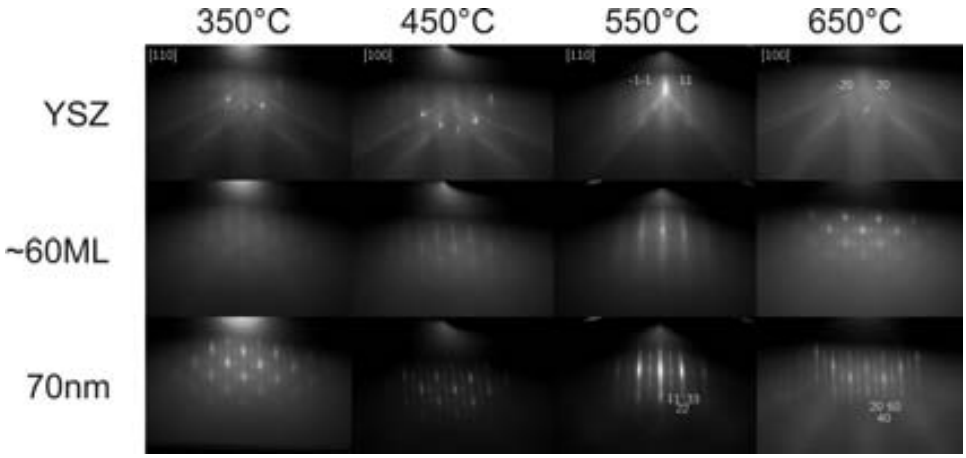

Figure 4.4: RHEED of YSZ is performed with the primary beam along the [110](for the sample deposited at 550°C) and the [100](other samples) axis. The in-situ RHEED images show the epitaxy relation between substrate and Eu_2O_3 along the 110 and 100 direction indicated for 550 and 650°C.

a layer-by-layer growth. As shown in figure 4.3, the oscillations at the initial growth stages are formed by several small maxima (see arrows), related to each laser pulse, enveloped by a wider maxima associated to the formation of a monolayer (ML). Interestingly in the very first stages of growth, for films deposited at 450°C only ~ 6 pulses are needed to form a ML, while for 550°C and 650°C, ~ 8 pulses are needed.
Thickness of film deposited at 450°C was determined by XRR in 74 nm. As 2050 pulses were used to grow the film, we can estimate its growth rate in 0.36 Å/pulse, and thus the formed monolayer height can be estimated in 2.16 Å, that cannot be associated to any clear atomic stack of the EuO or Eu_2O_3 lattice. For higher temperatures, the heights of the monolayer are estimated around 2.53 Åthat can correspond to 1/4 of the cubic Eu_2O_3 cell. For better understanding in figure 4.3 the crystalline structure of Eu_2O_3 is shown. The successive Eu/O/Eu stacking suggests that one monolayer of Eu_2O_3 is 2.59Åcorresponding to $a/4$, where a is the bulk Eu_2O_3 lattice constant.

To better understand the first stages of growth, we show (figure 4.4) the RHEED patterns along the [001] and [110] direction of the YSZ substrates at first stage of growth ~ 60 ML and after 70 nm comparing its location and intensity can be compared with the theoretical one shown in figure 4.5a.

The RHEED patterns of the YSZ substrate with typical Kikuchi lines, allowing aligning the sample surface with the electron beam, are clearly observed. Also, for ~ 70 nm thick films, the four photographs show the

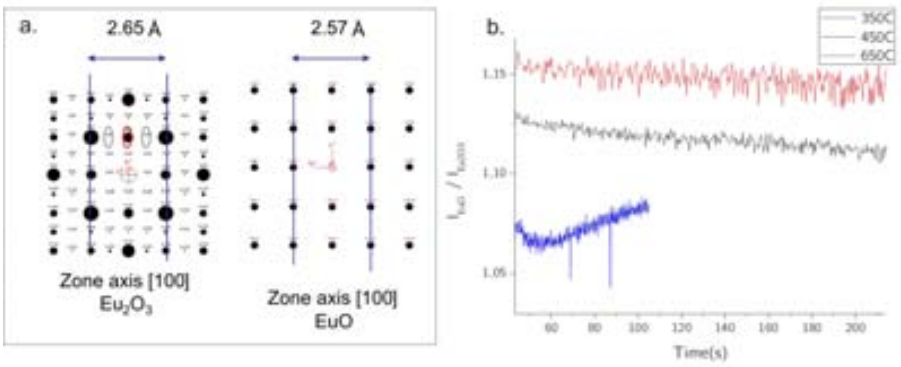

Figure 4.5: a. shows the theoretical RHEED patterns of the [100] zone axis for the EuO and Eu_2O_3 cubic structure. The grey ellipses indicate the formation of Eu_2O_3, while the red ellipse indicates a position that could also be attributed to EuO. Figure b. shows the evolution in time of the relative intensities of peaks that are attributed to Eu_2O_3 and peaks may be attributed to EuO.

RHEED pattern of the Eu_2O_3 structure confirming the Eu_2O_3 cubic structure determined by XRD. The samples show an increasing crystal quality (more intense diffraction pattern) with temperature. Films deposited at low temperatures show a diffraction pattern consisting of defined spots, which are a direct consequence of the surface roughness associated with the formation of 3D islands. Conversely, films grown at higher temperatures show streaks (in the image of 70nm) indicating a progressive flattening of surface morphology. The streak lines of the Eu_2O_3 and YSZ appear in identical position in the RHEED pattern confirming in-plane epitaxial growth on YSZ. As (110) and (100) lines indexed in figure 4.4 of the film and the substrate are parallel, we can extract the epitaxial relationship as: $Eu_2O_3(400)\|YSZ(200)$ and $Eu_2O_3(220)\|YSZ(110)$, confirming the expected cube-on-cube lattice growth.

The diffracted patterns of about 60 ML($\equiv$ 15nm) samples deposited at T$<$ 650°C may indicate the formation of EuO (only main spots, absence of secondary spots),in early stages of growth. Thicker films already show clear secondary spots consistent with the formation of Eu_2O_3 phase. The distance between spots of this supposed EuO films is identical to that of YSZ confirming that such interface is growing epitaxial, which could perfectly be the case of EuO due to its perfect lattice matching with the substrate (a_{EuO}=a_{YSZ}=5.14 Å). Therefore the observed lack of secondary spots may be assigned to the presence of a EuO buffer layer. Nevertheless, the non observation of secondary spots at the beginning of the analysis in some samples

can be simply associated to an initial spot intensity below the detector resolution. To confirm if EuO buffer layer is effectively growing during the first stage, we analyze as a function of time the relative intensity of a spot exclusively related to the presence of the Eu_2O_3 structure a secondary plot - and a spot that can be assigned either to EuO or to Eu_2O_3. As can be seen in figure 4.5b., the ratio I_{EuO}/I_{Eu2O3} for films deposited at 450 and 650°C is almost constant with deposition time confirming the presence of a unique Eu_2O_3 phase. On the contrary, samples prepared at 350°C show a variation of the ratio as a function of time, with a large ratio at the beginning, indicating the probable presence of a second phase which can be assigned to EuO at the interface between Eu_2O_3 and YSZ. Note that we could not use the sample deposited at 550°C in this analysis because of the different crystallographic orientation used for its RHEED characterization that gives very intense spots in comparison with the formers ones.

4.5 Conclusions

Epitaxial Eu_2O_3, with a FWHM of ϕ of 2.4° and ω of 1.5°C (at 450°C), was grown successfully by PLD at several temperatures. were successfully grown on YSZ by PLD. The growth was monitored by *in-situ* RHEED showing extremely flat cube on cube growth of Eu_2O_3 (00ℓ) on YSZ (00l) substrates, where the Eu_2O_3 lattice constant matches twice the lattice constant of YSZ. XRD analysis shows a change of the thin film lattice constant with increasing temperature towards the literature value. This is expected due to the better relaxation at higher temperatures. A precise analysis of the RHEED pattern as well as the evolution of the spot intensity with time, for the initial stages of growth of the films has allowed us to determine that films deposited at 350°C, a buffer EuO layer may be present between the YSZ and the Eu_2O_3 interface. For higher deposition temperatures a sharp interface seems to exist between YSZ and the Eu_2O_3 film.

Chapter 5

Sputtered europium oxide films

Sputtering has grown to be the most widely used vacuum deposition technique due to the possibility of depositing uniformly over big areas. In industry, sputtering is the standard technique to manufacture magnetic hard disks and the possibility of growing EuO thin films with this technique is therefore favorable. However, sputter deposition of EuO thin films is a great challenge. During this thesis only one group [31, 35] managed to grow 80% EuO thin films by RF cosputtering Eu_2O_3 and metal Eu in an UHV vacuum chamber ($P_b = 4 \times 10^{-9}$Torr). Several approaches to deposit thin EuO films by DC sputtering from a metal target have been tempted.

5.1 Deposition conditions - experimental

The base pressure of the system is 5×10^{-8}Torr and a metal Eu target is used as sputter source with the idea to oxidize Eu at the sample surface. Prior to deposition the target material is sputtered during several minutes to guarantee that superficial oxides are removed. The EuO films of 40-60nm are grown varying deposition temperature and rate, using different capping layers and substrates.The mass flux was measured using an oscillating quartz crystal, calibrated by perfilometry and/or XRR scans. The deposition parameters shown in the table were chosen inside the published conditions known from other deposition techniques as described in the introduction 1.1.1. The maximum deposition rate of the Eu is limited, because at higher deposition rates show the formation of an amorphous layer which then could not be properly characterized by XRD. The inter- and capping layers are also deposited by DC sputtering at a working distance of 15cm and an argon pressure of 1.0×10^{-2} Torr. For Mg deposition a power of 165W (rate 0.6Å/s) is used. For the Pd capping 75W (rate 0.9Å/s) are applied and for the capping with Al 125W (rate 0.25Å/s).

Table 5.1: Range of conditions used for EuO growth.

temperature	deposition rate	substrates	interlayer	capping layer
20°C - 600°C	0.10 - 0.18Å/s	YSZ, Si, SiN_x	Mg	Al, Pd

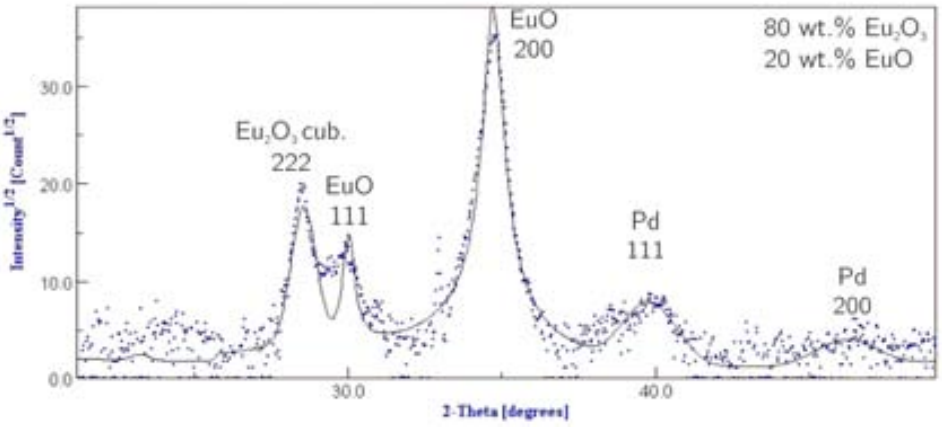

Figure 5.1: Quantitative MAUD analysis of a thin film consisting of EuO and Eu_2O_3.

In order to get a statistically significant result with few deposition the Taguchi method can be applied, which is generally used to improve the quality of a product depending on many parameters. Such attempts were made varying the parameters shown in table 5.1, though the bad reproducibility of the depositions led to few significant results. XRD measurements were used as coarse assessments for quality of the EuO thin film. In general a mixture of metal Eu and the oxides EuO, Eu_2O_3 is obtained. The Theta-2Theta scans were analyzed with MAUD [98], based on Rietveld's whole X-ray pattern fitting methodology, allowing the calculation of the mass percent of EuO contained in each sample. A typical fit is shown in figure 5.1. Note that even though the peak intensity of EuO is much higher the resulting mass EuO fraction, 20%, is much lower than the Eu_2O_3 fraction.

5.2 Effects of the Substrate

YSZ, Si and SiN_x substrates were used for the deposition having different advantages and drawbacks, which are presented in this section. The advantage of using **Si** is that its a non oxide material which is beneficial in growing a non stable oxide material such as EuO. Another reason for depositing on

Si is its widely use as substrate in semiconductor applications and the integration of EuO with Si is interesting for spintronic applications.
Before loading the Si substrates into the chamber, the native SiO_2 layer is removed by a quick dip in 10% hydrofluoric acid (HF). If the oxide is properly stripped off can be easily observed by putting a drop of water on the surface, which spreads on the hydrophilic oxide surface and bends on the bare hydrophobic Si surface. Dangling hydrogen bonds at the Si surface originating from the HF attack should protect the surface from oxidation during several minutes. Anyhow, in depositions at $300 - 400°C$ the X-ray pattern shows polycrystalline SiO_2, shown in fig. 5.2, which can lead to enhanced content of Eu_2O_3 at the interface. This is likely due to silicon oxide formation in the base pressure of the deposition chamber during the heating of the substrate before film deposition. For this reason a buffer layer of Mg or other substrates are used in later depositions at elevated temperatures.

YSZ is cleaned by Acetone, Ethanol and distilled water before being loaded into the chamber where it is kept at 400°C during 1h to guarantee a smooth surface. Our attempts to grow EuO on YSZ revealed that the substrate acts as an oxygen source, compared to samples deposited on SiN_x under the same conditions as shown in figure 5.2. Both substrates are deposited together at room temperature and capped with Pd. The YSZ substrate shows mainly Eu_2O_3 and EuO peaks, but the SiN_x substrate shows the metal Eu phase with fractions of EuO and Eu_2O_3. This makes the control of the oxygen in EuO difficult and irreproducible. The close lattice match and the fact that both EuO and YSZ have face-centered cubic structures, difficult also an unambiguous assignment of the EuO peaks in the XRD measurement.

The non-reactive surface of 340nm $\mathbf{SiN}_x$ capped substrates avoids the problems mentioned before and favors the formation of EuO at the interface. However, the fact that SiN_x has an amorphous surface SHOULD result in polycrystalline EuO.

5.3 Magnesium interlayers and capping

Interlayers of Magnesium are introduced with the purpose that magnesium competes with europium for the oxygen and prevents the formation of higher europium oxides at the interface. As a side effect it also prevents the formation of the intermetallic EuPd, which was observed in depositions at 400°C. Palladium was first chosen as capping layer, as from hydrogenation experiments performed earlier by Roger Domenech-Ferrer we know that hydrogen, but no oxygen can pass through such thin films. However the films capped with 20-30nm of Pd having a Mg interlayer showed visible circular changes

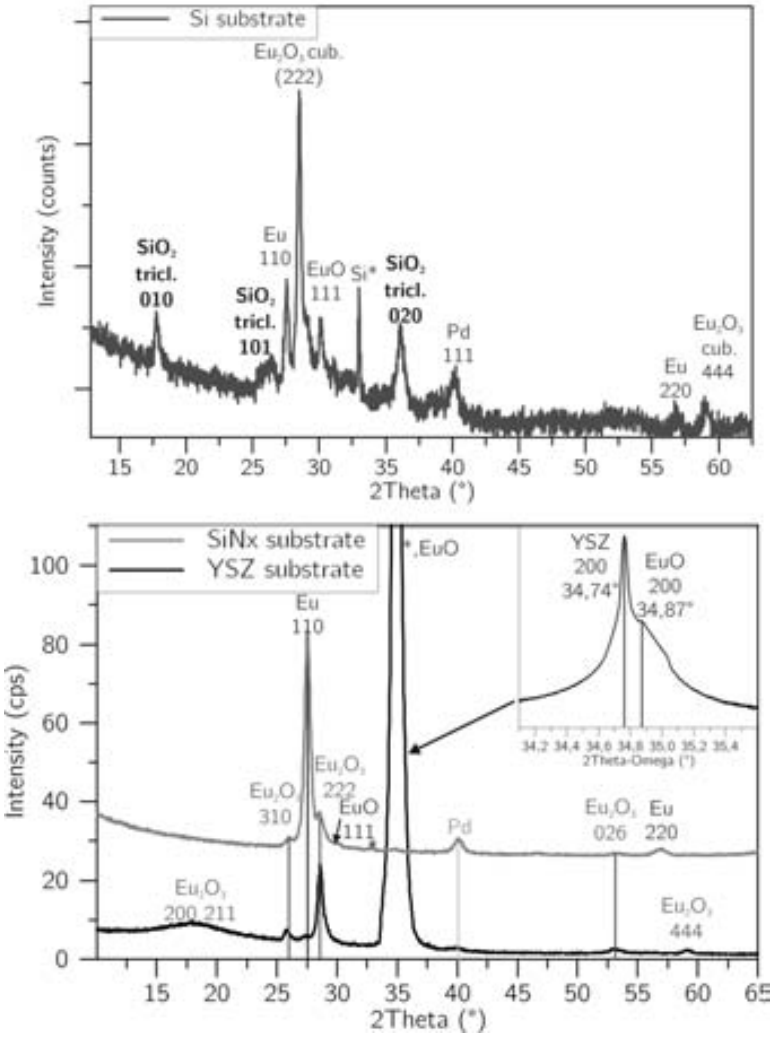

Figure 5.2: The figure on the top shows the formation of superficial SiO_2, after the Si slice was cleaned by HF, and afterwards was heated up to 400°C for EuO deposition. The figure on the bottom shows the Theta-2Theta scan of 40nm Europium deposited at room temperature on YSZ and SiN_x and immediately capped with 20nm Pd. The high resolution scan of the YSZ substrate peak shown in the inset allows us to distinguish the EuO peak (a=5.14Å) from the substrate(a=5.16Å).

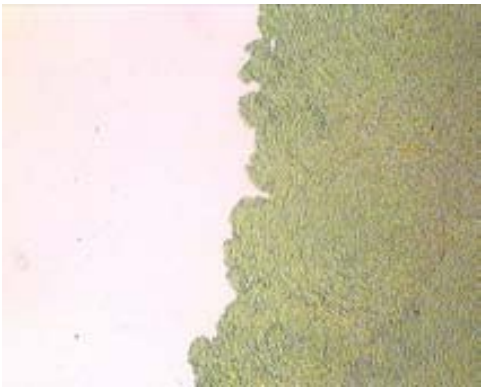

Figure 5.3: The image was taken with an optical microscope showing the visible degradation of the sample surface when capped with 10nm Mg and 20nm Pd layer.

at the sample surface after a few hours at air as shown in figure 5.3. This can be contributed to the formation of magnesiumoxide which causes a local volumetric change of 20%. These visible changes are accompanied by a decrease of the intensity of the EuO film peaks in Theta-2Theta scans towards an amorphous sample, as the cracks open ways for oxygen diffusion. Using these indicators, 20-30 nm thick Al capping layers were found to effectively protect the EuO films from degradation, as they form self-limiting Al_2O_3 at the surface.

5.4 Problems of EuO DC sputter deposition

The main problem with the sputter deposition is the relatively high base pressure and the high reactivity of the Europium inside the plasma. To enhance the knowledge about the composition of the base pressure (mainly H_2O and CO_2) a mass spectrometer was installed for measurements prior and after deposition. Mass spec scans show that europium reduces water as well as carbon dioxide inside the chamber (see fig. 5.4). The slight change in the hydrogen peak could indicate the formation of EuH_2 but hasn't been observed in XRD scans and is probably from the heating and subsequent cooling of the sputter gun. The composition of the chamber base pressure changes from one deposition to the next being an important factor when depositing without the introduction of O_2.

Most samples were deposited without introduction of additional oxygen, as the base pressure already has a high oxygen content being an important variable. The enthalpies of formation for H_2O and CO_2 are $\Delta E_f = -242$kJ/mol and $\Delta E_f = -394$kJ/mol [99], respectively. With a $\Delta E_f = -608$kJ/mol for

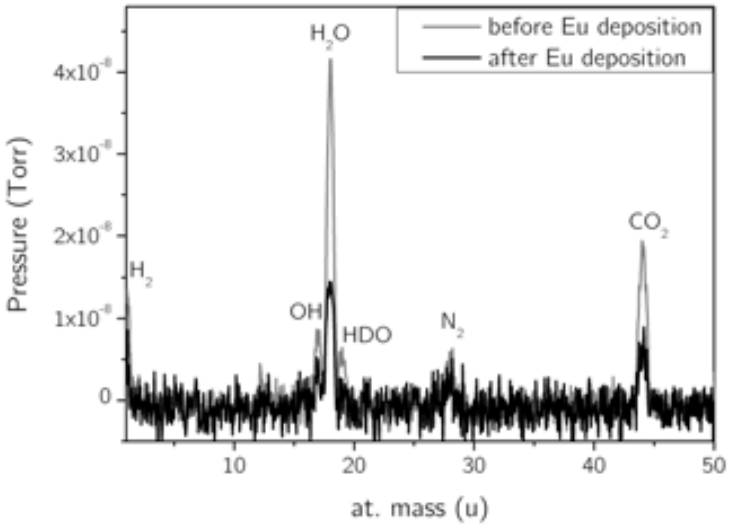

Figure 5.4: Mass spec scans before and after Eu sputter deposition.

EuO and $\Delta E_f = -1730$kJ/mol for Eu_2O_3 [100] evaporated and ionized europium can easily reduce the water and carbon dioxide present in the chamber to form oxides. As the base pressure of our system cannot be controlled easily, a low reproducibility in the depositions is the result.

Good quality samples could be deposited, as shown in fig. 5.5 on the top, though they couldn't be deposited repeatedly. The search of a condition window there small variations in the deposition parameters allow the growth of EuO could not be found. Although during the time of EuO depositions the sputtering system was barely used for depositing any other materials, the reproducibility of the samples is the main problem encountered with this technique. Samples that were deposited at room temperature with a base pressure of 4.5 to 5.0×10^{-8} Torr, where all other parameters were kept the same, did not show any reproducible formation of phases, see figure 5.5 on the botom. For this reason only samples deposited in the same run are compared here. Generally a mixture of Eu, EuO and Eu_2O_3 was obtained in the samples, indicating that the deposition conditions, namely the background oxygen pressure, are changing during the deposition. Also the getter effect of the interlayer and capping material affect at the interfaces.
Similar problems were observed by [16], who sputtered from an EuO target. They give an estimation of the extent to which the background contaminants like CO, CO_2 and H_2O influence the stoichiometry of a sputtered film (see fig 5.6). In comparison to the group [31, 35], that deposited EuO by co-sputtering Eu_2O_3 and Eu, we can say that by using the background

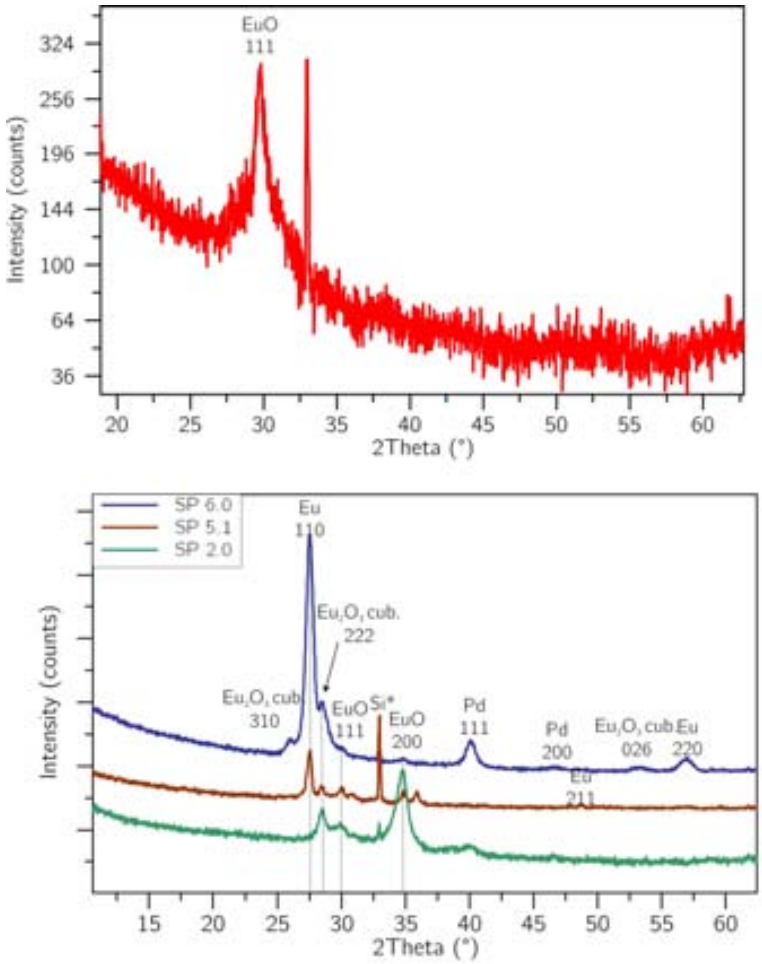

Figure 5.5: The figure on the top shows a pure EuO sample deposited at 100°C on a SiN_x substrate and then capped with 30nm Al. The figure on the bottom shows 3 under the same conditions, but separately, deposited samples indicating reproducibility problems.

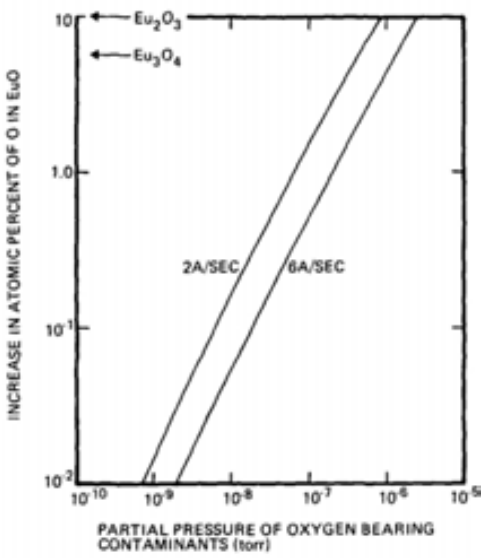

Figure 5.6: Assuming a sticking coefficient of one, an estimation of the % of oxygen that adds to the EuO surface is given as a function of the chamber base pressure bearing oxygen-contaminants. Taken from ref. [16]

oxygen pressure of the chamber for EuO deposition is not a good approach for EuO deposition, as the results get irreproducible. Some trials where a minimum amount of oxygen was introduced into the chamber resulted only in the formation of the pure Eu_2O_3 phase.

Chapter 6

EuO deposited by MBE

6.1 The role of introducing an MgO interlayer

In this chapter we present structural and magnetic characterization of EuO films deposited by MBE on lattice matching YSZ (001) substrates at low temperature, 573 K, with and without a MgO buffer layer, in order to demonstrate a less restrictive experimental condition window for high quality films when using such diffusion barrier layer. Surprisingly, the MgO buffered thin EuO films show a higher crystalline order, despite the big lattice mismatch, as well as better magnetic properties. One would expect epitaxial growth directly on YSZ as it has perfect lattice match with EuO.

6.1.1 Experimental

EuO layers (20 nm) were grown on (001) YSZ single crystal at 573K by evaporating Eu metal from a Knudsen cell at 0.21 Å/s in an oxygen atmosphere of 5×10^{-9} Torr. Prior to the evaporation, the substrate was heated to 653 K in high vacuum, $10^{-6}-10^{-7}$ Torr, for two hours to ensure a clean substrate surface. For some of the samples and prior to europium evaporation, 5 nm of MgO was deposited on the cleaned YSZ surfaces at room temperature using an electron-beam evaporator at 6×10^{-9} Torr with a deposition rate of 0.18 Å/s. After Eu evaporation and just before cooling down, a 5 nm cap layer of yttrium was evaporated by electron-beam at 3×10^{-9} Torr with a deposition rate of 0.15 Å/s. To avoid further oxidation when exposed to air, a thicker supplementary aluminum barrier, 80 nm, was sputtered on top of the structure once the sample had cooled down to room temperature. X-ray diffraction (XRD) analysis was performed in a four-angle diffractometer (X'Pert, Panalytical) with CuK_α radiation. $2\Theta/\omega$ spectra were acquired with a 2 degree omega offset to avoid as much as possible overlapping with single crystalline substrate reflections. High-resolution 2Ω scans in the vicinity of the 200 YSZ substrate reflection were performed by using monochromatic $CuK_{\alpha1}$ incident beam generated with a 4 crystal Ge

(220) asymmetric monochromator. To avoid the substrate we performed, using the same equipment, in-plane diffraction scans where lattice planes perpendicular to the surface can be measured. Phi scans (rotation angle in the film plane) with a 2Θ value fixed to the one corresponding to EuO 200 and YSZ 200 reflections were acquired using such in-plane diffraction geometry with both incident and exit grazing angles (ϕ) of about 0.5°.
X-ray Photoelectron Spectroscopy (XPS) of the multilayers was performed ex-situ using a PHI ESCA-5500 spectrometer equipped with a monochromatic Al K_α source. Compositional depth profiles of the heterostructures were acquired after sample bombardment with an ionized argon beam to enable in-depth characterization of the oxidation throughout the various layers and at the interfaces. Magnetic characterization was carried out using a SQUID magnetometer (Quantum Design MPMS XL-7T) with the field applied parallel to the sample surface. The hysteresis loop M vs. H was measured at 5 K sweeping the field up to ±3000 Oe.

6.1.2 Results and discussion

6.1.2.1 Structural characterization

Figure 6.1 shows the XRD pattern of 20 nm thick EuO films prepared on bare and MgO coated YSZ substrates. For films deposited directly onto YSZ (bottom scan), the 111, 200, 222 and 400 reflections are clearly distinguishable and perfectly match those of the polycrystalline EuO face-centered-cubic crystal structure. On the contrary, for layers deposited on MgO-coated YSZ (top scan), no reflections other than those identified with YSZ substrate are observed. Reflections associated with higher oxidation states of europium, Eu_2O_3 or Eu_3O_4, are neither identified. As EuO (001) and YSZ (001) have a perfect lattice match ($a_{EuO} = a_{YSZ} = 5.144$ Å), epitaxial growth of EuO on top of YSZ was envisaged instead of the observed disordered growth. On the contrary, as MgO has a smaller lattice parameter, a_{MgO}=4.212 Å, lattice mismatches of YSZ(001)/MgO(001) in either cube-on-cube arrangement (-22%) or 45°-in-plane rotation (-13%) are quite large. Consequently, ordered growth of EuO on MgO buffered-YSZ lattices, which may have made the contribution from the EuO film and YSZ substrate undistinguishable, was not expected. Therefore, we performed high resolution XRD scans in the out of plane direction through the 002 peak, as shown in the inset of figure 6.1, to assess any possible epitaxial growth responsible for the reflections overlapping. Only a single peak is observed. Neither a separate film peak nor Kiessig fringes associated to the film thickness are observed, ruling out the coherent epitaxial growth of EuO on MgO-YSZ. However, these observations do not preclude the existence of a highly-oriented out-of-plane film texture. In order to analyze the film texture, we perform ϕ scans on different reflections. Standard ϕ scans

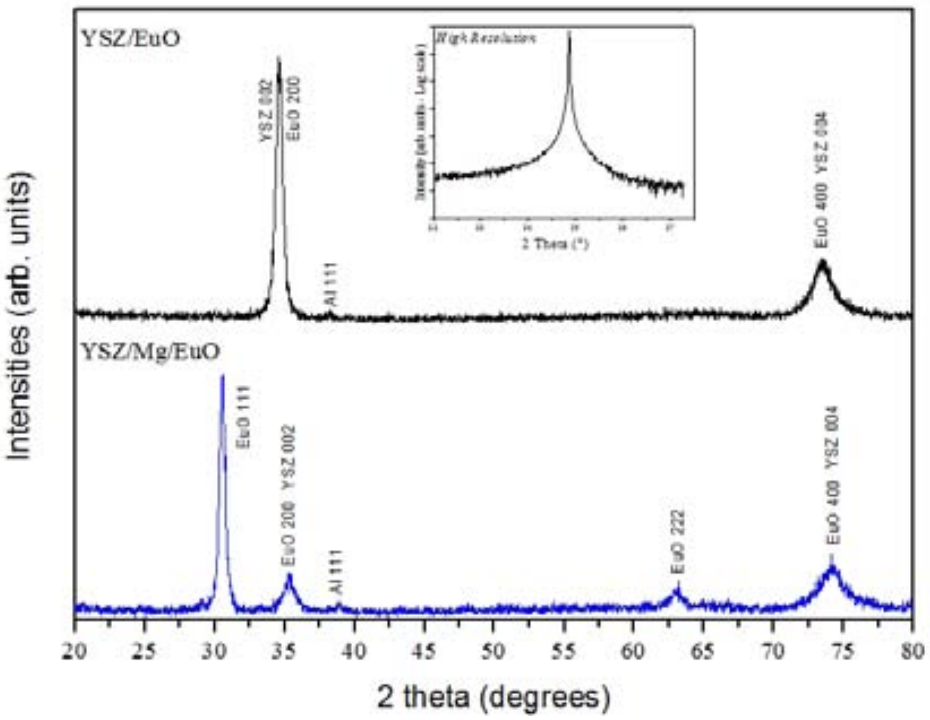

Figure 6.1: XRD patterns of EuO/YSZ and EuO/Mg/YSZ heterostructure. Inset shows High resolution XRD along 002 reflection.

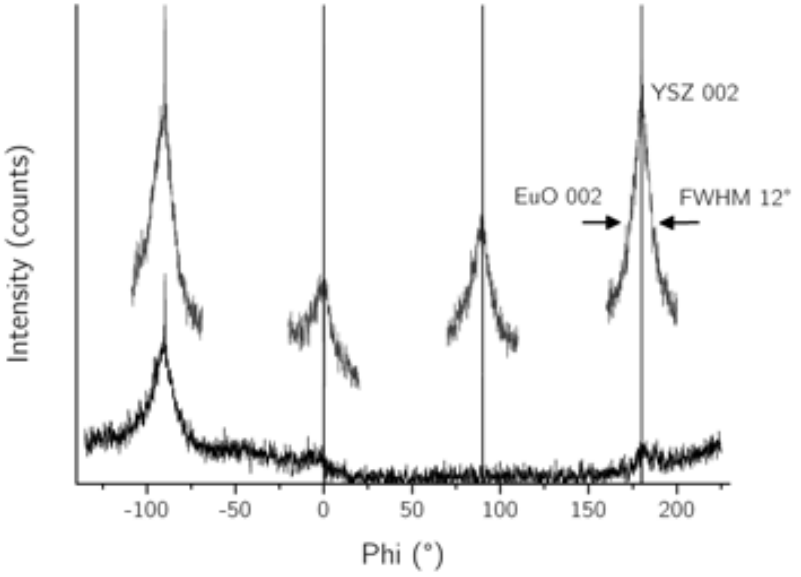

Figure 6.2: Individual in-plane ϕ-scans performed after optimization in the different phi ranges in grey the full range phi (black) scan could not be aligned over the whole scan range. Four sharp peaks mark the YSZ substrate.

of asymmetric reflections do not reveal any substantial contribution from the EuO film. Therefore, we carry out ϕ scans of the 200 YSZ reflections with the in-plane diffraction geometry (0.5° incidence angle) to determine the in-plane texture of the film. In this geometry the X-ray penetration in the sample is reduced so film contribution is substantially enhanced (the presence of the thick Al cap layer did not seem to affect the measurement due to its low x-ray absorbance). In-plane 360°ϕ-scan, performed with 2Θ fixed to YSZ and EuO 002 reflections, shows four narrow peaks associated with the fourfold symmetry of the substrate. Wider and less intense peaks are also observed at the same ϕ angles and thus assigned to the 002 EuO film reflections. The weak intensity of the peaks, especially above $\phi = 90°$, is assigned to the difficulty in maintaining perfect planarity of the sample during 360 degrees rotation, giving rise to a signal intensity lost. To get rid of this technical limitation, we perform local scans of 40 degrees range (-20, +20) around the four maximum ϕ angles observed for YSZ but using individually optimized parameters for each position (figure 6.2). Local phi-scan shows four wide peaks (FWHM=12°), aligned with the sharp reflections corresponding to the substrate (figure 6.2) demonstrating the preferential

in-plane orientation of the EuO crystals. We have to mention that complementary partial scans performed in between those maxima do not reveal the presence of any other maxima which could indicate a different in-plane alignment. Out-of-plane and in-plane X-ray diffraction results confirm the textured growth of the EuO lattice onto MgO-coated YSZ substrates.

Sutarto el al. [101] already pointed out the difficulty of growing stoichiometric EuO films on YSZ, because of its oxygen donor ability, preparing epitaxial EuO films on YSZ using a lower oxygen partial pressure than that used for films grown on MgO substrates. Intermediate MgO may thus act in our samples as a barrier suppressing any oxygen interdifusion coming from the substrate and allowing conditions for highly oriented growth to be reached only onto MgO. Such, diffusion barrier effect was also exploited by Swartz et al. [25] to prepare epitaxial EuO films on GaAs. Here, similarly to Sutarto et al. [101], highly in-plane and out-of-plane texture is preserved throughout the EuO/MgO/YSZ heterostructure despite the large lattice mismatches. Unfortunately, probably due to its low thickness (5nm), XRD analysis did not allowed us to confirm the formation of the highly textured MgO, mandatory for such crystallographic ordered growth. Ex-situ XPS in-depth analysis of the complete heterostructure is also performed to investigate chemical bonding states of the constituent atoms, mainly Mg and Eu metals and oxygen. To perform the XPS depth profiles, we acquire general scans, from 0 to 1100 eV, after each minute of etching using an argon gun. As the aluminum cap layer is rather thick (80 nm), the first scan is performed after 4 minutes of etching. Figure 6.3 shows some scans selected as representative of a particular depth of the Al/Y/EuO/MgO/YSZ heterostructure. From 4 to 9 minutes of etching, we observe peaks corresponding to aluminum (Al2p and Al2s) and yttrium (Y3p and Y3d) cap layers and already to europium (Eu 4d). While aluminum peaks decreases, Eu4d peak clearly increases as increasing depth. The O1s oxygen peak also increases considerably from the aluminum layer level (after 4 minutes etching) to the Al/Y/EuO interface, reached after 9 minutes attack. From that depth on, we perform a more precise analysis acquiring shorter spectra, in between selected energy ranges, after every 20 seconds of etching. After a total attack of 11 minutes, the Zr3p and Zr3d peaks corresponding to the YSZ substrate appear as well as a very weak signal tentatively assigned to Mg2p, confirming that the bottom MgO/YSZ interface is reached.

When in the vacuum of 10^{-8} Torr the monolayer formation time is of several minutes corresponding to 1.1. This was also observed in our measurements on the Eu and O_2 peak. In figure 6.4 the $Eu5d_{5/2}$ peak one can observe that the initial asymmetric contribution of the shake-up peak of divalent europium ions starts forming the symmetric peak characteristic for trivalent europium ions. In the $O_2$1s peak an contribution due to the formation of Eu_2O_3 can be found. After 20min a EuO exposed surface in a vacuum of 7×10^{-8} already show an increased amount of higher oxides.

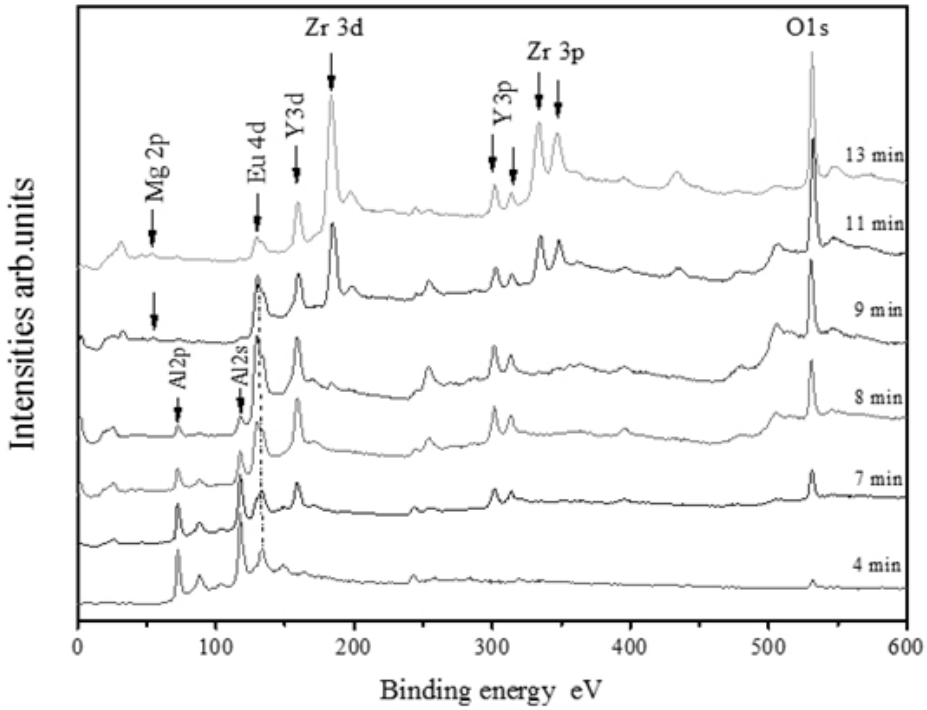

Figure 6.3: General XPS spectra of the heterostructure after several etching times.

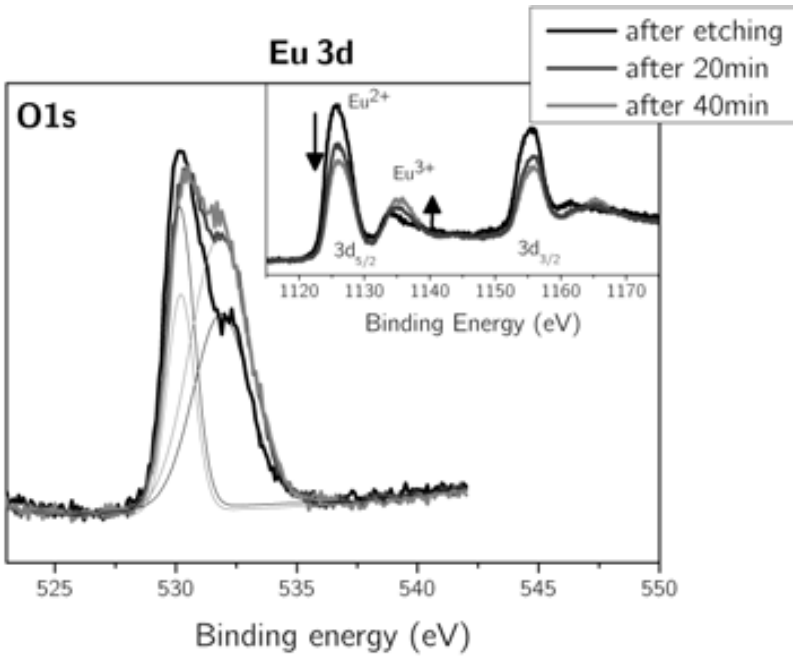

Figure 6.4: After several minutes in high vacuum $\sim 10^{-8}$Torr the formation of higher oxides can be observed in the Eu5d as well as in the $O_2$1s peak.

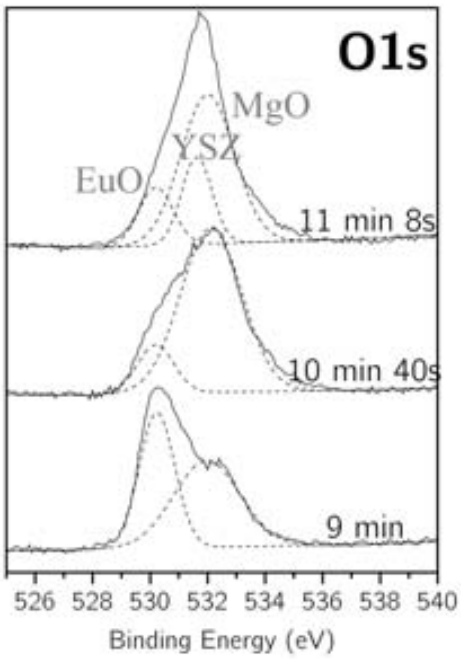

Figure 6.5: Evolution and deconvolution of the oxygen peak O1s with depth, i.e. etching time. The contributions of EuO, MgO and the YSZ substrate to the peak are assigned.

Figure 1.1 shows the Eu3d core-level spectra acquired after a $9'$ etch. The spectra performed consist of two main groups, the 3d5/2 (at 1125,7eV) and 3d3/2 (at 1155,5 eV) structures which are clearly separated due to a large spin-orbit splitting of 29,8 eV in excellent agreement with previous work [33]. These main peaks, and the corresponding satellite doublets, are assigned unambiguously to the divalent Eu^{2+} multiplet, confirming that EuO is grown free of Eu_2O_3 or Eu_3O_4. Within the entire EuO thickness no changes related to Eu^{3+} coming from higher oxides are observed, confirming that pure and stoichiometric EuO was grown on MgO diffusion barrier.

Figure 6.5 shows the O1s core-level spectra acquired after some selected etching time also in the $9'$ to $11'20''$ range. From $9'$ to $10'40''$, i.e. from top EuO/MgO to bottom EuO/MgO interface, we clearly identify two peak contributions, fitted using single Gaussian peak, with maxima at 530,2 and 531,8 eV, which can be both correlated with EuO or MgO oxides. The exact EuO and MgO contributions to the O1s peak are not straightforward, as both peaks are expected to appear at similar binding energies. Nev-

ertheless, as observed when comparing spectra at different heterostructure depth (figure 6.5), the intensity of the high energy shoulder of the O1s peak increases with increasing etching time, i.e. as approaching the MgO/YSZ interface. This deconvoluted peak can thus be assigned to the MgO contribution to the O1s spectra while the lower energy shoulder is assigned to the EuO contribution. When increasing depth (i.e. etching time) the O1s peak cannot be correctly fitted with two contributions and a third peak has to be added, corresponding to the zirconia contribution to the oxygen signal and confirming that the substrate is reached.

6.1.2.2 Magnetic characterization

Magnetic properties of the films are studied using a superconducting quantum interference device (SQUID) magnetometer. M vs. H at 5 K is shown in figure 6.6 for the 20 nm thick EuO films deposited on YSZ and on MgO-buffered YSZ. The temperature dependence of M for these two films stacks is shown in the inset. Strong ferromagnetic behavior with a saturation magnetic moment of 6 μ_B and 7 μ_B, for YSZ and MgO-YSZ films, respectively, are measured approaching the bulk value of 7 μ_B per Eu ion [102]. The observed T_C, 71 ± 1 K and 69 ± 1 K [1], for YSZ and MgO-YSZ films, respectively, are also close to bulk EuO, 69 K [102]. The coercive fields of the films are 165 ± 10 Oe and 110 ± 10 Oe, for YSZ and MgO-YSZ films, respectively.

EuO layer deposited on bare YSZ shows slightly lower saturation magnetic moment and larger coercive field, compared with films deposited on MgO-buffered YSZ. These differences probably rely on film microstructure, as EuO/YSZ films are polycrystalline with mixed orientations while EuO/MgO-YSZ showed high 3D crystallites orientation. The structural ordering does not seem to affect the T_C, as both films exhibit similar values close to the single crystal bulk value. The broader hysteresis loop, with a coercivity of 165 ± 10 Oe, in EuO/YSZ films compared to MgO buffered ones, is consistent with the presence of larger and more disoriented grain boundaries in films deposited directly on YSZ [103].

6.1.3 Conclusions

High quality pure stoichiometric EuO thin films have successfully been grown on YSZ as well as on MgO-buffered YSZ, using the MBE technique. In spite of the lattice mismatch EuO films grown on MgO-YSZ substrates shows a high degree of 3D texture with in- and out-of-plane alignment with the underlying YSZ crystal, as demonstrated by XRD. In-depth XPS analysis confirms the exact oxygen stoichiometry of EuO deposited on the MgO

[1] The curves are fitted with the 2D Ising model: $M(T) \sim (T_C - T)^{\beta}$ with $\beta = 1/8$

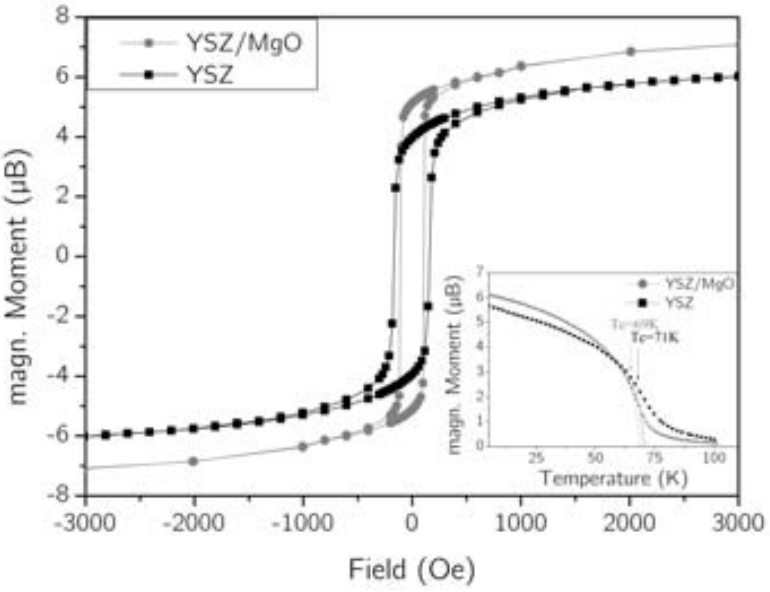

Figure 6.6: Magnetization M vs. H of the EuO films grown on YSZ and MgO/YSZ substrates. The inset shows the temperature dependent magnetization.

barrier. SQUID measurements confirms the high quality of the EuO layers, with T_C and M_S values close to single crystal ones. The difference in crystallites arrangement appears to be the cause of the enhanced saturation magnetization observed for the EuO film grown on buffered substrates ($7\mu_B$) compared to EuO films directly grown on YSZ ($6\mu_B$). As expected, growing onto MgO interdifusion layer, although not allowing epitaxial growth, generates a 3D texture EuO film with excellent magnetic properties. The MgO barrier hinders the O_2 coming from the YSZ substrate allowing EuO to grow highly oriented. As MgO is known to epitaxially grow on silicon, next step will be to prepare highly textured EuO films on extremely thin MgO-buffered silicon substrates. Such architecture, mimicking that formerly proposed by Schlom et al. [2, 3] using extremely thin SrO epitaxial buffer layer on silicon, could be used to inject spin polarized electrons into silicon for the use in spintronics applications.

6.2 Effect of Se doping

In this chapter we present Se-doped and undoped EuO thin films which are deposited at room temperature. The relatively low Curie temperature of 69 K renders difficult its application in real devices. Several strategies including electron doping or induced strain can be used to increase the Curie temperature. Here we present the remarkable behavior of Se-doped EuO films and compare the structural and magnetic properties of selenium doped and undoped EuO thin films deposited by molecular beam epitaxy under the same conditions. The first evidence that highly orientated thin films can be grown at room temperature is shown. Magnetic measurements show that the addition of only 0.3% at. Se raises the Curie temperature up to 130 K offering a new perspective towards future applications.

6.2.1 Experimental

10nm thin films of EuO are deposited on HF etched Si at room temperature in a MBE system with a base pressure of 8×10^{-10}Torr. The partial oxygen pressure is 4×10^{-8} Torr and the growth rate is 0.14Å/s. Immediately after EuO deposition the film was capped with 5nm of Al by e-beam within the same chamber. A thick Al layer is then deposited after transferring the sample in the load lock chamber. Due to previous depositions of BiSe a certain amount of Se contamination is expected in the MBE chamber. Though the base pressure of the system didn't show any change.

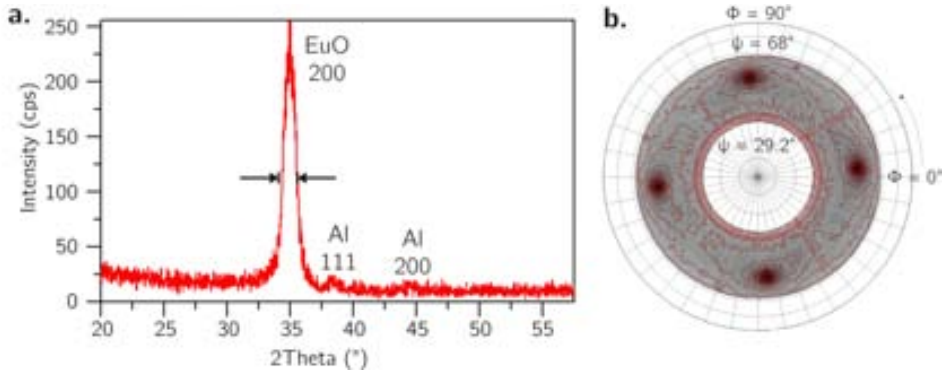

Figure 6.7: Figure a. shows the Theta-2Theta scan of the doped EuO thin film. Figure b. shows the Pole figure of the same film, taken at $2\Theta = 30.1°$ corresponding to the 111 peak.

6.2.2 Results and Discussion

6.2.2.1 Crystalline structure

Surprisingly, the films grown at room temperature on Si (100) show a preferential growth in the 200 direction (see Theta-2Theta scan fig 6.7a.). We observe broadening of the 200 peak in the Theta - 2Theta scan. From the Debye-Scherrer [104] equation, the minimum sizes of the ordered crystalline domains L can be approximated from the XRD peak half-width by assuming that there is no strain:

$$L = \frac{K\lambda}{\Delta \cos\Theta} \tag{6.2.1}$$

where K is the shape factor, λ is the x-ray wavelength, $\Delta = \Delta_{meas} - \Delta_{std}$ is the difference in FWHM width between a standard and the measured EuO sample in radians, and Θ is the Bragg angle. The typical value of K is 0,9, taken for spheres and cubes, though it varies with the actual shape of the crystallite. From the 1.15° FWHM of the EuO peak the size of the average EuO grains can be estimated to be higher than 8.5 ± 1.3[2]nm. This opens the possibility that our film has grown highly orientated, even epitaxial. The pole figure taken at 2 Theta equal to 30.1Åcorresponding to the 111 peak confirms that only highly orientated EuO is present in our sample. In the GADDS measurement the Si substrate contribution is separated from the contribution of EuO, by carefully limiting 2Theta on the area detector to $29.2° - 40°$ to avoid the Si contribution at $2\Theta = 28.4°$. Apart from the fourfold symmetry of the cubic EuO structure no other crystalline orientations are observed. The EuO 200 axis is oriented along the Si 400 axis, and the EuO 111 axis along the Si 111 axis. This results in a lattice

[2]error comes from the $\sim 15\%$ uncertainity of the Debye-Scherrer formula

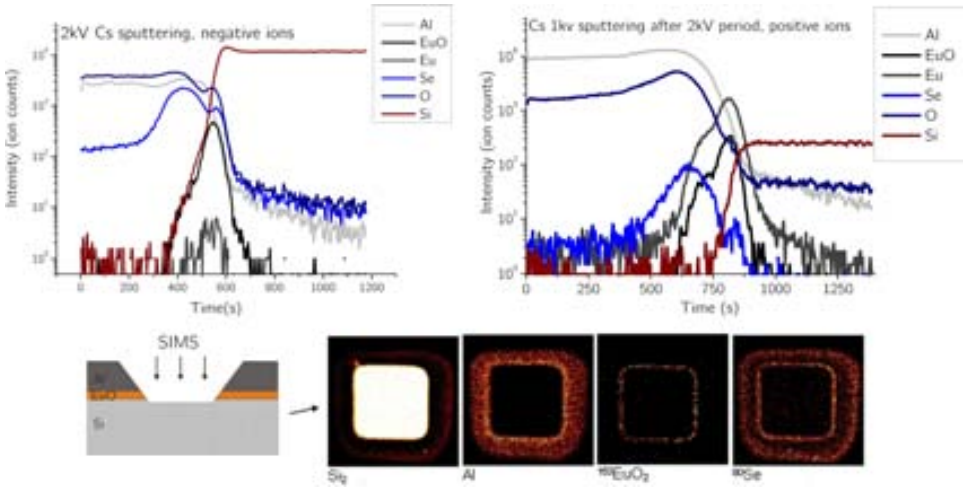

Figure 6.8: The SIMS depth profile (as a function of sputter time) of the materials present in the film is measured by positive and negative ions. At the bottom the images of negative ions of the attacked area show the location of the different zones inside the film.

mismatch of 5.3% at the Si-EuO interface.
The SQUID measurements, shown later in fig. 6.11b. in samples doped with Se coming from the background pressure in the MBE system show 2 Curie temperatures (T_{C1}=67K, T_{C2}=130K) in comparison to the stoichiometric EuO film. In order to know where the Se is located in our sample SIMS measurements were performed.

6.2.2.2 Composition analysis

The SIMS measurement (fig. 6.8) gives information about the impurities present in our samples. The sample is sputtered with a focused Cs beam and the secondary ions ejected from the sample are analyzed by a mass spectrometer. Cs bombardment increases the yield of negative ions (Se, Si) and has reduced ionization efficiency for Eu and Si, as can be seen when comparing the measurement of negative and positive ions. In order to extract the relative concentrations of EuO and Se, reference samples with known Se concentrations would have to be produced. Also, implementation of surface atoms into the sample leads to smearing of the result. Anyhow, it can be clearly seen that with increasing sputter time the Se concentration enhances while still in the aluminum region, corresponding to the presumption that with the capping with Al performed inside the MBE chamber also Se was introduced. Further attack of the sample reveals a notable amount of Se also in our EuO film, giving rise to the assumption that the enhanced magnetic

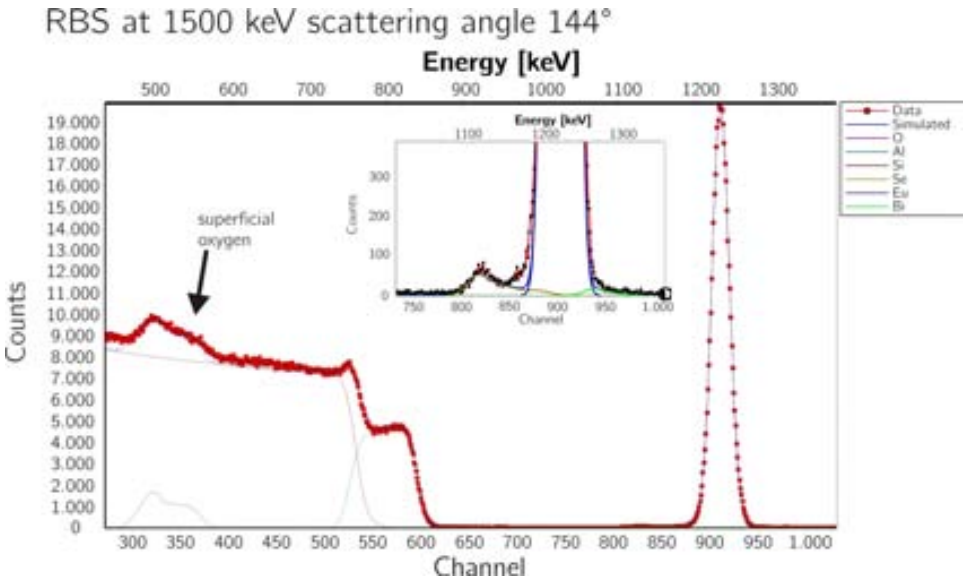

Figure 6.9: The entire spectrum taken at 1500keV is fitted with SIMNRA, where the contributions of each element can be distinguished. The energy scale is calibrated with a known reference TiTa multilayer sample on Si. The inset shows the area relevant for the doping contribution.

properties are due to Se doping of our EuO thin films. To get information about the real Se concentration in our sample additional Rutherford Backscattering Spectroscopy (RBS) measurements are performed.
These measurements reveal the depth and concentration of the Se buried in the film. The RBS study has been performed at CMAM with the 5 MV tandem accelerator using a He beam at two different energies, 1500 keV and 3035 keV. The lower energy beam (fig. 6.9) will give a better depth resolution, and the higher energy beam (fig. 6.10) will give a better mass resolution besides being centered in a resonance in the scattering cross section for the oxygen, increasing the sensitivity to detect this element near the surface of the sample. The fit was performed using the computer code SIMNRA [64]. The spectrum shows clearly that also the covering Al layer contains oxygen. All the fits agree that the amount of oxygen increases towards the interface with the EuO layer. The thickness of each layer is measured in units of 10^{15}atoms/cm^2. One of such units is roughly equivalent to a monolayer (something between 0.2 or 0.25 nm, depending on the material). The calculated thickness of the EuO film is 10.0 ± 0.5nm in accordance with the nominal thickness measured with the crystal monitor.

Layer	Thickness (10^{15}at/cm^2)	Si (%)	O[1] (%)	Al (%)	Se (%)	Eu (%)	Bi (%)
1	520	0	36.97	63	0.03	0	0
2	370	0	41.9375	58	0.06	0	0.0025
3	60	0	49.735	50	**0.25**	0	**0.015**
4	**65**	0	49.79	0	**0.2**	50	**0.01**
substrate		100					

[1] The digits given for the composition of oxygen are not significant besides the first decimal digit. The RBS simulation program needs them to normalize the overall composition to 100%.

RBS results confirm the presence of Se in the sample estimating that it is present in the Al + O film as well as in the EuO film. The RBS spectra taken at 3035 keV, which is the resonance oxygen, depict more clearly the Se signal. According to this spectrum the concentration of Se would be higher (0.3 at %) in the EuO film. The uncertainty of overall amount of Al and Eu atoms in the sample as determined with RBS is estimated to be of 5%. This value is of 10% for Se and the heavier Bi. All spectra could be fitted within these limits. As the first Al layers near the EuO interface were deposited in the Se contaminated chamber, also a considerable amount of Se can also be found in the Al layer.

Layer	Thickness (10^{15}at/cm^2)	Si (%)	O[1] (%)	Al (%)	Se (%)	Eu (%)	Bi (%)
1	520	0	35.97	65	0.03	0	0
2	320	0	44.9375	55	0.06	0	0.0025
3	60	0	49.785	50	**0.2**	0	**0.015**
4	62	0	49.69	0	**0.3**	50	**0.01**
substrate		100					

[1] The digits given for the composition of oxygen are not significant besides the first decimal digit.

6.2.2.3 Magnetic properties

The magnetization measurements (fig 6.11 a.) show, that the Se doped as well as the undoped films have a magnetic moment of $6.9\mu_B$ per Eu atom in good agreement with the bulk value of $7\mu_B$ per Eu atom. The H(T) curve in fig. 6.11b. shows that the Se doped film has 2 Curie temperatures in comparison to undoped EuO films. The Curie temperatures the of the doped film 67K and 130K using the derivative shown in the inset. In the paramagnetic region EuO follows the Curie-Weiss law, $\chi^{-1} = (T - \Theta)/C$, where χ is the susceptibility, Θ the paramagnetic Curie temperature, and $C = n\mu_{eff}^2/(3k_B)$ with n being the number of magnetic particles per cm^3,

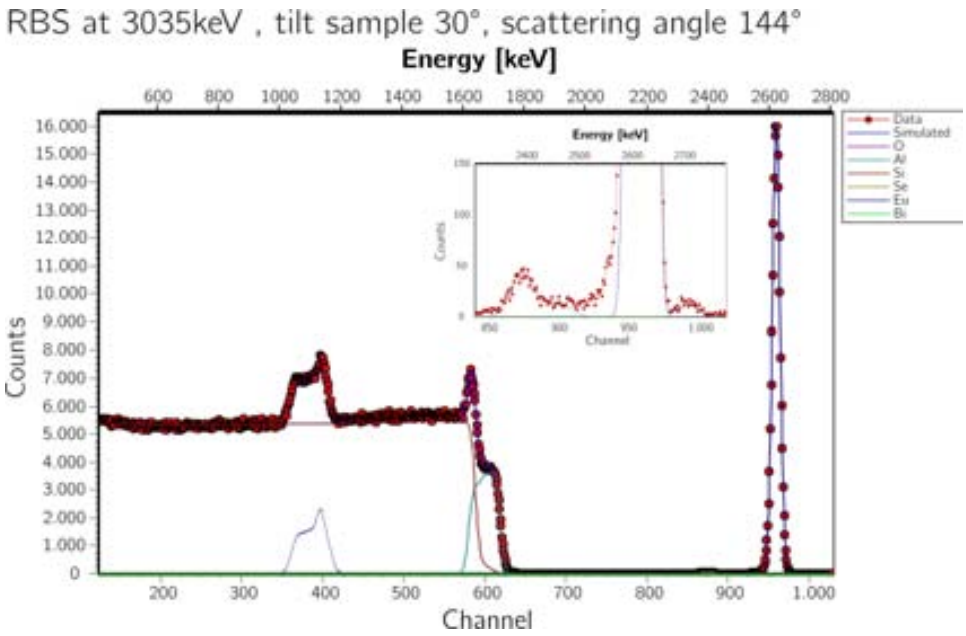

Figure 6.10: The entire spectrum taken at the oxygen resonance at 3035keV. The contributions of each element can be distinguished. The inset shows the area relevant for the doping contribution.

and μ_{eff} the effective paramagnetic moment. The measurement of the susceptibility (fig. 6.11c.) gives a paramagnetic moment of $7.9 \pm 0.4\mu_B$ per Eu atom, as expected for $\mu_{eff} = \mu_B g\sqrt{J(J+1)}$, and a paramagnetic Curie temperature of $120 \pm 5K$[3]. The small jump at 150K in the susceptibility curve comes from the transition through zero, which is afterwards is corrected for the substrate contribution and has no physical meaning. The two onsets of the magnetization (two peaks of the first-derivative) indicate that two phases with different T_C values coexist in the Se-doped EuO: one is the same as that of the stoichiometric EuO and the other an additional T_C at higher temperatures due to the Se doping in the film. [50] Other groups have observed also two contributions in the M(T) curves in Eu-rich EuO [31], Gd, Ce, and La doped EuO [24, 48–50], due to possible clustering of the dopants in the film [50], or due to the formation of local impurity moments which are superexchange coupled with the 4f moments [105]. According to Mauger [44] a critical concentration above 1% is needed to allow for free carriers and enhance the T_C accordingly, though some observed the effect of doping in concentrations as low as 0.2 % [24]. The magnetization of EuO comes from the 4f electronic configuration of Eu^{2+} ions. Extra charges due to doping or oxygen vacancies can occupy the 5d levels of the conduction band enhancing the magnetic exchange between 4f and 5d electrons [49]. As the ionic radius of Se^{4+} is 0.5Å, it is likely to occupy the Eu lattice sites, (ionic radius of Eu^{2+} is 1.17Å and of O^{2-} is 1.35Å) [106]. On on hand Se^{4+} has a smaller radius than Eu^{2+} and doping EuO with Se^{4+} will therefore lead to an increase of ferromagnetic interactions. On the other hand Selenium can share up to 4 electrons per atom between nearest neighbors. Two electrons will be shared with the neighbor oxygen atom, leaving 2 extra electrons that can be excited into the conduction band. Doping with extra electrons is well known to increase the T_C of EuO above 70 K, the value for pure EuO. It is, however, notorious the much larger increase of T_C with respect to previous dopants found in the literature (Gd^{3+} or La^{3+}). The smaller ionic radius of Se could also introduce chemical strain in the EuO lattice leading to higher T_C as shown by Ingle and Elfimov [56]. However, within our experimental uncertainty we have not observed such contraction in the position of the XRD peaks, which may be due the very small amount of dopants in the sample. At present, the mechanism responsible for the large T_C increase with a low Se doping remains unclear and more experiments are needed to verify its occurrence.

6.2.3 Conclusions

Thin EuO films are deposited directly on a silicon substrate exhibiting highly orientated growth at room temperature despite the lattice mismatch of 5.3%

[3]The error comes from the correction with the reference sample, which was deposited independently.

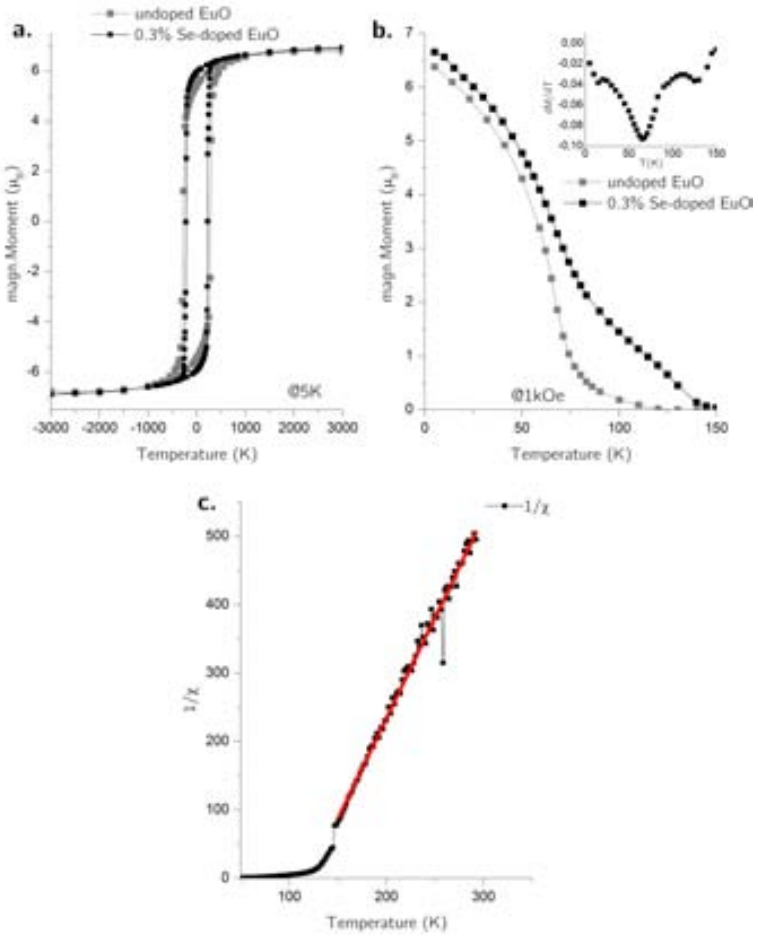

Figure 6.11: Figure a. shows the M(H) with a coercivity of 220 Oe and a saturation magnetization of 5.95 μ_B for the Se doped sample. The M vs T curve for a EuO standard and the doped curve are shown in fig. b., where the doped sample exhibits 3 separate Curie temperatures which also can be good distinguished in the derivative shown in the inset. Figure c. shows the inverse susceptibility curve already corrected for the substrate. The red line indicates the fit of the Curie Weiss law.

at the Si-EuO interface. An enhancement of the magnetic Curie temperature to 130K is observed in the sample doped with selenium. The dopant concentration in the sample is determined by Rutherford Backscattering Spectroscopy to be $0.30 \pm 0.015\%$. This is the lowest doping level observed for enhancing T_C by $\sim$ 60K, being much lower than the doping levels needed to reach saturation of the Curie Temperature temperature at 125 K with Gd or La doping ($\sim 4\%$) [24, 47]. This approach appears promising to further increase T_C in EuO and enable this material to be used in future spintronic applications. We propose an Eu-O-Se superexchange mechanism, where the Se atom donates 4 electrons to the conduction band forming the Se^{4+} ion. Two of the donated electrons are shared with the neighboring oxygen atoms, and 2 electrons per Se atom go in the Eu 5d conduction band.

Chapter 7

Nanocalorimetric measurements on PLD deposited thin EuO films

7.1 Motivation

The first calorimetric measurements on bulk EuO have been performed already in 1966 by Teaney [60]. More recent measurements also allow extracting the dependence of the specific heat as a function of applied field [61]. Due to the difficulties in the deposition of EuO, which readily forms non-magnetic higher oxides (Eu_2O_3, Eu_3O_4) when exposed to air, thin film growth is more delicate. Due to its simple cubic NaCl-type structure and being an ideal Heisenberg ferromagnet, EuO can be used as a model system for spin injection as well as calorimetry.

7.2 Experimental details

EuO is deposited by PLD at the University of Twente in a stack of MgO(2nm)-EuO(x nm)-MgO(2nm)-AlO_x(20nm) onto the SiN_x membrane of the nanocalorimeter chips. It is important to note that each sample is deposited separately and only the 2 reference calorimeters are deposited together. For deposition the sample is heated up to 300°C with a base pressure of 3×10^{-8} Torr at this temperature. A fluence of 2.5 J/cm^2 is used. The MgO buffer layer is deposited as a diffusion barrier to prevent the formation of higher europium oxides at the interface. It is deposited from a metal Mg substrate (deposition from the MgO substrate had too low efficiency) in O_2 atmosphere of 5.2×10^{-6}Torr at 4Hz for 71s. The greenish color of the plasma indicates the formation of the oxide. Afterwards the O2 valve is closed and the Eu target is preablated. The EuO is deposited from a metal target with nominal thicknesses of 19, 12, 7 and 3nm in O_2 atmosphere of 2.5×10^{-6}Torr following the

recipe from [28]. The ablation frequency is 20Hz. The O_2 valve is closed and Mg preablated. An additional 2nm of MgO are deposited as the deposition of Al at 300°C has lead to the formation of Al-Eu intermetallics observed in sputtered films. The heater is switched off and we wait several hours (keeping the sample in a vacuum of 10^{-8} Torr) for cooling down below 100°C before depositing the final 20nm AlO_x (5Hz, $P_{Ar} = 4 \times 10^{-3}$Torr). The quality of the EuO thin films is checked by in-situ core level XPS measurements as well as ex-situ magnetic measurements. The XPS measurements are performed inside the deposition chamber system without breaking the vacuum. This quasi in-situ technique allows XPS measurements on clean surfaces, giving unique information about the chemical state of the different elements. The photon energy of the Omicron monochromatic Al source is 1483 eV and the energy resolution of the system is 0.1 eV at 1 keV. The magnetic measurements are performed by SQUID (Quantum Design MPMS XL-7T) as well as PPMS (Quantum Design PPMS with VSM option). The thermodynamic properties of the samples are characterized from 30K to 120K by fast scanning on home-made calorimetric cells in a closed cycle cryostat at MatGas.

7.3 Electronic and Magnetic properties of the PLD deposited EuO films

To find the optimum partial oxygen pressure for the deposition XPS scans were performed without breaking the vacuum as shown in figure 7.1. The red curve shows a high amount of Eu_2O_3 and was deposited with a partial oxygen pressure of 5.0×10^{-6}Torr, where at a binding energy of 8 eV the $4f^6 \rightarrow 4f^5$ state appears in the valence band. The blue curve shows typical stoichiometric EuO deposited with 2.8×10^{-6}Torr oxygen in the chamber.The valence band spectrum shows the Eu $4f^7 \rightarrow 4f^6$ electron removal state, the oxygen 2p band and the $4^6 \rightarrow 4f^5$ state. On the nanocalorimeters a slightly underoxidized $EuO_{1-\delta}$ is deposited using an oxygen pressure of 2.5×10^{-6} Torr.

Figure 7.2 shows selected magnetization isotherms of a 15nm thin EuO film between 5 and 180 K. The behavior of the magnetization as a function of the magnetic field in EuO is consistent with the expected ferromagnetic ordering. The nonlinearity of the M vs. H behavior above the T_C=69 K indicates that short-range magnetic ordering and/or ferromagnetic clustering persist to 30K above the zero magnetic-field Curie temperature, due to a slight doping with oxygen vacancies. When comparing the magnetization curve taken at 5K for thin films of different thicknesses, one can see that the coercive field depends on the sample thickness as shown in the inset of fig. 7.3a. The thickness of the magnetic layer is calculated from the M(H) curves measured by SQUID supposing a saturation moment of $6.9\mu_B$ per

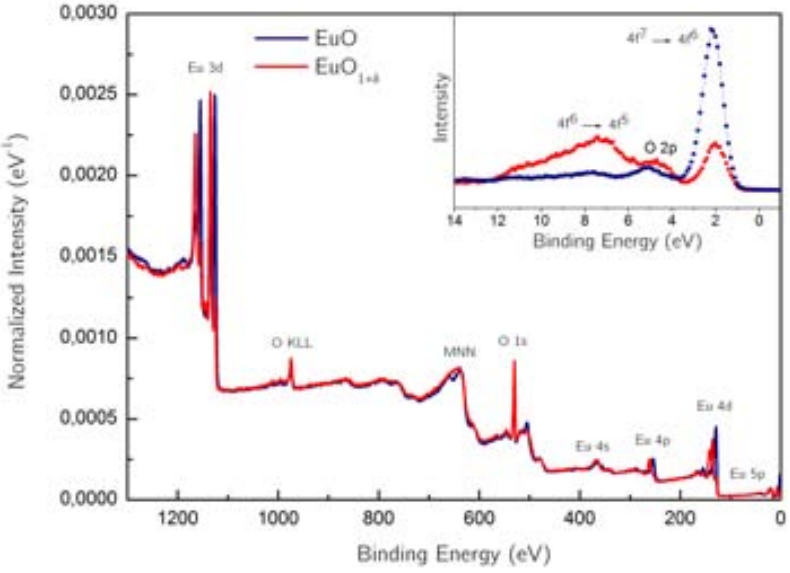

Figure 7.1: Differences in the XPS spectra for 2 different films on MgO buffered Si. The valence band spectra are shown in the inset.

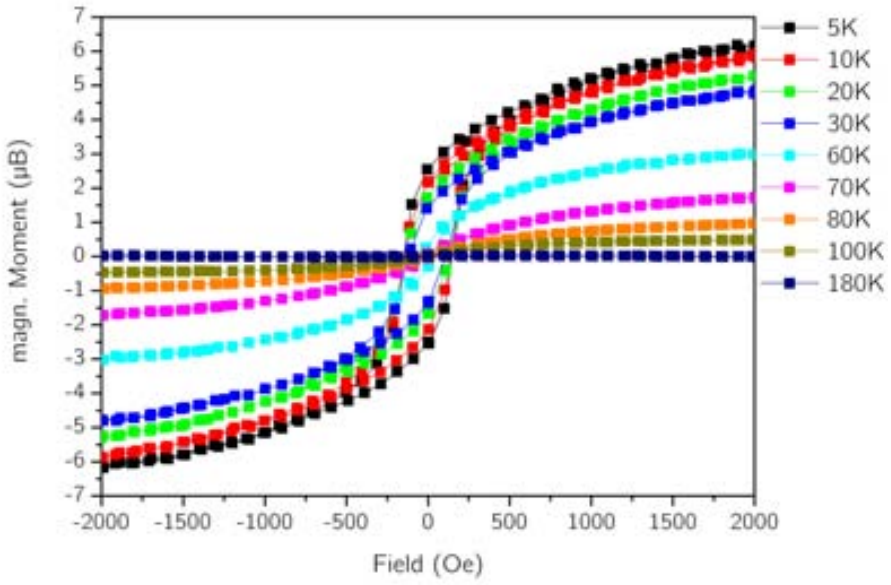

Figure 7.2: Magnetic moment of a EuO thin film on Si as a function of external magnetic field. Hysteresis is clearly observed. The coercive field at 5 K is 150 Oe.

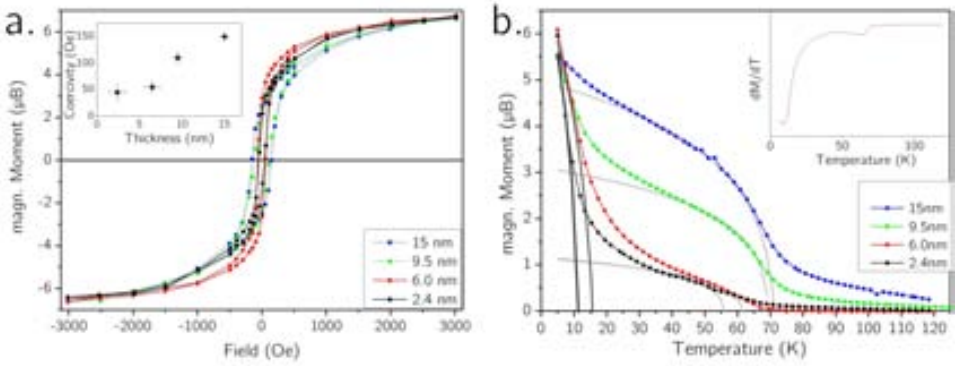

Figure 7.3: a. shows the magnetic moment at 5 K of EuO thin film of various thicknesses on Si as a function of external magnetic field. The Hysteresis curves show a thickness dependent coercive field which is shown in the inset. b. shows the M vs T curve fitted with the 2D Ising model (grey lines).

Eu atom (2.4nm, 6nm, 9.5nm and 15nm). The thickness difference between reference and sample layers obtained from perfilometry and calculated from the additional mass on the calorimeters is twice as large and has to be corrected for in the calculations afterwards. (The nominal thicknesses were 4 nm, 8 nm, 13 nm and 20 nm from XRR measurement prior to deposition.)

The coercivity is related to the rate at which magnetic relaxation between the remanent and demagnetized states takes place. At a temperature of 0K the coercive force measures the height of the barriers that must be overcome by the magnetic moments to restore equilibrium, i.e., the demagnetized state. This relaxation process involves displacements of magnetic domain walls and can therefore be strongly influenced by the film structure and thickness. The coercive fields measured in ultrathin magnetic films are orders of magnitude smaller than those of bulk samples of the same materials. This discrepancy has been attributed to the effect of step edges, such as grain boundaries which are present in our samples. In epitaxial films the decreasing coercivity could be contributed to an effect of reduced dimensionality, reflecting the evolution of the Curie temperature in the same thickness range [107]. In our case the films grew polycrystalline and the change in the coercive field can be contributed to a change in the EuO grain size. The M(T) curves in figure 7.3b. are measured in steps of 2K in a field of 1kOe on Si reference substrates, where the same stack is deposited as on the nanocalorimeters. The observed behavior is typical for a temperature-induced magnetic phase transition from a ferro- to paramagnetic state on heating. The 15nm thick samples behavior is consistent with the M(H) curves measured by VSM showing T_C=70K. By fitting with the 2D Ising

model the Curie temperature of each sample is obtained. In the films of 2.4 nm and 6 nm two different Curie temperatures are observed. The lower T_C is not due to a paramagnetic phase such as Eu_2O_3 or Eu, because in the derivative of the M vs T curve they appear as a separate peak. At the moment the lower of the 2 Curie Temperatures cannot be explained. The higher Curie temperatures follow the calculated thickness dependence [58, 59, 108], which is shown later in fig. 7.13.

7.4 Nanocalorimetry

The samples are measured in 2 different configurations, with a constant current source (Keithley 2400) and with a capacitor, as shown in figure 7.4. The constant current source (configuration 1.) has the advantage of high heating rates over large temperature ranges and easy data treatment. A box averaging process is performed after the raw data acquisition. Selecting boxes of 5 points, only signal frequencies over 100 kHz will be rejected since the acquisition is performed at 500 kHz. Most random noise is eliminated in these averaging process in time domain. Allen et al. [109] had shown that for a constant current the expression of the heat capacity can be simplified. It is important to note that the signal of the phase transition taken into account for this measurement is the differential of the amplified ΔV signal, not the V_s signal, as shown in the section 7.4.1.As the resistance of sample and reference are chosen to be equal within 1%, the differential signal can be amplified by a factor of several hundreds. This procedure significantly improves the signal-to-noise ratio and it is the key point for highly sensitive measurements. The main drawback for measurements on EuO with this technique is the transient of the current source. The time needed to reach stable operation is of the order of 100 μs, which at a heating rate of 300000 K/s means the true measurement starts 30 K above the base temperature of the calorimetric cell. As the lowest temperature of the cryostat used for these measurements is 10 K, only transitions above 40 K can be observed. This may represent a drawback for measuring the magnetic transition in very thin films of EuO, which may be depressed with respect to the bulk value of 69 K. The other configuration requires the use of a capacitor (configuration 2) that enables starting the measurement at 25 K. The current is sensed by measuring the voltage drop as a function of time on a 50 Ohm high precision resistance. It has to be taken into account that the large resistance variation during the heating scan induces a concomitant change in the current fed to the metal resistor used for heating. On the other hand, this technique allows for higher input currents and consequently higher heating rates, but leads to larger changes in the heating rate during the measurement. Since the

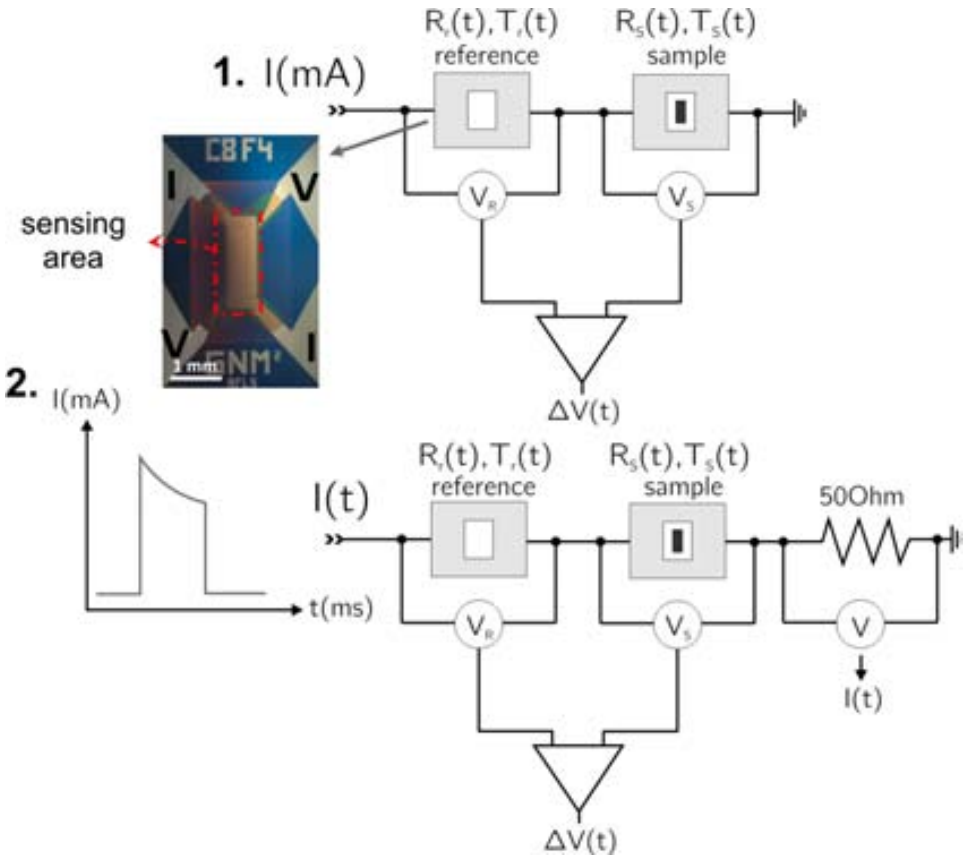

Figure 7.4: Simplified setup for the nanocalorimetric measurement. The sensing area limited by the area of the meander and the four electric contacts are shown. The current was generated mainly by a capacitor (see schematic 2.), but also rectangle current pulses were generated by a Keithley 2400 current source.

acquisition rate is constant this variation causes that few data points[1] are available in the low temperature region. In addition, the heating rate may drop by a factor of 4 leading to noisy data. Hence, this technique is best suited for phase transitions occurring at temperatures close to the starting temperature of the measurement.

Before we discuss the results of the nanocalorimetric measurement, a mathematical formalism for the EuO thin films has to be developed for calculating the heat capacity when using a capacitor. This will be described in the next section.

7.4.1 Principles
The advantage of using differential nanocalorimetry

The advantage of using differential nanocalorimetry has been previously established and permits a large increase of sensitivity by improving the signal-to-noise ratio. We will now describe the specific methodology used for the determination of the heat capacity, starting with the more general calculation using a capacitor, in which the current is not constant, but it is the same for both sample and reference.

When a current pulse is sent through the metallic heater the calorimetric cell is heated by the Joule effect. The Si frame, which is more massive than the membrane, remains at constant temperature acting as a heat sink. In quasi-adiabatic nanocalorimetry heating rates are much faster than cooling rates and therefore heat losses can be neglected. In this regime, in absence of first order phase transitions, all the Joule heat generated by the heater, is employed to increase the temperature of the calorimetric cell (sample + addenda) leading to the following relation for the heat capacity, C_P:

$$V(t) \cdot I(t)dt = C_P(T)dT \tag{7.4.1}$$

Heat losses can be safely neglected at high heating rates (10^5K/s) and low temperatures since the main thermal link between the calorimetric cell and the Si frame is through a 50 nm SiN_x membrane with a thermal conductivity as low as 2.5 W/mK.
The voltage is measured on the sensing pads and the change in resistance $R(t) = V(t)/I(t)$ of the sensing area (shown in fig. 7.4) can be obtained. To relate a certain resistance value to the sample temperature, calibration measurements $R(T)$ have to be performed beforehand. Then, one can derive the temperature of the sample as a function of time. An important improvement to this procedure is the measurement in differential configuration using a sample (S) and reference (R) cell with closely match resistance

[1] The resolution in temperature of our measurement relates like $T_{\text{resolution}} = \frac{1}{\text{acq.rate}} \frac{dT}{dt}$, where our acquisition rates at 500 Ksamples/s per channel, when using 4 channels.

heaters and heat capacities, as proposed by Allen et al. [109]. In this case, the same current pulse $I(t)$ passes through sample and reference and the response in voltage $V_{S(R)}(t)$ and $\Delta V = V_S - V_R$ measured. By introducing the heating rate $\beta_{R/S}(t) = dT_{R/S}(t)/dt$ the equation can be rewritten to:

$$C_P^{R/S}(T_{R/S}(t)) = \frac{V_{R/S}(t)I(t)}{\beta_{R/S}(t)} \tag{7.4.2}$$

The heat capacity of the empty reference cell, C_P^R, is known as the addenda heat capacity. Once the sample is grown, C_P^S consists of the addenda of the sample cell plus the contribution of the deposited sample. By measuring in differential mode we can calculate the difference in heat capacity $\Delta C_P = C_P^S - C_P^R$, before and after deposition. The subtraction of the contribution from both calorimetric cells leaves the contribution of the deposited sample. With the aim of reducing the noise we rewrite the differential heat capacity to:

$$\Delta C_P = \frac{V_S(t)I(t)}{\beta_S(t)} - \frac{V_R(t)I(t)}{\beta_R(t)} = \frac{V_R(t)I(t)}{\beta_R(t)} \left\{ \frac{V_S(t)}{V_R(t)} \times \frac{1}{\beta_S(t)/\beta_R(t)} - 1 \right\} \tag{7.4.3}$$

This expression separates the noisy expression containing $\beta_S(t)/\beta_R(t)$ which are derivatives and therefore degrade the signal-to-noise ratio [109]. To reduce the noise of the experimental data we will express this component as a function of the differential voltage ΔV. By differentiating $\Delta V = V_S - V_R$ and using $V = IR$ one can find that:

$$\frac{d\Delta V}{dt} = I(t) \left.\frac{\partial R_S}{\partial T_S}\right|_t \beta_S(t) - I(t) \left.\frac{\partial R_R}{\partial T_R}\right|_t \beta_R(t) + \frac{\Delta V(t)}{I(t)} \left.\frac{dI}{dt}\right|_t \tag{7.4.4}$$

To relate to the $\beta_S(t)/\beta_R(t)$ term we simply form:

$$\frac{\beta_S(t)}{\beta_R(t)} = \frac{\frac{d\Delta V}{dt} - \frac{\Delta V(t)}{I(t)} \left.\frac{dI}{dt}\right|_t}{\beta_R(t)I(t) \left.\frac{\partial R_S}{\partial T_S}\right|_t} + \frac{\partial R_R/\partial T_R|_t}{\partial R_S/\partial T_S|_t} \tag{7.4.5}$$

Assuming that $R_S(T_S) = R_R(T_R)$, which is the case for our calorimeters (see figure 7.5), the last term in equation 7.4.5 can be considered approximated to 1. If the signal is small, we can use the Taylor series to approximate:

$$\frac{1}{\beta_S(t)/\beta_R(t)} \cong 1 - \frac{\frac{d\Delta V}{dt} - \frac{\Delta V(t)}{I(t)} \left.\frac{dI}{dt}\right|_t}{\beta_R(t)I(t) \left.\frac{\partial R_S}{\partial T_S}\right|_t} \tag{7.4.6}$$

Inserting the obtained relation in equation 7.4.3 for ΔC_P, we rewrite:

$$\Delta C_P = \frac{V_R(t)I(t)}{\beta_R(t)} \left\{ \frac{V_S(t)}{V_R(t)} \times \left(1 - \frac{\frac{d\Delta V}{dt} - \frac{\Delta V(t)}{I(t)} \left.\frac{dI}{dt}\right|_t}{\beta_R(t)I(t) \left.\frac{\partial R_S}{\partial T_S}\right|_t} \right) - 1 \right\} \tag{7.4.7}$$

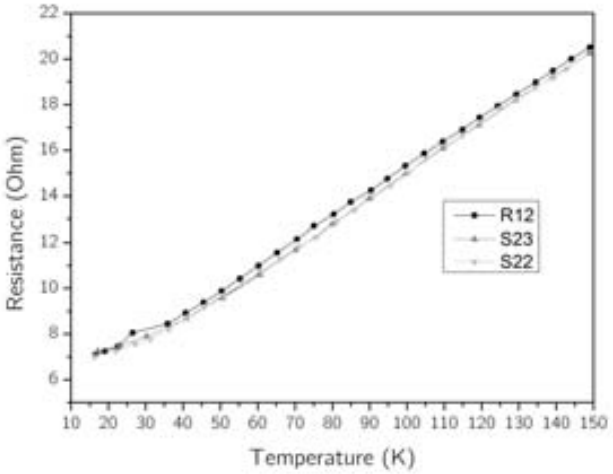

Figure 7.5: The RT calibration curves (showing the behavior expected from the the Bloch-Grüneisen function) for different pairs of calorimeters R12 being the reference for 2 different samples.

$$= \frac{\Delta V(t) I(t)}{\beta_R(t)} - \frac{V_S(t)\frac{d\Delta V}{dt} - R_S(t)\Delta V(t)\left.\frac{dI}{dt}\right|_t}{\beta_R^2 \left.\frac{\partial R_S}{\partial T_S}\right|_t} \tag{7.4.8}$$

The attenuation of noise in the β_R component is simple, because since the reference sensor has no sample on it, the β_R is a featureless and monotonic function of temperature, which can be fitted by a polynomial function. The same holds true for the $I(t)$ function, which can also be fitted.

The derivative of ΔV contains the major component of the useful signal, while the derivatives of V_S and V_R are major sources of noise. If the variation of $V_S(t)/V_R(t)$ in time cannot be neglected (if the phase transition is highly energetic or the deposited film too thick), equation 7.4.8 should be used to calculate the heat capacity of the samples.
Knowing that the resistances of sample and reference calorimeter are very similar one can approximate $V_S/V_R \cong 1$ and further simplify equation 7.4.7 to:

$$\Delta C_P = -\frac{V_R(t)}{\beta_R^2 \left.\frac{\partial R_S}{\partial T_S}\right|_t} \cdot \left(\frac{d\Delta V}{dt} - \frac{\Delta V(t)}{I(t)}\left.\frac{dI}{dt}\right|_t\right) \tag{7.4.9}$$

For constant current, the term with the derivative of the current is zero and we obtain the same equation deduced by Allen et al. [109]:

$$\Delta C_P^{Allen}(T_S(t)) = -\frac{V_R(t)}{\beta_R^2(t) \cdot \left.\frac{\partial R_S}{\partial T_S}\right|_t} \cdot \frac{d\Delta V}{dt} \tag{7.4.10}$$

To obtain the samples entropy S we consider:

$$S = S_0 + \int_0^T \frac{C_V}{T} dT \tag{7.4.11}$$

7.4.2 Corrections

As our sample consists of capping and buffer layers, which add an additional mass to our nanocalorimeter, the correction developed by Allen et al. [109] had to be redefined and adapted to our purpose. We measured the heat capacity of sample and reference calorimeter before (C_P^S, C_P^R) and after ($C_P^{S\prime}$, $C_P^{R\prime}$) deposition. Here $C_P^{S\prime} - C_P^S$ gives the contribution of the entire stack deposited on the calorimeter, while $C_P^{R\prime} - C_P^R$ gives us the contribution of the capping and buffer layers. Hence we can calculate the heat capacity of the magnetic layer of interest by:

$$C_P^{RAW}(T_S') = C_P^{S\prime}(T_S'(t')) - C_P^S(T_S'(t')) - \left[C_P^{R\prime}(T_R'(t')) - C_P^R(T_R'(t'))\right] \tag{7.4.12}$$

The fact that C_P^S and C_P^R are empty calorimeters allows us to fit them with polynomial functions as a function of T_S and T_R, respectively. As the measurement of $C_P^{S\prime}$ and $C_P^{R\prime}$ is done simultaneously, every time t' corresponds a certain T_S' and T_R' value since both cells may increase their temperature at a different rate depending on the sample heat capacity and residual differences between deposited layers. Therefore, the subtraction of values in different temperature spaces T_S' and T_R' is allowed. This explanation is given for the raw $C_P^{S/R}$ values which are very noisy. These always have to be calculated additionally to the low noise heat capacity calculated from the differential ΔV in order to correct the final result as no approximation is used.

Classical correction for empty reference cell

When the reference cell is empty (no buffer or capping layers) the main difference between sample cell and reference cell is the sample itself which induces a decrease of the heating rate of the sample cell with respect to the reference cell. As the differential voltage is measured in time domain a correction needs to be introduced. For the reference calorimetric cell, the heating rate is equal before and after sample deposition, while the sample calorimeter reduces its heating rate when the sample is present. The result is that for a given T_S' the corresponding T_R' is higher than for T_R. This introduces an error in ΔC_P when comparing the baseline with the measurement as the $C_P^S(T_R)$ value as shown in figure 7.6.

Hence the correction in heating rate gives us:

$$C_P^{betaI} = C_P + C_P^{R\prime}(T_S') - C_P^R(T_S) \tag{7.4.13}$$

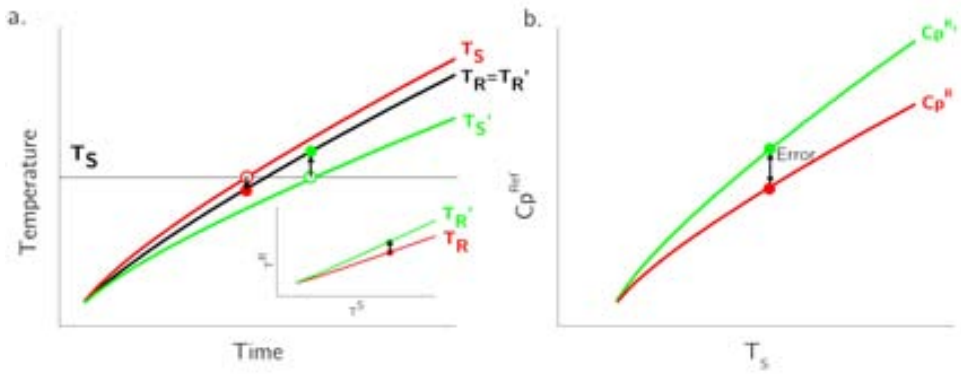

Figure 7.6: **a.** shows that without capping layer the T_R is the same before and after deposition, while the heating rate of the sample decreases after deposition. The inset shows that when a sample is present in the sample calorimeter, the apparent heating rate of T'_R seems accelerated. Which is the core of this problem.**b.** Evaluating C_P^R as a function of T_S shows that an error in the C_P is promoted, since $C_P^{R\prime}(T'_S) - C_P^R(T_S)$ is not zero, and ideally should be cancelled.

Typically, a linear/or low order polynomial fitting is applied to remove noise before the subtraction of this correction, because C_P^R does not contain any information about the phase transition itself.

Correction with buffer and/or capping layers

Supposing that sample and reference calorimeter were deposited together and hence the thickness of the capping layer perfectly coincides in both cells, the correction shown before can also be applied with few adaptations. By depositing more mass on the sample than on the reference calorimeter, the heating rate of the sample lowers more than the heating rate of the reference cell (see figure 7.7a.). In this case the heating rate of both sample and reference calorimeter lowered, when the sample and/or capping layer are deposited. To illustrate this approach we suppose, only the capping layer is deposited on the reference as well as on the sample calorimeter. Then T'_R and T'_S would lower the same amount as a function of time and when plotting the T_R vs. T_S curve, T'_R would perfectly coincide with the T_R curve before sample deposition and no corrections for a change in heating rate would have to be made.
However, in real measurements we have an additional mass (apart from the capping layer) on the sample calorimeter coming from the specimen to be analyzed. Now we fit the relation of $T_R(T_S)$ in figure 7.7b before deposition to obtain $T_R(T'_S)$ which is a necessary step for being able to

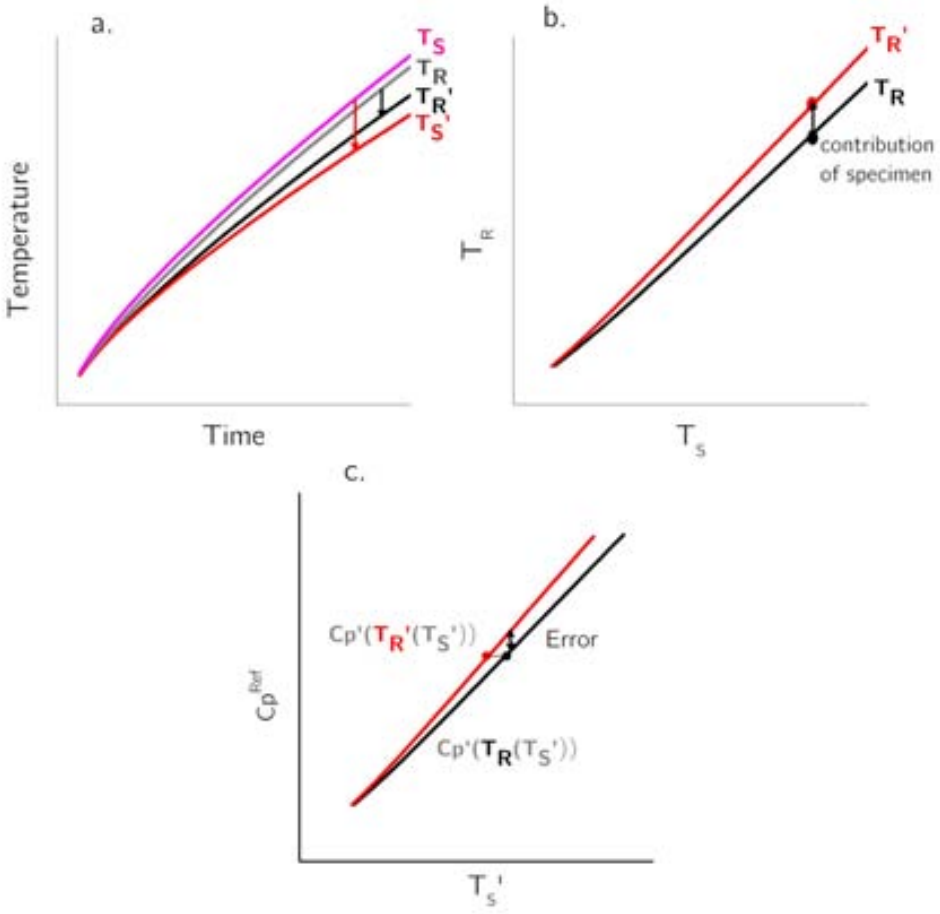

Figure 7.7: **a.** shows that with a capping layer the T'_R lowers after deposition, as well as T'_S. **b.** the enhancement of T'_R is only due to the specimen deposited on the sample calorimeter, because sample and reference temperature are lowered by exactly the same amount by to the capping layer. **c.** The reference heat capacity is evaluated $C_P^{R\prime}$ as a function of T'_S for different relations $T'_R(T'_S)$ and $T_R(T'_S)$. This shows that an error in the C_P is promoted, since $C_P^{R\prime}(T'_S) - C_P^R(T_S)$ is not zero, and ideally should be cancelled.

do the correction in the T'_S-space. $C_P^{R\prime}(T'_R)$ also has to be fitted by a low order polynomial. Hence calculating $C_P^{R\prime}(T'_R(T'_S)) - C_P^{R\prime}(T_R(T'_S))$ gives us the change ΔC_P^R in heat capacity, which results from the enhancement in the reference temperature ($\Delta T_R = (T'_R(T'_S) - (T_R(T'_S))$.

The corrected heat capacity is then given by:

$$C_P^{betaII}(T'_S) = C_P(T'_S) + C_P^{R\prime}(T'_R(T'_S)) - C_P^{R\prime}(T_R(T'_S)) \tag{7.4.14}$$

Note that this correction requires the fitting of 2 functions. Although this calculation can also be used for films without capping layer described in the chapter before, less fitting has to be done in the former case and hence less error is introduced.

7.4.2.1 Application of the corrections

As an example for the obtained calculations corrections we will calculate the heat capacity step by step and compare with standard measurements.The case of a constant current source is shown in figure 7.8, the case with a capacitor as current source is shown in figure 7.9.

As mentioned before $d\Delta V/dt$ curve is the main source of the transition signal. The small change in inclination can be attributed to the ferro- to paramagnetic phase transition, figure 7.8**a** and 7.9**a**. The previous calibration of the membranes allows us to know the temperature of the membrane corresponding to a certain resistance of the heater $R_{S/R}(T_{S/R})$. The temperature dependence in time is shown in figure 7.8**b** and 7.9**b**. Starting at the same temperature the reference calorimeter heats up faster than the sample calorimeter. This behaviour can also be observed in the corresponding heating rates. In case of the capacitor the heating rate decreases along the measurement by a factor of 4, hence the signal at higher temperatures becomes noisier. For the constant current source, the heating rate also changes by a factor of 2, but final heating rates are still higher when compared to the capacitor. The calculation of the final heat capacity is performed in the 2 ways presented before. The second line shows the calculation of the C_P using the more general formula 7.4.8, also referred to as *Model I*. To correct for different addenda between sample and reference cell the baseline, referring to ΔC_P of the empty calorimeters, has to be subtracted from the ΔC_P measured after deposition, shown in figure **c**. A correction for different heat capacity of blank sample cell at different temperatures, formula 7.4.14, has to be applied in case of using *Model I*. This results in the C_P^{beta} curve shown in figure **d**. As a last step we calculate with formula 7.4.13 the heat capacity in non-differential mode C_P^{raw} . This always has to be done to check if the approximations used for *Model I* are legitimate. In our case a small offset has to be corrected for, which was introduced by one of the approximations used for the calculations. The third line referred to as *Model II*

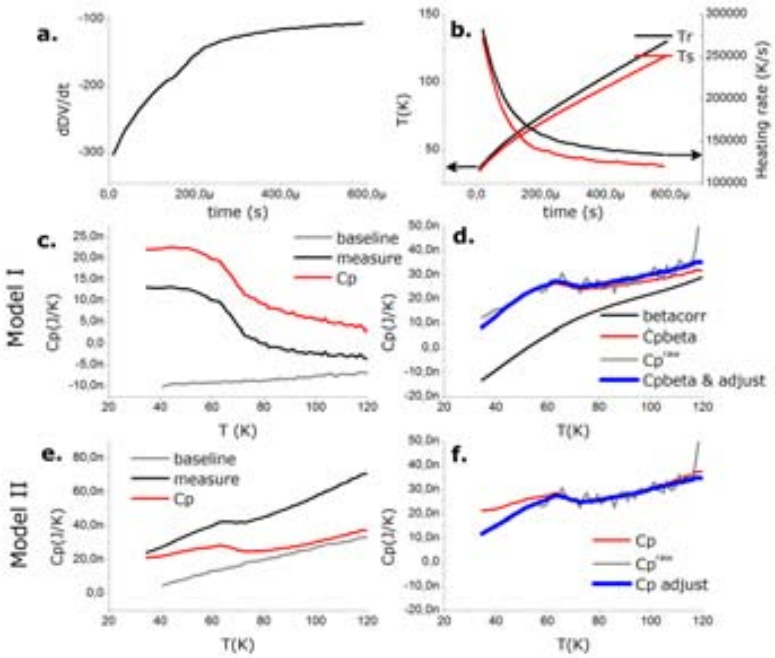

Figure 7.8: Schematic of the calculation of C_P for constant current in 2 different approaches. **a.** shows the raw $d\Delta V/dt$, which contains all the information coming from the transition. **b.** gives the conversion from time to temperature space, showing that the heating rate decreases with time. **c. and d.** describe how the differential signals calculated by formula 7.4.8 have to be corrected in order to obtain the final curve $C_P$beta & adjust. **e. and f.** show the same calculation when using the more simplified formula 7.4.10, for which in some cases like this one no correction, except the adjustment to the real C_P^{raw}, has to be done.

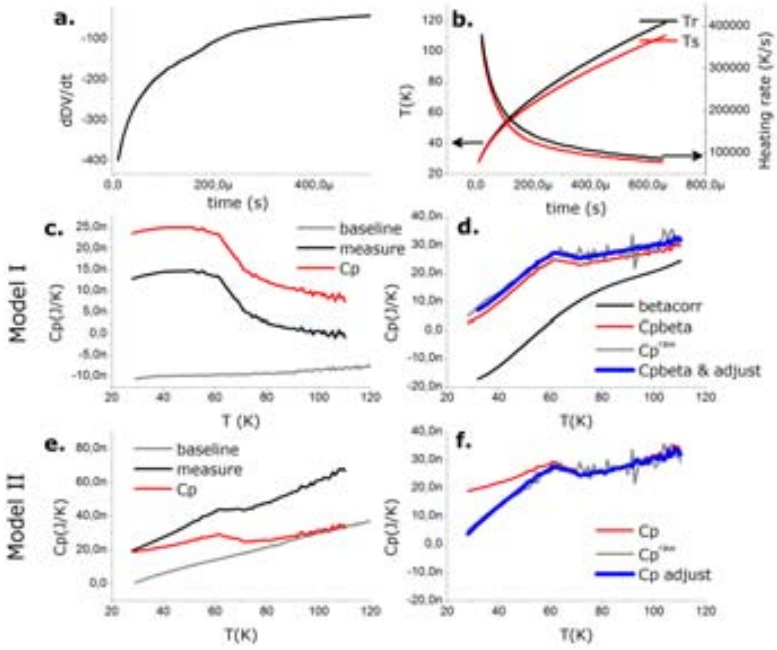

Figure 7.9: Schematic of the calculation of C_P for current from a capacitor in 2 different approaches. **a.** shows the raw $d\Delta V/dt$, which contains all the information coming from the transition. **b.** gives the conversion from time to temperature space, showing that the heating rate decreases with time more than for constant current, increasing noise at long measurements. **c. and d.** describe how the differential signals calculated by formula 7.4.8 have to be corrected in order to obtain the final curve $C_P$beta & adjust. **e. and f.** show the came calculation when using the more simplified formula 7.4.9, for which in some cases like this no correction apart from the adjustment to the real C_P^{raw} has to be done.

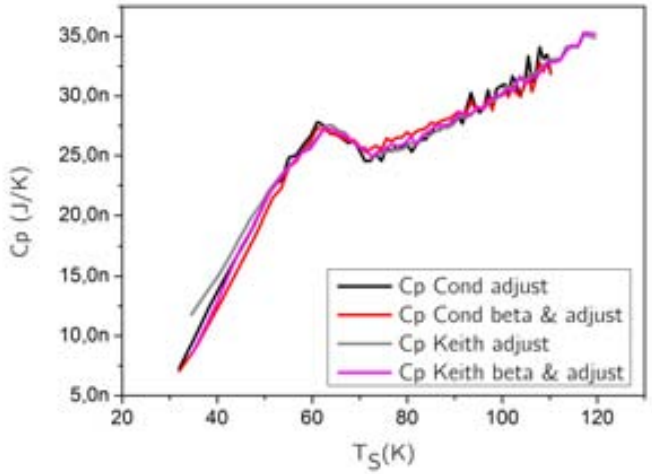

Figure 7.10: The comparison of the previous 4 results is shown. Cond refers to the calculation with the capacitor, Keith refers to the calculation with the constant current source (Keithley 2400)

shows the calculation for the simplified formula, where only the correction for different addenda is applied and then a correction to the heat capacity in non-differential mode C_P^{raw} is done.

When compared to C_P^{raw} a polynomial corrections has to be made sometimes. Though both techniques give practically the same result, the calculation of C_P the second method relies on the exactitude of very noisy data and therefore should be avoided. In figure 7.10 the results of the 4 previous methods are compared, showing that the final result is reproduced within few deviations.

7.5 Nanocalorimetric measurement of thin EuO films

Nanocalorimetric measurements are performed for several thicknesses of EuO (2.4, 6, 9.5 and 15 nm). The raw data was treated as described before in the figure 7.9a-d, resulting in the curves shown in figure 7.11a. Since only one chip could be deposited at a time in the PLD system slight deviations in the amount of capping layer, AlO_x, can occur between reference and samples. As the precise thickness of the EuO layers is determined through the T_C dependence from SQUID measurements, the specific heat capacity is calculated by taking the mass of a EuO film given that the area of the calorimetric cell is known. Due to the sequential deposition a small cor-

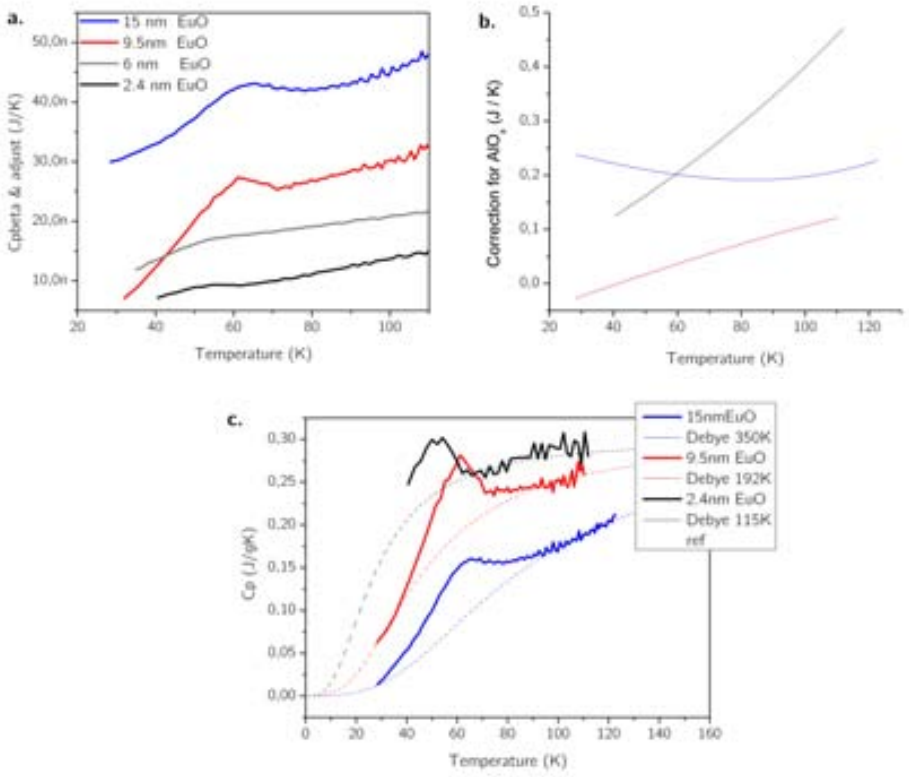

Figure 7.11: The calculated ΔC_P curves for 4 different thicknesses are shown in figure a. The correction for a certain AlO_x quantity difference between the sample and reference calorimeter is shown figure b. In figure c. these values are normalized by the EuO mass, corrected for an AlO_x layer, and compared with literature values for bulk samples [60].

rection for uncompensated AlO_x has to be applied shown in the inset. It consists of a linear part which is due to the additional mass difference and a phonon contribution $\propto (T/T_D)^3$, where the Debye temperature for Al_2O_3 is taken as 980 K. This almost linear correction is shown in figure 7.11b. Once the heat capacity is mass normalized and the correction for the excess AlO_x is performed the specific heat capacity can be decomposed in two terms: the vibrational and magnetic specific heats. It is worth to note from figure 7.11c that the occurrence of different slopes, outside the broad magnetic transition, between the various samples can be correlated with a variation of the Debye temperature. Hence, the specific heat capacity can be fitted using the a Debye model for the lattice contribution and assuming the Debye temperature is thickness dependent:

$$C_{V,latt} = 9Nk_B \left(\frac{T}{\Theta_D}\right) \int_0^{x_D} \frac{x^4 e^x}{(e^x - 1)^2} dx \tag{7.5.15}$$

where N is the number of atoms, k_B is the Boltzmann constant, Θ_D is the Debye temperature (for bulk EuO, 350 K [110]) and $x_D = \Theta_D/T$. The vibrational specific heat derived this way is illustrated by dashed lines in figure 7.11c. Note that due to the breaking of one of the voltage sensing contacts of the 6 nm EuO sample the nanocalorimetric measurement was performed in 2 points instead of 4 points. Therefore, the signal of the transition peak, though appearing at the expected temperature of 61 K, is lower than expected and is not taken into account in the calculations thereafter. The 15 nm thick sample with $T_C = T_C(bulk) = 69$K is fitted with a vibrational contribution constructed with the bulk value of the Debye temperature, $\Theta_D = 350$ K. On the contrary fitting the other specific heat curves required a significant lowering of the Debye temperature as shown in figure 7.11c. The estimated Debye temperatures roughly span from 115 to 350 K and increase with increasing film thickness. Since the Debye temperature is related to the amplitude of atomic vibration around the equilibrium positions, its reduction in nanosize materials can be attributed to the lower coordination number of surface atoms which leads to enhanced vibrational amplitudes at a given temperature. The decrease of Θ_D has been experimentally determined from measurements of resistivity in metallic thin films of gold [111], copper [112,113], platinum [114], silver films [113] or wires, and cobalt/nickel superlattices [115]. Derlet et al. [116]investigated by Molecular Dynamics the phonon DOS of model nanocrystalline samples of Ni and Cu with contributions from the inner and outer atoms of the grains and from grain boundaries. Their study indicated that grain boundary atoms are the main cause of the observed enhancement of the specific heat. Defects and impurities, as shown by inducing ion irradiation defects [117], can also lead to phonon softening. In nanocrystalline thin films, such as the ones analyzed here, the grain boundary-to-volume ratio can lead to substantial phonon

softening at the grain boundaries. Although the reduction of the Debye temperature has been predicted in a variety of materials including metals and magnetic oxides. Although the reduction of the Debye temperature has been predicted in a variety of materials including metals and magnetic oxides [118], as far as we are aware has only been experimentally observed in metal materials. Eu-doped EuO samples exhibit a metal-insulator transition at its Curie temperature, being the first material that shows a decrease of the Debye temperature in the insulating state.

In bulk magnetic materials the heat capacity [60,61] of the ferro- to paramagnetic transition appears as a delta shaped peak. However, in nanocalorimetric measurements a rounding of the transition is observed [72, 73].The rounded appearance of the maximum in Cp is a characteristic feature of the measurements in this study and it is likely related to both a temperature gradient of several degrees in the sample region and to the small size and the size distribution of the grains inside the film. A similar behavior was found by Teaney in EuO powder [60]. As rounding poses a severe constraint on the analysis of the asymptotic behavior by a power law the critical parameters were not evaluated.

The observed Debye temperatures range roughly from ∼115 to 350[2] K and tend to increase with increasing film thickness, which is also found in studies on thin investigated the phonon DOS of model nanocrystalline samples of Ni and Cu with separation of contributions from grain, grain boundaries and internal surfaces, showing that the grain boundary atoms mainly cause these enhancements. Compared with the films surface-to-volume ratio, the grain boundary-to-volume ratio of the present EuO films is in the order of the contribution of the grains making the phonon softening at the grain boundaries important. Defects and impurities, as shown by inducing ion irradiation defects [117], can also lead to phonon softening. The reduction of the Debye temperature was only observed in metal materials, Eu-doped EuO shows a metal-insulator transition at its Curie temperature being the first material that shows a decrease of the Debye temperature when in the insulating state.

By substracting the Debye contribution from the measured curve the magnetic heat capacity is obtained, as shown in figure 7.12a. We use the data from Teaney et al. [60] as reference. To allow direct comparison with our data after removing the lattice contribution we use polynomial function to obtain the correspondiong C_m curve. This procedure introduces an offset error when calculating the entropy deficit $S_{bulk} - S_{xnm}/S_{bulk}$, but the general trend is preserved. The calculated value of the bulk entropy is $S_{bulk} = 0.0426 \pm 0.001 J/(gK)$, see slashed line in figure 7.12b. Figure 7.12b

[2]A Debye temperature of 350 K corresponding to the bulk value [119])

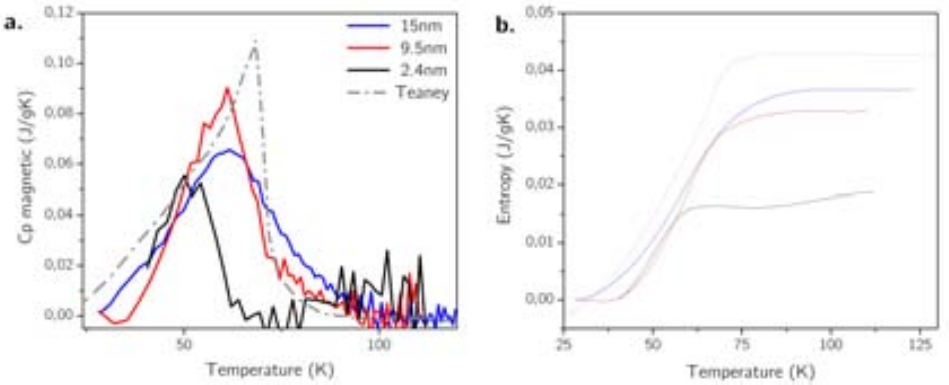

Figure 7.12: The magnetic heat capacity, after subtraction of the vibrational and electronic heat capacity, of the thin EuO films is plotted for various thicknesses in figure a. Figure b. shows the corresponding magnetic entropy obtained by integration of C_V/T. The slashed line indicates the contribution of the bulk reference [60]. In this case the magnetic signal was obtained by subtracting a polynomial function.

illustrates the magnetic entropy decreases with decreasing film thickness, as atoms at the surface of the film and near or within grain boundaries have lower coordination numbers compared to atoms in the center of the film/grains. To relate the entropy deficit to the amount of surface atoms we include those located at the surface of the nanograins. With this in mind, the grain size that explains the entropy reduction can be evaluated and is plotted in figure 7.13a. In the very early stages of growth impingement often limits the development of the fastest growth planes. Therefore, for films thinner than 4nm a spherical growth mechanism is considered, while for thicker films a columnar growth is more probable. The real grain sizes of the EuO thin films could not be measured, because the high reactivity of EuO at air prevents any TEM imaging, other than using TEM-FIB systems. Standard Theta-2Theta scans did not show enough signal to extract valuable information about grain size. An estimation can be made from the coercive field of the samples, as it is supposed to relate to the grain size d like $H_C = const. \times d^6$ [120], where the constant is a material specific parameter. The fitting of the grain sizes calculated from the entropy with this function shows a rather large deviation (fig. 7.13b.). This can be due to the large uncertainties and the offset error in the entropy evaluation.

Figure 7.13 c shows the reduction of the Curie temperature with decreasing thickness and the good agreement between nanocalorimetry and purely magnetic measurements. These results also satisfactorily agree with calculations [58, 59] of the thickness dependent electronic structure of a single-

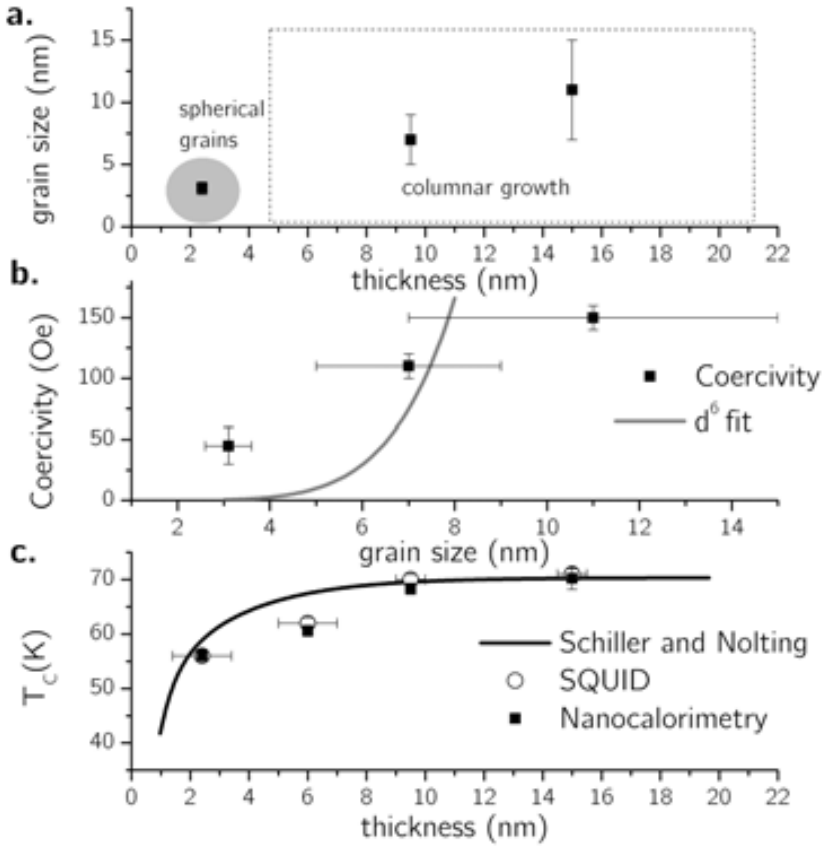

Figure 7.13: Figure a. shows the relation between the film thickness and the grain size estimated from the magnetic entropy. For the first stages a spherical growth is supposed, for thicker films the growth is columnar. Figure b. shows the relation between the grain size estimated from entropy measurements and the grain size calculated from the coercive field [120] (continous line). Figure c. shows the thickness dependence of the Curie Temperature measured by SQUID and nanocalorimetry following the predicted behavior from ref. [58].

crystal EuO(100) film as a function of temperature and thickness. The study uses a combination of the ferromagnetic Kondo-lattice model and first principles band structure calculations. They found that the T_C of thin EuO is strongly thickness dependent, starting with $T_C = 15$ K for a single monolayer (corresponding to 2.57Å). The layer-dependent magnetizations from their calculation is shown as a solid line in figure 7.13 c. The magnetization of the center layer of the film is supposed to follow the familiar shape of a ferromagnetic Brillouin function, whereas the shape of the magnetization curve for the surface layer is suppressed, corresponding to the reduced coordination number for surface atoms.

7.6 Conclusions

A new formula for the treatment of nanocalorimetric data measured with a variable current source is developed allowing a reduction of the noise in heat capacity curves. The corrections, which have to be applied when capping layers are used, are presented. The thickness dependency of the Curie temperature is observed by magnetic and calorimetric measurements, because the number of nearest magnetic interaction neighbors decreases and spins at the surface have fewer spin interactions than those in the interior. This also results in a lowering of the magnetic entropy of the transition. A reduction of the Debye temperature is observed as well, as grain boundaries, defects and impurities can result in phonon softening.

Chapter 8

Spin Polarized Tunneling through EuS Junctions

A material as reactive as Europium could not be deposited by thermal evaporation in the system described earlier in figure 3.3, as the system described earlier in figure was not in optimal conditions to reach the necessary low base pressure. In addition, the available MBE chamber was not equipped with the necessary masking strategy to *in-situ* deposit tunnel junctions of EuO. The interface of the ferromagnetic barrier with the electrodes can give rise to additional insulating atom layers, due to the reactivity of the europium monoxide with the metal electrodes, the substrate or oxygen. Hence, very few have succeeded in growing good quality EuO tunnel junctions [7, 32].
As a consequence we decided to deposit tunnel junctions of EuS, as this material is far more easy to control and less reactive than EuO. We deposited EuS tunnel junctions by e-beam and thermal evaporation. Ferromagnetic EuS barriers have shown polarization as high as 85% [8, 9] and have similar properties to EuO tunnel junctions.

8.1 Principles

Spin filter measurements are usually performed in Superconductor - Insulator - Ferromagnetic Metal (S/I/FM) structures. Instead we use a Ferromagnetic Insulator tunnel barrier, S/FI/S, where EuS is the FI. Differently to the traditional junctions, the electron spins were filtered during the tunneling (fig. 8.1) of the electrons. For spin injection and detection Al superconducting electrodes were used. In order to measure the polarization of the electron current, at least one of the electrodes has to show Zeeman splitting, where the density of states splits in two energy levels separated by $2\mu_B H$ for $\uparrow$ and $\downarrow$ electrons. Otherwise, no polarization can be detected as shown in figure 8.1b and as described before in figure 3.6. Below T_C two different barrier heights are available in the EuS barrier for spin-up ($\Phi\uparrow$) and spin-

down ($\Phi\downarrow$) electrons.

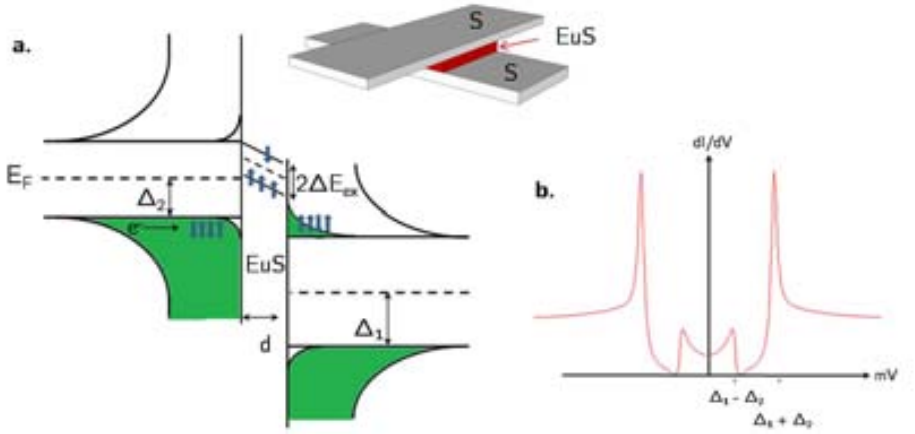

Figure 8.1: **a.** shows the principles of spin polarized tunneling for a S/EuS/S junction. Electrons with random orientation tunnel from the valence band of one S through the EuS barrier into the conduction band of the other S. The EuS has two different barrier heights for spin-up (lower barrier) and spin down (higher barrier) leading to a preferential tunneling of the spin-up electrons. If none of the superconducting electrodes shows Zeeman splitting the polarization of the current can not be detected. **b.** is the corresponding conductance curve for an arbitrary polarization, where the superconducting band gaps can be calculated from the difference peaks ($\Delta_1 - \Delta_2$) and sum peaks ($\Delta_1 + \Delta_2$).

For a given barrier thickness d, the spin-up (spin-down) tunnel current density ($J_{\uparrow(\downarrow)}$) is exponentially dependent on the tunnel barrier height $\Phi_{\uparrow(\downarrow)}$:

$$J_{\uparrow(\downarrow)} \propto \exp(-\sqrt{\Phi_{\uparrow(\downarrow)}}d) \tag{8.1.1}$$

Due to the exponential dependence even a small difference in barrier heights results in a much greater tunneling probability for spin-up electrons than for spin-down electrons, known as spin polarization P of the tunnel current:

$$P = \frac{J_\uparrow - J_\downarrow}{J_\uparrow + J_\downarrow} \tag{8.1.2}$$

The difference in the barrier height for spin up ($\Phi_\uparrow$) and spin down ($\Phi_\downarrow$) is equal to $2\Delta E_{ex}$, the magnitude of the exchange splitting of the tunnel barrier. EuS shows an exchange splitting of $2\Delta E_{ex} = 0.36$eV achieving 85% spin polarization. [8, 9].

From the difference peaks at $V_{bias}=\pm(\Delta_1 - \Delta_2)$ caused by temperature excited states and the sum peaks at $V_{bias}=\pm(\Delta_1 + \Delta_2)$ [121] one can extract the values of the energy gap $2\Delta_{1,2}$ of the 2 superconductors.

8.2 Fabrication of the Junctions

The structure is grown by thermal and electron-beam evaporation (Fig. 3.3) with a vacuum base pressure of 7×10^{-8} Torr using *in-situ* shadow masks to define the effective junction area of $200\times200\mu m^2$. In a single experiment 12 sets of tunnel junctions can be deposited on the $5\times5cm^2$ glass substrate each containing 6 tunnel junctions.

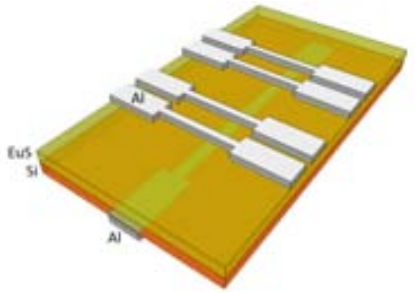

Figure 8.2: Schema of tunnel junction: side view with a junction area of 0.04 mm^2. The bottom long strip is deposited on a glass substrate.

Figure 8.2 shows the schematic of the structure (in order of deposition: Al(3.8nm)/Si/EuS/Al(10nm)) deposited on Corning 7059 borosilicate glass substrates. The bottom Al superconducting electrode and an interface layer of Si or Cu were deposited at a substrate temperature of 77K. Then the EuS barrier was grown over the whole substrate area at room temperature, in order to increase the coercive field of the EuS. At elevated growth temperature, the EuS domain size is larger compared to the deposition at 77 K, resulting in the larger coercive field [37]. These EuS films were deposited by electron-beam evaporation at a rate of approximately 0.17Å/s, with the thickness monitored by a quartz crystal monitor (error 10%).
The top aluminum superconducting electrode was deposited and capped with by a thick AlO_x film over the entire junction structure for protection. Copper and silicon are used as the interface material between the aluminium superconductor and the EuS barrier.

8.3 Experiment

Spin-polarized tunneling is an extremely interface-sensitive phenomenon, in which transport properties depend highly on the density of states at the interface between the electrode and barrier [121]. For example, the tunneling spin polarization of the electrode is the polarization at the Fermi level at the electrode/barrier interface due to the long spin life times in the aluminum electrons. Moodera et al. [122] also showed that P reduced rapidly as just two monolayers of non-magnetic Au were inserted at the Al_2O_3/Fe interface in Al/Al_2O_3/Au/Fe junctions. The aim is to investigate the exchange interaction between the ferromagnetic insulating EuS and superconducting aluminum. Therefore, the interface between them is altered by introducing several monolayers of copper or silicon, as in these materials the spin orbit scattering is relatively low ($\propto Z^4$, Z is the atomic mass). The dynamic conductance is measured in planar Al/X/EuS/Al junctions, as shown in Fig. 8.2, and the peak structure of the conductance spectra is investigated. The conductance measurements are performed in a helium cryostat at a temperature of 1K.
Initial tests of the tunnel junctions to estimate their quality and the absence of shorts are done prior to the measurements. For the measurement of the zero-bias resistance as a function of temperature a low-voltage ohmmeter, to avoid damaging the barriers, is used.
In case of EuS we see the junction getting ferromagnetic at 15K as shown

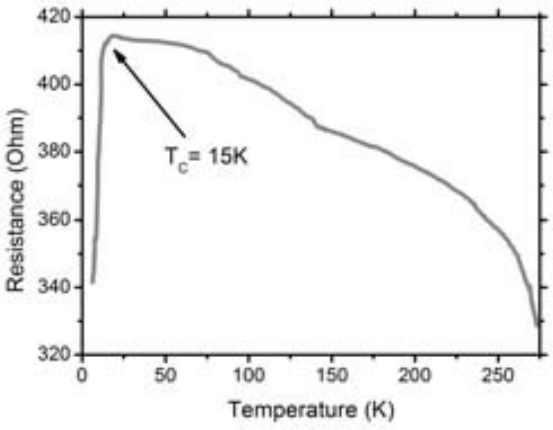

Figure 8.3: Typical behavior of a EuS tunnel junction, measured at 1μA current. In EuS barriers the resistance drops dramatically below T_C = 15K, due to exchange splitting in EuO and the resulting decrease in spin-up barrier height.

in Fig. 8.3. For non-magnetic tunnel barriers, the junction resistance would increase by 10-20% when temperature decreases, due to a reduction in the electron-phonon scattering. When our junction is cooled from room temperature, junction resistance rises rapidly, which is typical of semiconductor tunnel barriers [123], because less electrons are available in the conduction band. The opposite behavior is a sure indication that shorts dominate the measured conductance. Due to the exchange splitting of EuS at temperatures $T < T_C$ the barrier height for spin-up electrons is lowered and because of the exponential dependence of the tunnel current on barrier height (see Equation 8.1.1), resistance decreases [36].

8.4 Maki analysis on S/FI/S junctions

In contrast to the bottom electrode, the top electrode in our junctions is strongly interacting with the internal magnetic field of the ferromagnetic EuS as there is an intimate contact between the two layers. Even in zero applied field, after cooling down below the Curie temperature, Zeeman splitting is observed on the superconducting top electrode due to the internal field of EuS.
In a series of measurements at different applied fields H the superconductivity of the top electrode started breaking down, when fields higher than 60 Oe were applied. The fact that the thicker (10nm) top electrode breaks down earlier than the thinner (3.8nm) bottom electrode, is due to the $d^{-3/2}$ dependence [121] of the in-plane critical field, when d is the thickness of the superconducting Al film. The internal field of EuS can easily reach up to various Tesla and therefore goes beyond the critical field of the top electrode ($\Delta_2 = 0.173$eV), where its superconductivity breaks down. The critical field caused by Pauli paramagnetism at T=0 K can be calculated by $H_C = \Delta_{1(2)}/\sqrt{2}\mu_B$. For the top electrode the critical field should then be 2.1 T (2.5 T from conductance measurements). The bottom electrode ($\Delta_1 = 0.351$eV) is capped with Si, Cu or a native layer of Al_2O_3. The interaction with the EuS magnetic field is therefore weakened and the bottom electrode doesn't show any Zeeman splitting (see figure 8.4) . The junctions with Si as an interlayer show spin polarizations up to 47%, slightly lower than junctions with Al_2O_3 and Cu as interlayer, which show spin polarizations up to 56% (the same was measured for junctions without any interlayer). This information is obtained from the fitting (Fig. 8.4) of the conductance curve with Maki's theorem [124], which is slightly altered for two superconducting electrodes instead of only one by Moodera *et al.* Spin polarizations of up to 85% have already been reported by Moodera [8] and Hao [9], but couldn't be reproduced as the superconductivity of the top electrode that shows Zeeman splitting broke down. The resistances of the junctions with Si generally are a factor 5 lower than in junctions with other

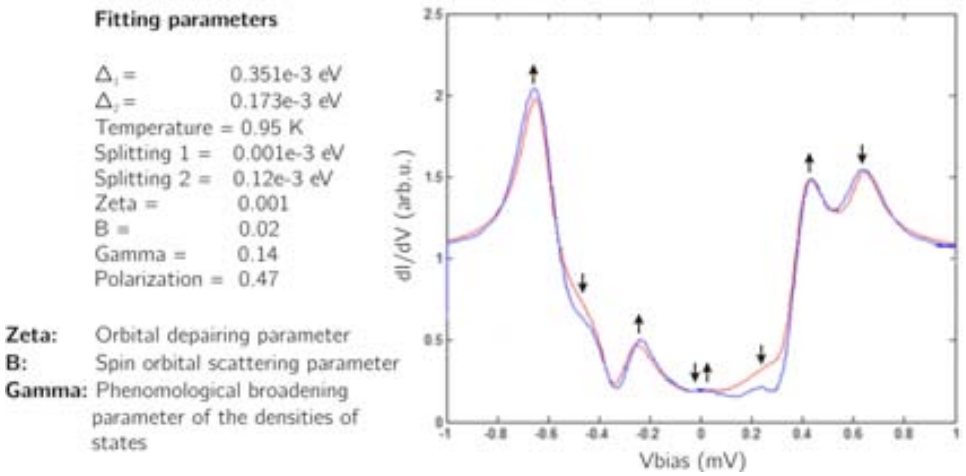

Figure 8.4: Typical maki fitting of a Al(3.8nm)-Si(1.2nm)-EuS(2.1nm)-Al(10nm) junction in a field of 27 Oe showing the parameters that can be obtained. The arrows indicate the spin directions of the peaks.

interlayers indicating a higher roughness, though the Si film was deposited at liquid-nitrogen temperature to increase the uniformity.

The spin orbit-scattering mechanism can be explained by the following model. If a non-magnetic impurity is present in the periodic lattice, this results in a distortion of its periodic electric field. A fast moving electron will interact with the distortion, which appears to the electron as an time-varying magnetic field which can flip the electron spin. In comparison to scattering by magnetic impurities as described in chapter 8.5 by the Kondo-effect, this process is time-reversal invariant.
The normalized spin-orbit scattering parameter $B = \hbar/3\Delta\tau_{so} = 0.02$ is near the literature value for Al (0.05 [121]) indicating that none of the introduced interlayers alters the spin-orbit scattering. Here Δ is the superconducting order parameter and $\tau_{so}^{-1} \propto Z^4$ is the spin-orbit scattering rate proportional to the fourth power of the atomic number Z.

In tunneling experiment in a magnetic field, the orbital depairing parameter Zeta affects the measured conductance simply by a broadening of the density of states with increasing applied field. It's a result of the Meissner screening currents. The highest current a superconductor can carry is described by the depairing mechanism: when the kinetic energy associated with the supercurrent exceeds the condensation energy (e.g., the binding energy of Cooper pairs), superconductivity vanishes.
In the case of a thin Al film with the magnetic field parallel to the film plane,

the orbital response is largely suppressed, resulting in almost very low values of Zeta. This is because the film thickness d is less than the penetration depth and with the field applied in the plane of the film, the Meissner screening currents are minimal and the field penetrates the film nearly uniformly. If the magnetic field was applied normal to the sample surface, the resulting screening currents and hence Zeta would be much higher.

8.5 Zero bias conductance peak

A few of the samples with a relatively low resistance of 100 Ohm where silicon is grown as an interlayer showed a conductance peak (ZBCP) at zero bias voltage. This anomalous peak could be suppressed by applying a magnetic field (see fig. 8.5a.). To guarantee that the measurements are correct we carried out both, 2- and 4 point measurements. Additionally, the long and cross strip are measured separately. By measuring the magnitude of the ZBCP as a function of applied field, the hysteretic nature of this peak with a coercive field of 200 Oe is observed (shown in fig. 8.5b.). Also time dependent measurements discussed in the next section show relaxation behaviour. The IV curve shown in figure 8.5c is obtained by integration of the conductance curves indicate the existence of a Josephson current in the junction, as discussed below. Temperature dependent measurements (see fig. 8.5d. and e.) show a BCS type behavior as the cross strip becomes normal conducting during warming up and its superconductivity breaks down. This indicates, that the ZBCP depends on the superconductivity of the top electrode.

The absence of the Zeeman splitting in the superconducting aluminum is probably due to the insufficient vacuum in the deposition system and therefore related to the low quality of the electrodes. Therefore, no value for the polarization of the conducting electrons can be obtained in these samples showing ZBCP. However, we can clearly observe the superconducting density of states of both aluminum electrodes with band gaps $\Delta_{1(2)}$ of 0.31mV and 0.17mV. The origin of the anomalous zero bias conductance peak (ZBCP) may, in principle, be related to several phenomena:

Kondo effect [125, 126] The Kondo effect describes the scattering of conduction electrons in a metal due to magnetic impurities, which could be the case if the thickness of EuS is smaller than read on the crystal monitor or the deposited EuS is of poor quality. The Appelbaum model [127] describing this effect, was generally developed for metal-insulator-metal junctions and was later applied to d-wave superconductors showing ZBCP [128]. In the case of an s-wave superconductor as aluminum simulations don't show the observed behavior of the ZBCP when adapting the Appelbaum model to simulate the conductance of the tunnel junction.

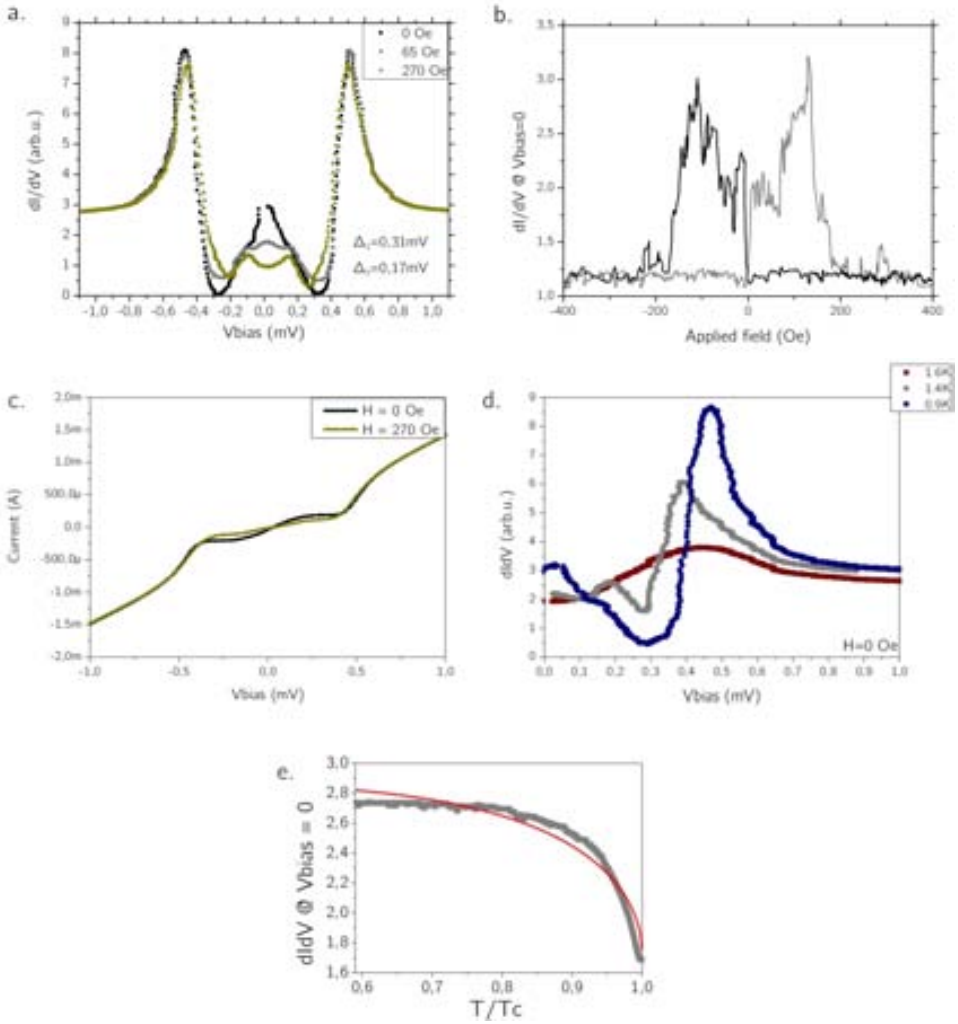

Figure 8.5: Fig. a. shows the conductance measurement of the EuS junction with Si as interlayer (Al (3.8nm)-Si (1.1nm)-EuS (2.2nm)-Al (10nm)). The ZBPC depends on the applied magnetic field. b. shows the dependence of the ZBCP with the magnetic field and c. shows the effect of the ZBCP on the IV curve (integrated from a.). Figure d. shows the temperature dependence of the conductance. The height of the ZBCP as a function of temperature is shown in figure e, where the red line indicates BCS like behavior.

Blonder-Tinkham-Klapwijk (BTK) model The BTK-model can be applied supposing we have a small short path in our tunnel junction which superposes with the normal tunneling characteristics. Joost

Beukers[1] simulated these short paths, which give rise to typical Andreev reflection at the metal-superconductor interface. The incoming electron (↑) from the metal is reflected as a hole (↓) with the same momentum and opposite velocity. The missing charge of 2e (↑↓) is absorbed as a Cooper pair by the superconducting condensate. In the optimal case such a ZBCP should show twice the height at zero bias in comparison to high bias, which is not observed (Fig. 3.6 a.). For different transmission values of the barrier between metal and superconductor an extra variable is introduced into the equations. In ferromagnetic metals an additional limitation occurs as the Andreev reflection is limited by a minority spin population. This situation was first considered by de Jong and Beenakker [129], when they discussed Andreev reflection at the interface between a half-metal (which is 100% spin polarized) and a conventional superconductor. Andreev reflection is then forbidden, as there are no states for a hole to get reflected to, resulting in zero conductance across the interface below the gap. Simulations for various polarizations of the conducting electron spins in our junction showed much broader ZBCPs than experimentally observed, as the ZBCP should have a width in the order of the superconducting gap.

Proximity effect [130, 131] The Proximity effect occurs when a superconductor is in contact with a normal metal and the injected Cooper pair density decays in the normal metal over a certain distance (the coherence length). Here, superconducting properties are induced in the normal metal layer and at the same time superconductivity is weakened in the superconductor.
At the S/FM interface the Cooper pair density not only decays over the coherence distance, but acquires a spatially dependent phase inside the ferromagnet. This is a consequence of ΔE_{ex} splitting the FM band structure, meaning that spin-up and spin-down electrons experience different barrier heights. This results in damped oscillations of the superconductor long range parameter, leading to band inversion as a function of the film thickness of the ferromagnetic layer in M/FM/S junctions. In our case no band inversion is observed in other samples with the same EuS thickness. Also, the ZBCP would not show the observed magnetic behaviour. As we have two superconducting layers (S/FM/S) the corresponding effect is described in the next section.

Josephson junctions - weak links In S/I/S junctions [132] (where I is a non-magnetic insulating tunnel barrier) similar phenomena occur as describe in the proximity effect. A supercurrent through such a junction is given by $I = I_C \sin(\phi)$ there ϕ is the phase difference of the

[1] University of Twente, 7500 AE Enschede, The Netherlands

wave functions of the two superconducting electrodes and I_C is the maximum supercurrent that can pass through the junction. When no current passes through a Josephson junction $\phi = 0$ corresponds to the energy minimum, $\phi = \pi$ corresponds to the energy maximum and is unstable. This characterizes a typical **0 Josephson junction**.
In junctions with a ferromagnetic interlayer S/FM/S the order parameter oscillates as perpendicular to the junction plane and it can go through zero at the center of the FM layer, if the FM thickness is of the order of half the oscillation length. Hence a state with the opposite sign of the order parameter (equal to a shift of π) is provided in the second superconducting layer. In such a junction the critical current is negative $I = -I_C \sin(\phi) = I_C \sin(\phi + \pi)$. Such a π **Josephson junction** has $\phi = \pi$ as ground state and $\phi = 0$ as unstable energy maximum. Until recently the π Josephson junctions have been limited to systems using metallic ferromagnetic as a barrier [133, 134]. Senapati et al. [135] observed Josephson junctions using a ferromagnetic isolating tunnel barrier (NbN/GdN/NbN). The characteristic Fraunhofer pattern of the critical current as a function of magnetic field applied perpendicular to the junction are measured. In difference to normal Josephson junctions, a hysteretic behavior of the Fraunhofer pattern due to the magnetic GdN hysteresis, a strong suppression of the critical current and a deviation from the BCS gap equation, due to the filter effect of the ferromagnetic insulating barrier, are observed.
In our case the ZBCP is suppressed by the application of an external magnetic field and the junction shows typical ohmic behavior (Fig. 8.5c.). In case of zero applied field, the presence of an increased, concave shaped DC current near zero bias indicates that two superconductors are weakly coupled. A similar behavior of the IV curve is shown in reference [135], where the step like behavior is a result of the lock-in oscillation broadening.

One reason why we only observed the ZBCP only in junctions with silicon and not with copper or just aluminum could be related to the roughness of the silicon surface. However, as the depositions of the bottom electrode were made at 77K, we expect the surface to be inherently smooth.

8.5.1 Relaxation behavior of the Zero bias conduction peak

Apart from the dependence of the magnetic field and the temperature, we also observe a relaxation behavior with time. This allows drawing conclusions about the switching of the different EuS grains as superconductivity can be killed by the internal magnetic field of EuS. The sample is magnetically saturated in one direction and then subjected to an abruptly applied (step-function) field in the opposite direction. The subsequent change in magnetization is then detected and recorded as a function of time in the

presence of the constant reverse field (fig.8.6a.). As a first approximation the curves are fitted by a simple exponential function $N_0 \exp(-t/\tau)$ allowing us to extract the mean relaxation time τ for a series of applied fields as shown in figure 8.6c. Note that the fitting is performed for negative as well as positive values of applied magnetic field H and the absolute value H is shown. A tendency to higher relaxation times for higher applied fields can be observed. This could be due to the rather small fraction of material that easily orientates at low fields (fig. 8.6d.). At higher fields the relaxation time is higher as grains align stepwise to the externally applied field.

In the Sharrock model [136] each curve can be understood as representing

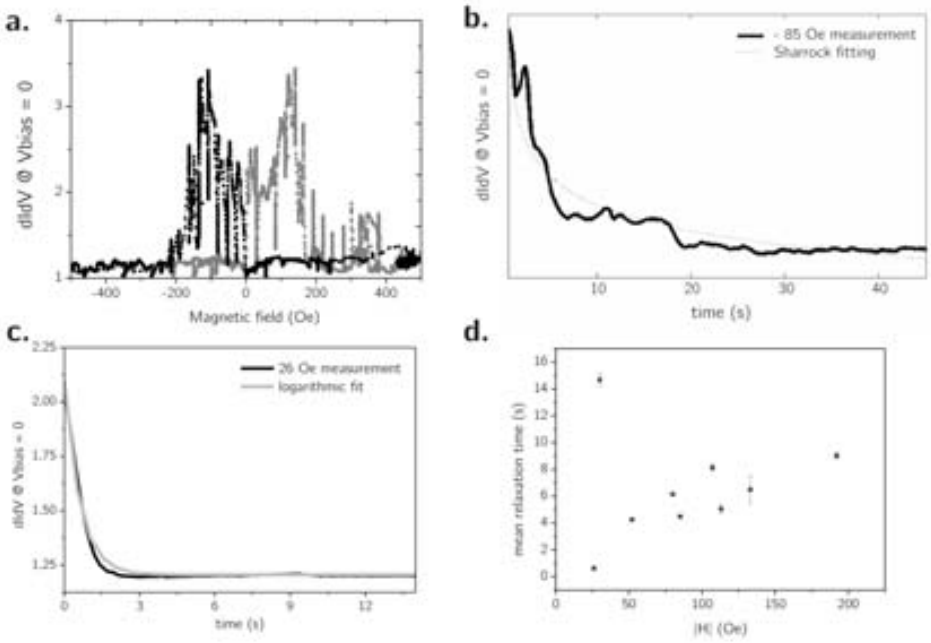

Figure 8.6: a. shows the relaxation measurements performed on the EuS tunnel junction. In figure b. the fitting with the Sharrock model [136] (dotted line) of one of the magnetization curves as a function of time is shown. c. shows the exponentially fitted curves, where the relaxation times can be calculated which are shown in figure d. as function of applied field.

a sum of logarithmic curves, whose decay constants span a large range. The overall behavior closely resembles that of simple logarithmic functions (see figure 8.6b.). A simple model of the magnetic switching of non-interacting grains at finite temperature assumes that reversal depends only on the size of the magnetic grain. It allows us to fit the relaxation curves with

$$m(t) = M(t)/M_R = B(H_0 - H) - C_{1/2}\sqrt{\log At}$$

where B, H_0 and $C_{1/2}$ are constants to be determined by fitting and M_R is the remanent magnetization. With $H_0 = 2K/M_s$ being the effective perpendicular anisotropy field and $C_{1/2}/BH_0 = \sqrt{2.303 \times k_B T/KV}$ one can calculate the anisotropy constant K and the volume of the magnetic grain V. For our EuS junction we get $B = (7.2 \pm 0.9) \times 10^{-3}$ Oe^{-1}, $H_0 = (230 \pm 60)$ Oe and $C_{1/2} = (0.20 \pm 0.07)$ Oe^{-1}. To calculate the bulk saturation magnetization M_s of EuS, we use the saturation magnetic moment of 7 μ_B and a density of 5.8 g/cm^3 and get $M_s = 1231$ emu/cm^3. We can estimate a value for the magnetic switching grain size of about (150 ± 100)nm^3 and an anisotropy constant K of $(1.4 \pm 0.4) \times 10^5$. Earlier depositions in this equipment [37] showed that the EuS deposited at room temperature shows a rounded hysteresis loop shape the indicating increased angular dispersion of domain magnetization vectors due to the nucleation of additional domain walls.
However a HR-TEM analysis of similar samples on copper as shown in figure 8.7 in the next section suggests that the EuS barrier consists of polycrystalline grains with a maximum grain size of $10nm^3$. This is not entirely in disagreement with the calculated magnetic grain size of (150 ± 100)nm^3 as the magnetic grain size does not have to coincide with the crystalline grain, but it is mainly dominated by domain walls.

8.5.2 TEM analysis

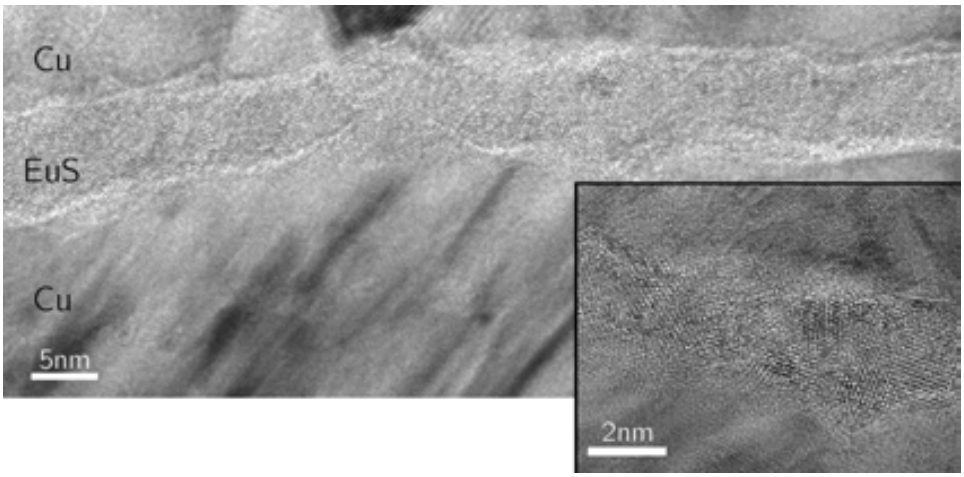

Figure 8.7: A cross section TEM measurement of a Cu-EuS-Cu junction. The inset shows a high resolution image where the polycrystalline grains are clearly visible.

To get more structural information about the EuS tunnel barrier, a high resolution transmission electron microscopy (HR-TEM) analysis is per-

formed. The transmission pattern of high energy electrons (30 keV) is recorded by Joost Beukers at the University of Twente. An EuS tunnel junction with 2 copper layers, where the bottom Cu is grown at 77K and the EuS barrier and the top Cu electrode are grown at room temperature. The EuS is deposited at room temperature in order to increase to coercive field of the EuS, as at higher growth temperatures the EuS domain size is larger compared resulting in a larger coercive field.
The thickness of (4 ± 2)nm of the EuS barrier is in agreement with the reading on the crystal monitor. A peak to peak roughness of the electrodes of 4nm is observed, but no pinholes are observed across the whole junction area. Note that the dimensions of the film may not be completely correct, as the glass substrate is amorphous it is impossible to align the cross sectional plane of the sample parallel to the electron beam. As a result the projection plane contains information of not only one single atomic sheet but also of neighboring planes. This effect seems to over estimate the roughness of the separate electrodes and barriers. No ordering of atomic planes is visible, as expected from the deposition conditions. Texture shows a polycrystalline EuS barrier.

8.6 Conclusions

Though EuO is an ideal spin filter tunnel barrier, the instability of EuO could easily lead to the formation of higher oxides at the interface adding a barrier between EuO and the superconducting electrode. To avoid this issue EuS tunnel junctions are deposited by thermal evaporation. The maximum obtained spin polarization, measured on an Al(3.8nm)-Si(1.2nm)-EuS(2.1nm)- Al(10nm) junction is 47% while for the same junction with 0.3nm Cu as well as without any interlayer a higher spin polarization of about 56% was calculated. Some of the junctions with a silicon interlayer showed a zero bias conductance peak, indicating the presence of a Josephson current between the two aluminium superconducting electrodes. This would be the first time a supercurrent through the EuS barrier has been measured through a europium monochalcogenide spin filter barrier. Further investigation of this observation in terms of Shapiro steps or the Fraunhofer pattern in structured EuS Josephson junctions is important the completely specify the behavior of such a spin filter Josephson junction.

Chapter 9

Outlook

The growth of single crystal epitaxial EuO or Ni on a new generation of nanocalorimeters having a single crystal Si surface would allow be interesting. A comparison of polycrystalline and epitaxial samples would be the best proof that the decrease of the magnetic moment is due to the interfaces of grains inside thin films. Also the further develpoment of a cryostate, where nanocalorimetric measurements can be performed as a function of applied magnetic field would give more, is a project that is very interesting for measurements of magnetic films.

Bibliography

[1] K. J. Hubbard and D. G. Schlom: *Thermodynamic stability of binary oxides in contact with silicon.* Journal of Materials Research, **11** (1996), no. 11, pp. 2757–2776

[2] A. Schmehl *et al.*: *Epitaxial integration of the highly spin-polarized ferromagnetic semiconductor EuO with silicon and GaN.* Nature materials, **6** (2007), no. 11, pp. 882–887

[3] J. Lettieri *et al.*: *Epitaxial growth and magnetic properties of EuO on (001) Si by molecular-beam epitaxy.* Applied Physics Letters, **83** (2003), no. 5, pp. 975–977

[4] C. Godart, A. Mauger, J. P. Desfours and J. C. Achard: *Physical properties of EuO versus electronic concentrations.* Le Journal de Physique Colloques, **41** (1980), no. C5, pp. 205–214

[5] I. Žutić, J. Fabian and S. Das Sarma: *Spintronics: Fundamentals and applications.* Reviews of Modern Physics, **76** (2004), no. 2, pp. 323–410

[6] J. S. Moodera, T. S. Santos and T. Nagahama: *The phenomena of spin-filter tunnelling.* Journal of Physics: Condensed Matter, **19** (2007), no. 16, p. 165202

[7] T. Santos and J. Moodera: *Observation of spin filtering with a ferromagnetic EuO tunnel barrier.* Physical Review B, **69** (2004), no. 24, p. 241203

[8] J. S. Moodera, X. Hao, G. A. Gibson and R. Meservey: *Electron-Spin Polarization in Tunnel Junctions in Zero Applied Field with Ferromagnetic EuS Barriers.* Physical Review Letters, **61** (1988), no. 5, pp. 637–640

[9] X. Hao, J. Moodera and R. Meservey: *Spin-filter effect of ferromagnetic europium sulfide tunnel barriers.* Physical Review B, **42** (1990), no. 13, p. 8235

[10] M. Ohring: *Materials Science of Thin Films*. second edition (2002)

[11] D. McWhan, P. Souers and G. Jura: *Magnetic and structural properties of europium metal and europium monoxide at high pressure*. Physical Review, **143** (1966), no. 2, p. 385

[12] J. M. Haschke and H. A. Eick: *Vaporization thermodynamics of europium monoxide*. The Journal of Physical Chemistry, **73** (1969), no. 2, pp. 374–377

[13] J. Schoenes and P. Wachter: *Exchange optics in Gd-doped EuO*. Physical Review B, **9** (1974), no. 7, pp. 3097–3105

[14] O. W. Dietrich, A. J. Henderson and H. Meyer: *Spin-wave analysis of specific heat and magnetization in EuO and EuS*. Physical Review B, **12** (1975), no. 7, pp. 2844–2855

[15] K. Lee and J. C. Suits: *Reduction of ferromagnetic Exchange with lattice dilation in EuO*. Journal of Applied Physics, **41** (1970), no. 3, pp. 954–956

[16] J. Coburn and K. Lee: *Sputter deposition of EuO Thin Films*. Journal of Applied Physics, **42** (1971), no. 13, pp. 5903–5905

[17] K. Y. Ahn and J. Suits: *Preparation and properties of EuO films*. IEEE Transactions on Magnetics, **3** (1967), no. 3, pp. 453–455

[18] K. Y. Ahn and T. R. McGuire: *Magnetic and Magneto-optic Properties of EuO Films Doped with Trivalent Rare-Earth Oxide*. Journal of Applied Physics, **39** (1968), no. 11, p. 5061

[19] K. Y. Ahn and M. W. Shafer: *Relationship Between Stoichiometry and Properties of EuO Films*. Journal of Applied Physics, **41** (1970), no. 3, p. 1260

[20] K. Lee and J. Suits: *Preparation of doped EuO films on rotating disks*. Magnetics, IEEE Transactions on, **7** (1971), no. 3, pp. 391–391

[21] K. Lee and J. Suits: *Enhanced ferromagnetic exchange in EuO films doped with Eu and non-magnetic ions*. Physics Letters A, **34** (1971), no. 3, pp. 141–142

[22] C. Paparoditis *et al.*: *Transport properties of Europium oxide thin films*. Solid State Communications, **9** (1971), no. 21, pp. 1871–1876

[23] O. Massenet, Y. Capiomont and N. Van Dang: *Effects of high nonstoichiometry on EuO properties*. Journal of Applied Physics, **45** (1974), no. 8, pp. 3593–3599

[24] R. Sutarto *et al.*: *Epitaxy, stoichiometry, and magnetic properties of Gd-doped EuO films on YSZ (001).* Physical Review B, **80** (2009), no. 8, p. 085308

[25] A. G. Swartz *et al.*: *Epitaxial EuO thin films on GaAs.* Applied Physics Letters, **97** (2010), no. 11, p. 112509

[26] J. Holroyd, Y. U. Idzerda and S. Stadler: *Properties of thin film europium oxide by x-ray magnetic circular dichroism.* Journal of Applied Physics, **95** (2004), no. 11, p. 6571

[27] N. Iwata, G. Pindoria, T. Morishita and K. Kohn: *Preparation and Magnetic Properties of EuO Thin Films Epitaxially Grown on MgO and SrTiO3 Substrates.* Journal of the Physics Society Japan, **69** (2000), no. 1, pp. 230–236

[28] J. Beukers *et al.*: *Epitaxial EuO thin films by pulsed laser deposition monitored by in situ x-ray photoelectron spectroscopy.* Thin Solid Films, **518** (2010), no. 18, pp. 5173–5176

[29] R. W. Ulbricht *et al.*: *Adsorption-controlled growth of EuO by molecular-beam epitaxy.* Applied Physics Letters, **93** (2008), no. 10, p. 102105

[30] T. Yamasaki *et al.*: *Observation of anomalous Hall effect in EuO epitaxial thin films grown by a pulse laser deposition.* Applied Physics Letters, **98** (2011), no. 8, p. 082116

[31] M. Barbagallo *et al.*: *Experimental and theoretical analysis of magnetic moment enhancement in oxygen-deficient EuO.* Physical Review B, **81** (2010), no. 23, p. 235216

[32] C. Caspers *et al.*: *Electronic structure of EuO spin filter tunnel contacts directly on silicon.* physica status solidi (RRL) - Rapid Research Letters, **5** (2011), no. 12, pp. 441–443

[33] C. Caspers *et al.*: *Chemical stability of the magnetic oxide EuO directly on silicon observed by hard x-ray photoemission spectroscopy.* Physical Review B, **84** (2011), no. 20, p. 205217

[34] R. Panguluri *et al.*: *Half-metallicity in europium oxide conductively matched with silicon.* Physical Review B, **78** (2008), no. 12, p. 125307

[35] M. Barbagallo *et al.*: *Thickness-dependent magnetic properties of oxygen-deficient EuO.* Physical Review B, **84** (2011), no. 7, p. 075219

[36] T. Santos *et al.*: *Determining Exchange Splitting in a Magnetic Semiconductor by Spin-Filter Tunneling.* Physical Review Letters, **101** (2008), no. 14, p. 147201

[37] G.-X. Miao and J. S. Moodera: *Controlling magnetic switching properties of EuS for constructing double spin filter magnetic tunnel junctions.* Applied Physics Letters, **94** (2009), no. 18, p. 182504

[38] D. Förster *et al.*: *Epitaxial europium oxide on Ni(100) with single-crystal quality.* Physical Review B, **83** (2011), no. 4, p. 045424

[39] T. Santos: *Europium oxide as a perfect electron spin filter.* Ph.D. thesis (2007)

[40] M. Horne *et al.*: *The electronic structure of europium chalcogenides and pnictides.* Journal of Physics: Condensed Matter, **16** (2004), no. 28, pp. 5061–5070

[41] D. Ghosh, M. De and S. De: *Electronic structure and magneto-optical properties of magnetic semiconductors: Europium monochalcogenides.* Physical Review B, **70** (2004), no. 11, p. 115211

[42] G. Busch, P. Junod and P. Wachter: *Optical absorption of ferro- and antiferromagnetic europium chalcogenides.* Physics Letters, **12** (1964), no. 1, pp. 11–12

[43] W. Heisenberg: *Zur Theorie des Ferromagnetismus.* Zeitschrift für Physik, **49** (1928), no. 9-10, pp. 619–636

[44] A. Mauger and C. Godart: *The magnetic, optical, and transport properties of representatives of a class of magnetic semiconductors: The europium chalcogenides.* Physics Reports, **141** (1986), no. 2-3, pp. 51–176

[45] T. Kasuya: *Exchange Mechanisms in Europium Chalcogenides.* IBM Journal of Research and Development, **14** (1970), no. 3, pp. 214–223

[46] M. W. Shafer and T. R. McGuire: *Studies of Curie-Point Increases in EuO.* Journal of Applied Physics, **39** (1968), no. 2, p. 588

[47] H. Ott *et al.*: *Soft x-ray magnetic circular dichroism study on Gd-doped EuO thin films.* Physical Review B, **73** (2006), no. 9, p. 094407

[48] H. Miyazaki *et al.*: *La-doped EuO: A rare earth ferromagnetic semiconductor with the highest Curie temperature.* Applied Physics Letters, **96** (2010), no. 23, p. 232503

[49] P. Liu *et al.*: *Ce-doped EuO: Magnetic properties and the indirect band gap.* Journal of Applied Physics, **109** (2011), no. 7, p. 07C311

[50] A. Melville *et al.*: *Lutetium-doped EuO films grown by molecular-beam epitaxy.* Applied Physics Letters, **100** (2012), no. 22, p. 222101

[51] T. Kasuya and A. Yanase: *Anomalous transport phenomena in Eu-chalcogenide alloys.* Reviews of Modern Physics, **40** (1968), no. 4, p. 684

[52] G. Petrich, S. von Molnár and T. Penny: *Exchange-Induced Autoionization in Eu-rich EuO.* Physical Review Letters, **26** (1971), no. 15, p. 885

[53] P. Steeneken *et al.*: *Exchange Splitting and Charge Carrier Spin Polarization in EuO.* Physical Review Letters, **88** (2002), no. 4, p. 047201

[54] D. DiMarzio, M. Croft, N. Sakai and M. Shafer: *EuO effect of pressure on the electrical resistance of EuO.* Physical Review B, **35** (1987), no. 16, pp. 8891–8893

[55] J. Kunes, W. Ku and W. Pickett: *Exchange coupling in Eu monochalcogenides from first principles.* Journal of the Physics Society Japan, **74** (2005), pp. 1408–1411

[56] N. Ingle and I. Elfimov: *Influence of epitaxial strain on the ferromagnetic semiconductor EuO: First-principles calculations.* Physical Review B, **77** (2008), no. 12, p. 121202

[57] D. G. Schlom *et al.*: *Strain Tuning of Ferroelectric Thin Films.* Annual Review of Materials Research, **37** (2007), no. 1, pp. 589–626

[58] R. Schiller and W. Nolting: *Prediction of a Surface State and a Related Surface Insulator-Metal Transition for the (100) Surface of Stochiometric EuO.* Physical Review Letters, **86** (2001), no. 17, pp. 3847–3850

[59] R. Rausch and W. Nolting: *The Curie temperature of thin ferromagnetic films.* Journal of Physics: Condensed Matter, **21** (2009), no. 37, p. 376002

[60] D. Teaney: *Specific Heats of Ferro-and Antiferromagnets in the Critical Region'.* NBS special publication, (1966), pp. 50–57

[61] K. Ahn, a. O. Pecharsky, K. a. Gschneidner and V. K. Pecharsky: *Preparation, heat capacity, magnetic properties, and the magnetocaloric effect of EuO.* Journal of Applied Physics, **97** (2005), no. 6, p. 063901

[62] J. Beukers: *Spectroscopy and transport on europium based ferromagnetic insulators.* Ph.D. thesis, University of Twente (2012)

[63] S. Rubin, T. O. Passell and L. E. Bailey: *Chemical Analysis of Surfaces by Nuclear Methods.* Analytical Chemistry, **29** (1957), no. 5, pp. 736–743

[64] M. Mayer: *SIMNRA User's Guide, Report IPP 9/113,.* Technical report, Max-Planck-Institut für Plasmaphysik,, Garching, Germany (1997)

[65] D. Paraskevopoulos, R. Meservey and P. Tedrow: *Spin polarization of electrons tunneling from 3d ferromagnetic metals and alloys.* Physical Review B, **16** (1977), no. 11, p. 4907

[66] P. M. Tedrow and R. Meservey: *Spin-Dependent Tunneling into Ferromagnetic Nickel.* Physical Review Letters, **26** (1971), no. 4, pp. 192–195

[67] R. Meservey and P. M. Tedrow: *Spin-orbit scattering in superconducting thin films.* Physics Letters A, **58** (1976), no. 2, pp. 131 – 132

[68] M. Y. Efremov *et al.*: *Discrete Periodic Melting Point Observations for Nanostructure Ensembles.* Physical Review Letters, **85** (2000), no. 17, pp. 3560–3563

[69] K. L. Kearns *et al.*: *Observation of low heat capacities for vapor-deposited glasses of indomethacin as determined by AC nanocalorimetry.* The Journal of chemical physics, **133** (2010), no. 1, p. 014702

[70] E. N. Abarra, K. Takano, F. Hellman and A. E. Berkowitz: *Thermodynamic Measurements of Magnetic Ordering in Antiferromagnetic Superlattices.* Physical Review Letters, **77** (1996), no. 16, pp. 3451–3454

[71] E. Leon-Gutierrez *et al.*: *In situ nanocalorimetry of thin glassy organic films.* The Journal of Chemical Physics, **129** (2008), p. 181101

[72] A. F. Lopeandía, F. Pi and J. Rodríguez-Viejo: *Nanocalorimetric analysis of the ferromagnetic transition in ultrathin films of nickel.* Applied Physics Letters, **92** (2008), no. 12, p. 122503

[73] M. Molina-Ruiz *et al.*: *Evidence of finite-size effect on the Néel temperature in ultrathin layers of CoO nanograins.* Physical Review B, **83** (2011), no. 14, p. 140407

[74] S. A. Adamovsky, A. A. Minakov and C. Schick: *Scanning microcalorimetry at high cooling rate.* Thermochimica Acta, **403** (2003), no. 1, pp. 55–63

[75] R. Karmouch *et al.*: *Damage evolution in low-energy ion implanted silicon.* Physical Review B, **75** (2007), no. 7, p. 075304

[76] E. Olson, M. Efremov and L. Allen: *The design and operation of a mems differential scanning nanocalorimeter for high-speed heat capacity measurements of ultrathin films.* Journal of Microelectromechanical Systems, **12** (2003), no. 3, pp. 355–364

[77] A. F. Lopeandía *et al.*: *Heat transfer in symmetric U-shaped microreactors for thin film calorimetry.* Journal of Micromechanics and Microengineering, **16** (2006), no. 5, pp. 965–971

[78] A. F. Lopeandia and J. R. Viejo: *Development of Membrane-based Calorimeters to Measure Phase Transitions at the Nanoscale.* Ph.D. thesis, Universitat Autónoma de Barcelona (2007)

[79] F. Rau: *No Title.* In *Proc. Rare Earth Res. II*, p. 117 (1964)

[80] A. A. Dakhel: *Poole-Frenkel electrical conduction in europium oxide films deposited on Si(100).* Crystal Research and Technology, **38** (2003), no. 11, pp. 968–973

[81] A. A. Dakhel: *Correlated structural and optical properties of thin Eu oxide films.* Materials chemistry and physics, **80** (2003), pp. 186–190

[82] S. Mochizuki, T. Nakanishi, Y. Suzuki and K. Ishi: *Reversible photoinduced spectral change in Eu2O3 at room temperature.* Applied Physics Letters, **79** (2001), no. 23, p. 3785

[83] W. Chen *et al.*: *Structure, luminescence, and dynamics of Eu2O3 nanoparticles in MCM-41.* The Journal of Physical Chemistry B, **106** (2002), pp. 7034–7041

[84] S. Wang, W. Wang and Y. Qian: *Preparation and characterization of Eu2O3 nanometer thin films by pulse ultrasonic spray pyrolysis method.* Materials Research Bulletin, **35** (2000), no. 12, pp. 2057–2062

[85] S. V. Mahajan and J. H. Dickerson: *Understanding the growth of Eu2O3 nanocrystal films made via electrophoretic deposition.* Nanotechnology, **21** (2010), no. 14, p. 145704

[86] Y. C. Shin *et al.*: *Optical Properties of Europium-Silicate Thin Films Fabricated on Different SiOx Intermediate Layer.* Journal of the Korean Physical Society, **50** (2007), no. 6, p. 1764

[87] G. Bellocchi *et al.*: *Synthesis and characterization of light emitting Eu2O3 films on Si substrates.* Journal of Luminescence, (2011), pp. 39–41

[88] G. Bellocchi *et al.*: *Eu3+ reduction and efficient light emission in Eu2O3 films deposited on Si substrates.* Optics express, **20** (2012), no. 5, pp. 5501–5507

[89] Y. Castro *et al.*: *Synthesis, characterization and optical properties of Eu2O3 mesoporous thin films.* Nanotechnology, **18** (2007), no. 5, p. 055705

[90] J. Qi, T. Matsumoto, M. Tanaka and Y. Masumoto: *Electroluminescence of europium silicate thin film on silicon.* Applied Physics Letters, **74** (1999), no. 21, p. 3203

[91] L.-C. Yen *et al.*: *Electrical and reliability characteristics of polycrystalline silicon thin-film transistors with high-κ Eu2O3 gate dielectrics.* Applied Physics Letters, **100** (2012), no. 17, p. 173509

[92] Y. Lin *et al.*: *Epitaxial growth of Eu2O3 thin films on LaAlO3 substrates by polymer-assisted deposition.* Applied Physics Letters, **85** (2004), no. 16, p. 3426

[93] S. V. Mahajan, D. W. Kavich, M. L. Redigolo and J. H. Dickerson: *Structural properties of electrophoretically deposited europium oxide nanocrystalline thin films.* Journal of Materials Science, **41** (2006), no. 24, pp. 8160–8165

[94] M. Paranthaman *et al.*: *Fabrication of Long Lengths of Epitaxial Buffer Layers on Biaxially Textured Nickel Substrates Using a Continuous Reel-to-Reel Dip-Coating Unit.* Journal of the American Ceramic Society, **84** (2001), no. 2, pp. 273–278

[95] M. P. Singh *et al.*: *Structural and electrical properties of low pressure metalorganic chemical vapor deposition grown Eu2O3 films on Si(100).* Applied Physics Letters, **89** (2006), no. 20, p. 201901

[96] *Standard X-ray Diffraction Powder Patterns.* National Bureau of Standards (US.) Monograph, **25** (1984), no. 20, p. 50

[97] K.-W. Chae *et al.*: *The enhancement of luminescence in Co-doped cubic Eu2O3 using Li+ and Al3+ ions.* Journal of Luminescence, **131** (2011), no. 12, pp. 2597–2605

[98] L. Lutterotti: *Maud v.1.993 - Materials Analysis Using Diffraction* (2010)

[99] W. Masterton, E. Slowinski and C. Stanitski: *Chemical Principles*, (CBS College Publishing, Philadelphia1986)

[100] G. V. Samsonov: *The Oxide Handbook.* 2 edition, (IFI/Plenum, New York, NY1982)

[101] R. Sutarto *et al.*: *Epitaxial and layer-by-layer growth of EuO thin films on yttria-stabilized cubic zirconia (001) using MBE distillation.* Physical Review B, **79** (2009), no. 20, p. 205318

[102] B. T. Matthias, R. M. Bozorth and J. H. Van Vleck: *Ferromagnetic Interaction in EuO.* Physical Review Letters, **7** (1961), no. 5, pp. 160–161

[103] F. Cebollada *et al.*: *Anisotropy, hysteresis, and morphology of self-patterned epitaxial Fe/MgO/GaAs films.* Physical Review B, **66** (2002), no. 17, pp. 1–8

[104] A. L. Patterson: *The Scherrer formula for X-ray particle size determination.* Physical Review, **56** (1939), no. 10, p. 978

[105] M. Arnold and J. Kroha: *Simultaneous Ferromagnetic Metal-Semiconductor Transition in Electron-Doped EuO.* Physical Review Letters, **100** (2008), no. 4, p. 046404

[106] R. Shannon: *Revised effective ionic radii and systematic studies of interatomic distances in halides and chalcogenides.* Acta Crystallographica, **A32** (1976), p. 751

[107] J. Camarero, J. Miguel and R. Miranda: *Thickness-dependent coercivity of ultrathin Co films grown on Cu (111).* Journal of Physics:Condensed Matter, **12** (2000), pp. 7713–7719

[108] R. Schiller: *Thickness dependent Curie temperatures of ferromagnetic Heisenberg films.* Solid State Communications, **110** (1999), no. 2, pp. 121–125

[109] M. Efremov *et al.*: *Thin-film differential scanning nanocalorimetry: heat capacity analysis.* Thermochimica Acta, **412** (2004), no. 1-2, pp. 13–23

[110] Y. Shapira and T. B. Reed: *Ultrasonic Propagation in EuO.* Journal of Applied Physics, **40** (1969), no. 3, p. 1197

[111] W. Ma, X. Zhang and K. Takahashi: *Electrical properties and reduced Debye temperature of polycrystalline thin gold films.* Journal of Physics D: Applied Physics, **43** (2010), no. 46, p. 465301

[112] W. Zhang *et al.*: *Analysis of the size effect in electroplated fine copper wires and a realistic assessment to model copper resistivity.* Journal of Applied Physics, **101** (2007), no. 6, p. 063703

[113] A. Bid, A. Bora and A. Raychaudhuri: *Temperature dependence of the resistance of metallic nanowires of diameter ¿15nm: Applicability of Bloch-Grüneisen theorem.* Physical Review B, **74** (2006), no. 3, p. 035426

[114] G. D. Marzi, D. Iacopino, A. J. Quinn and G. Redmond: *Probing intrinsic transport properties of single metal nanowires: Direct-write contact formation using a focused ion beam.* Journal of Applied Physics, **96** (2004), no. 6, p. 3458

[115] S. Kim, H. Suhl and I. Schuller: *Surface Phonon Scattering in the Electrical Resistivity on Co/Ni Superlattices.* Physical Review Letters, **78** (1997), no. 2, pp. 322–325

[116] P. Derlet *et al.*: *Low-Frequency Vibrational Properties of Nanocrystalline Materials.* Physical Review Letters, **87** (2001), no. 20, p. 205501

[117] G. Kastle *et al.*: *Resistivity and phonon softening in ion-irradiated epitaxial gold films.* Journal of Applied Physics, **96** (2004), no. 12, p. 7272

[118] X. Lang, W. Zheng and Q. Jiang: *Size and interface effects on ferromagnetic and antiferromagnetic transition temperatures.* Physical Review B, **73** (2006), no. 22, p. 224444

[119] K. G. Subhadra, B. Raghavendra Rao and D. B. Sirdeshmukh: *X-ray determination of the Debye-Waller factors and Debye temperatures of europium monochalcogenides.* Pramana-Journal of Physics, **38** (1992), no. 6, pp. 681–683

[120] G. Herzer: *Grain size dependence of coercivity and permeability in nanocrystalline ferromagnets.* IEEE Transactions on Magnetics, **26** (1990), no. 5, pp. 1397–1402

[121] R. Meservey and P. Tedrow: *Spin-polarized electron tunneling.* Physics Reports, **4238** (1994), pp. 173 – 243

[122] J. Moodera, M. Taylor and R. Meservey: *Exchange-induced spin polarization of conduction electrons in paramagnetic metals.* Physical review. B, **40** (1989), no. 17, p. 11980

[123] R. Meservey, P. M. Tedrow and J. S. Brooks: *Tunneling characteristics of amorphous Si barriers.* Journal of Applied Physics, **53** (1982), no. 3, p. 1563

[124] D. C. Worledge and T. H. Geballe: *Maki analysis of spin-polarized tunneling in an oxide ferromagnet.* Physical Review B, **62** (2000), no. 1, pp. 447–451

[125] S. Bermon, D. Paraskevopoulos and P. Tedrow: *Ultra-high magnetic field study of the Kondo-type zero-bias conductance peak in magnetically doped metal-insulator-metal tunnel junctions.* Physical Review B, **17** (1978), no. 5, p. 2110

[126] J. Kondo: *Resistance Minimum in Dilute Magnetic Alloys.* Progress of Theoretical Physics, **32** (1964), no. 1, pp. 37–49

[127] J. A. Appelbaum: *Exchange model of zero-bias tunneling anomalies.* Physical Review, **154** (1967), no. 3, pp. 633–643

[128] J. Ekin *et al.*: *Correlation between d-wave pairing behavior and magnetic-field-dependent zero-bias conductance peak.* Physical Review B, **56** (1997), no. 21, pp. 13746–13749

[129] M. de Jong and W. Beenakker: *Andreev reflection in Ferromagnet-superconducter junctions.* Physical Review Letters, **74** (1994), no. 9

[130] K. Boden, W. Pratt Jr and N. Birge: *Proximity-induced density-of-states oscillations in a superconductor/strong-ferromagnet system.* Physical Review B, **84** (2011), no. 2, p. 020510

[131] T. Yokoyama, Y. Tanaka and A. Golubov: *Resonant proximity effect in normal metal/diffusive ferromagnet/superconductor junctions.* Physical Review B, **73** (2006), no. 9, p. 094501

[132] B. Josephson: *Possible new effects in superconductive tunnelling.* Physics Letters, **1** (1962), no. 7, pp. 251–253

[133] V. Ryazanov *et al.*: *Coupling of Two Superconductors through a Ferromagnet: Evidence for a π Junction.* Physical Review Letters, **86** (2001), no. 11, pp. 2427–2430

[134] T. Khaire, W. Pratt and N. Birge: *Critical current behavior in Josephson junctions with the weak ferromagnet PdNi.* Physical Review B, **79** (2009), no. 9, p. 094523

[135] K. Senapati, M. G. Blamire and Z. H. Barber: *Spin-filter Josephson junctions.* Nature Materials, **10** (2011), no. 9, pp. 1–4

[136] P. J. Flanders and M. P. Sharrock: *An analysis of time-dependent magnetization and coercivity and of their relationship to print-through in recording tapes.* Journal of Applied Physics, **62** (1987), no. 7, p. 2918

Acknowledgements

It's surprising how many people are involved in the realization of this thesis. I want to take this opportunity to thank all of them. I really hope I didn't forget anyone.
En primer lugar quiero darle las gracias a Javier Rodríguez-Viejo, por darme la oportunidad de hacer el doctorado en el grupo de nanomateriales y microsistemas (GNaM). Gracias por la paciencia y el constante interes. Has creado un ambiente agradable en el grupo, preocupandote por todos. Llevar un grupo de investigacion y a la vez ser co-director de otro centro de investigacion, MatGas, requiere mucha motivacion y entrega. Sin embargo siempre tienes tiempo para hablar e intercambiar ideas.
Gracias por el soporte financiero de esta tesis por parte del AGAUR con la beca FI predoctoral.

Gracias Maria Teresa por tu entusiasmo, motivacion y las reuniones de grupo tan agradables.
Muchas gracias Gemma, por tu apoyo constante y por todas las discusiones, ya que sean de datos o no. Gracias por ser la co-guia en los últimos cuatro años, esta muy apreciada. Sin tu talento organizativo el grupo probablemente se perderia en el caos.
Manel, durante nuestra investigación doctoral, hemos trabajado mucho juntos. Trabajar contigo en el laboratorio no fue sólo productivo, sino también muy agradable. Muchas gracias y buena suerte en Grenoble. Gracias Marta por tu ayuda tanto profesional como personal. Tambien gracias Aitor por las largas discusiones y el apoyo con la nanocalorimetria. Victor, tienes muchos proyectos abordados, con la licenciatura hiciste un buen trabajo. Gracias!
Gracias tambien a Cristian y Pablo por el suporte en los ultimos anos. A mis antiguos colegas Joan, Alfonso, Jaime y Edgar quiero dar las gracias por compartir sus conocimientos y experiencias conmigo.

Al hacer la investigación experimental son, por supuesto, muy importante las instalaciones de laboratorio.
Por el mantenimiento del Sputtering en MatGas quiero dar las gracias a Raquel, que siempre estaba dispuesta a ayudar. Al technico Emili por arreglar los equipos lo más rapido possible y a Oriol por la introduccion en el

uso del AFM y su ayuda con el mantenimiento del cryostato.
Para las mediciones de XRD y las deposiciones PLD en el CIN2, le debo mucho a Jose Santiso. Su experiencia en las medidas de diffracción es indispensable. Gracias a los miembros de su grupo Jaume y Pablo con cuales no solo comparto el interes en medidas de diffracción sino tambien la aficin en deportes.
Gracias Maria Angeles y Raquel de la sala blanca de la UAB por los consejos y el apoyo en los experimentos.

Thanks to all the people at the FBML at MIT I had the privilege to work with, specially for the guidance of Dr. Jagadeesh Moodera. The daily discussions at the coffee break were very interesting and I learnt a lot in those few months. Thanks to Guo-Xing and Ferhat for the help with the MBE system. Furthermore I would like to thank Ssu-Yen, Karthik, Matthias, Pascal, David and Jean-Baptiste for their collaboration.
Thanks a lot to Joost, who I also met at the FBML and further collaborations worked out to be fruitful. The visit to the University Twente in the group of Alexander Brinkman was very impressive. Thanks for the warm welcome to your family, the delicious vegetarian "hutspot" and the beautiful trip to Giethoorn.

Gracias a todos mis amigos de Barcelona, Austria y el resto del mundo.

Ein großes Dankeschön an meine Familie in Österreich. Vor allem vielen Dank für die unaufhörliche Unterstützung und die regelmäßigen Besuche meiner Eltern Roswitha und Karl. Ihr habt mich stehts motiviert und trotz der großen Distanz wart ihr immer für mich da. Vielen Dank Martin, für einen inspirierenden Kalender, die Erklärung all der biologischen Prozesse und vieles mehr. Du bist und bleibst mein liebster kleiner Bruder. Ich freue mich schon sehr bald wieder näher bei euch zu sein.
Al final vull donar les gràcies a Carlos per la teva increïble paciència, per la motivació i el suport en temps difícils, per acompanyar-me a qualsevol bogeria i pel teu amor.

Summary

Ferromagnetic europium monoxide (EuO) displays a huge variety of physical phenomena and due to its simple structure it is often used as a model system. It shows magneto-optic Kerr effect, spin-dependent transport and, in the case of Eu doped EuO, a metal-insulator transition showing a colossal magnetoresistance. EuO is also the only known binary oxide that can be grown in a thermodynamically stable form in contact with silicon. The application of EuO for spin injection either by matching its conductivity or by using it as insulating tunnel barrier has been shown. Its relatively low Curie temperature of 69 K can be enhanced by doping, normally with lanthanides or metal europium.

However, problems of fabricating thin EuO films make its implementation difficult. Europium monoxide readily forms higher, non-magnetic oxides Eu_2O_3 and Eu_3O_4, when exposed to air. Also recent studies still report on considerable amounts of Eu^{3+} present in the samples. This thesis focuses on the growth, magnetic properties and heat capacity of EuO. Therefore several techniques, such as sputtering, molecular beam epitaxy (MBE) and pulsed laser deposition (PLD), are used to obtain high quality EuO thin films on yttria-stabilized cubic zirconia (YSZ) (001) and silicon substrates.

In a first step the growth of epitaxial EuO on YSZ was tempted using pulsed laser deposition. Due to the high oxygen content in the chamber epitaxial Eu_2O_3 was grown. This is the most used form of the europium oxides nowadays, as it can be implemented in photoactive coating, optical storage data, and fluorescent displays due to its luminescence properties. Due to its high dielectric strength recently it was also used in microelectronic devices as high dielectric gates. However, studies on high quality epitaxial Eu_2O_3 are still rare.
In order to make EuO accessible for industrial purposes sputter deposition is the preferred option. Attempts of EuO deposition by sputtering from a metal target are described. The effect of different substrates, inter- and capping layers is discussed. We show that the high reactivity of Eu inside the plasma leads to bad reproducibility of depositions. X-ray measurements were used to determine the approximate content of the Eu-EuO-Eu_2O_3 films.

At the moment MBE deposition is the preferred technique for EuO deposition, as it offers great control of all critical deposition parameters. Due to its perfect lattice match YSZ is favoring the growth of epitaxial EuO. By introducing an MgO buffer layer problems in the deposition could be overcome and crystallinity is enhanced. When considering applications of EuO doping is an important topic, since it allows the enhancement of the Curie temperature and the tuning of the resistivity over various orders of magnitude. Doping EuO with a very low percentage of Se surprisingly shows a large enhancement of the Curie temperature. As no model exists for this case, the mechanism for the enhancement of the Curie temperature by Se is discussed.
The first nanocalorimetric measurements on EuO thin films are presented. Apart from improving the measurement system, a mathematical formalism was developed to allow a more accurate calculation of the heat capacity. Thin films EuO could be measured in thicknesses down to a few nanometers, where size effects come to play. A decrease of the Curie and Debye temperature as well as the magnetic entropy is observed due to the decrease in the number of nearest magnetic interaction neighbors at the surface.
Ferromagnetic insulating EuS barriers - similar to EuO barriers - are used for or transport measurements, because they are less reactive and therefore can be deposited in good quality in evaporation chambers with a higher base pressure. The effect of the interface between EuS and superconducting aluminium is investigated by introducing thin Cu and Si interlayers in SC-FI-SC junctions. A zero bias peak is observed, which is hysteretic with respect to an applied magnetic field. The origin of this feature is discussed. The maximum spin polarization that was obtained is about 56 %.